Solution-Processed Quantum Dot Infrared Lasers

Nima Taghipour

ICFO - The Institute of Photonic Sciences
Barcelona, 2023

Solution-Processed Quantum Dot Infrared Lasers

Nima Taghipour

under the supervision of

Professor Gerasimos Konstantatos

submitted this thesis in partial fulfillment
of the requirements for the degree of

Doctor Of Philosophy in Photonics

by the

Universitat Politècnica de Catalunya
Barcelona, 2023

To my family and my wife,
who made this work possible...

Abstract

Colloidal semiconductors quantum dots (CQDs) have emerged as a promising solution-processed gain material that can be engineered via low-cost and scalable chemical techniques. Owing to quantum confinement, their emission wavelengths and optical properties can be tuned from the visible to the infrared. Despite these possible advantages, the realization of lasing action in CQDs is complicated and fundamentally stems from the non-unity degeneracy of the band-edge state. This results in multiexcitonic nature of optical gain, leading to high lasing thresholds. This, in turn, leads to a very short optical gain lifetime which is caused by Auger recombination.

Following the first demonstration of lasing action in CQDs, this field has thus far experienced remarkable developments with materials offering emission in the visible showing limited application potential. However, the possibility of lasing in the infrared region would open a new realm of applications for this material platform in optical telecommunications, photonic integrated circuits, and LIDAR applications. To unleash those applications, the demonstration of solution-processed infrared lasers in the eye-safe window between 1.5-1.6 μm operating robustly at room temperature is a prerequisite.

Midgap trap states in CQDs limit the performance of optoelectronics devices. In particular, PbS CQDs suffer from a very fast trap-assisted Auger process leading to high lasing thresholds. To suppress this type of Auger process, in this work, we use a binary nanocomposite of PbS CQDs and ZnO nanocrsystals (NCs) where the former serves as the infrared gain medium and the latter as a remote passivant for midgap traps in PbS CQDs. This binary heterostructure drastically suppresses the Auger process and lowers the lasing thresholds.

Low threshold infrared CQD-laser has been thought to be not possible because of 8-fold degeneracy of the band-edge state in the infrared-emitting Pb-chalcogenide CQDs. In this Thesis, we demonstrate that using core-alloyed shell heterostructured CQD comprising PbS as core and PbSSe as shell allows suppressing Auger process.

Furthermore, by applying doping to specially engineered CQDs, we demonstrate a substantial reduction in lasing threshold down to sub-single exciton level per-dot thanks to the blocking of the ground state absorption. Employing these CQDs has drastically improved the net modal coefficient of the medium and brought it on par with a gain coefficient of epitaxially grown III-V infrared semiconductors.

The realization of CQD infrared laser-diodes will have a profound impact in many disciplines. Here, by engineering the electric field distribution in our devices, we show stimulated emission in a record ultra-thin gain media which is beyond the slab waveguide theoretical limit by introducing scatterers implemented by ZnO NCs. We employ this thin gain media as the active layer in a full-stack light emitting diode (LED) device. Also, to overcome the existing challenge underpinned by the optical losses of the metal contacts that have prevented the realization of stimulated emission in a LED, we use an engineered transparent conductive oxide and graphene as anode and cathode of the LED, respectively. Finally, our proposed LED structure leads us to realize a dual function device showing strong infrared spontaneous- and stimulated-emission under electrical- and optical-pumping, respectively.

In summary, we have demonstrated that CQDs can emerge as a robust technology for the realization of infrared lasers. Our proposed CQD systems lead us to achieve high performance laser devices under optical excitation and using CQD heterostructures as an active medium in the proposed LED structure paves the way towards the future development of infrared CQD-laser diodes.

Resumen

Los puntos cuánticos de semiconductor sintetizados mediante procesos coloidales (CQDs) han resultado ser un prometedor medio de ganancia cuya obtención puede llevarse a cabo mediante técnicas de bajo coste y alta reproducibilidad química. Gracias al efecto del confinamiento cuántico, su longitud de onda puede modularse con precisión desde el visible hasta el infrarrojo. A pesar de todas estas ventajas, conseguir acción láser utilizando estos materiales presenta una gran dificultad, originada fundamentalmente por el alto grado de degeneración de los niveles energéticos más bajos, dando lugar a umbrales ópticos más altos. Esto hace que se requiera de múltiples excitones para conseguir la acción láser, lo que a su vez resulta en tiempos de ganancia muy reducidos por culpa de la recombinación Auger.

Tras la primera demostración del láser utilizando CQDs, este campo ha experimentado un importante desarrollo utilizando materiales con emisión en el visible, limitando sus potenciales aplicaciones. La obtención de luz láser en la región infrarroja supondría por tanto un nuevo abanico de posibilidades para tecnologías tales como las telecomunicaciones ópticas, la fotónica integrada, la imagen biomédica o las aplicaciones LIDAR. Para la realización de todas ellas, es requisito fundamental el desarrollo de láseres infrarrojos en el rango 1.5-1.6 μm y que puedan operar a temperatura ambiente de forma estable.

Las trampas electrónicas dentro de la banda prohibida son factores limitantes en el funcionamiento de los dispositivos optoelectrónicos. En el caso de los CQDs basados en PbS, los procesos Auger debidos a estas trampas dan lugar a altos umbrales de ganancia láser. Para mitigar dichos procesos, empleamos un nanocomposite a base de CQDs de PbS y nanocristales de ZnO, donde los CQDs actúan como medio de ganancia y los nanocristales de ZnO sirven de pasivantes de dichas trampas. Esta heteroestructura binaria suprime drásticamente los procesos Auger y reduce el umbral láser.

La fuerte degeneración (8) de los estados energéticos fundamentales de la banda

prohibida en los calcogenuros de plomo ha obstaculizado el desarrollo del láser infrarrojo basando en CQDs. En esta tesis, demostramos la supresión de los procesos Auger mediante el uso de CQDs con estructura núcleo (PbS)/corteza (PbSSe). También probamos que, mediante dopaje, es posible reducir el umbral láser a valores por debajo de 1 excitón/CQD gracias a la reducción en la absorción del estado fundamental. El uso de estos CQDs mejora sustancialmente el coeficiente modal neto del medio de ganancia, equiparándose al de los semiconductores infrarrojos del grupo III/V crecidos epitaxia.

El uso de diodos láser infrarrojos fabricados mediante procesos en solución supondrá un cambio significativo en múltiples disciplinas. Mostramos que es posible la obtención de emisión estimulada de luz en un medio de ganancia ultrafino con un espesor por debajo del límite teórico para guías de onda planas gracias a la modificación del campo eléctrico mediante la inclusión de nanocristales de ZnO actuando como puntos dispersivos. Empleamos este medio activo para construir un dispositivo LED. Además, para evitar el problema de las pérdidas ópticas debidas a los contactos metálicos que hasta ahora habían dificultado la obtención de emisión estimulada, hemos empleado un óxido conductor transparente y grafeno como ánodo y cátodo de nuestro LED, respectivamente. Nuestra propuesta de LED demuestra que es posible la fabricación de un dispositivo de funcionamiento dual capaz de producir luminiscencia espontánea y estimulada mediante bombeo eléctrico y óptico, respectivamente.

En resumen, hemos probado que el uso de CQDs ofrece una alternativa tecnológica para la producción de luz láser. Estos dispositivos basados en CQDs permiten fabricar fuentes láser de alto rendimiento mediante bombeo óptico. Además, su uso como medio activo en un dispositivo LED supone un avance hacia futuros láseres de diodo basados en CQDs.

Acknowledgements

First and foremost, I would like to express my sincere and profound gratitude to my supervisor Gerasimos Konstantatos. I feel very fortunate for having had him as my supervisor. He gave me plenty of opportunities for doing right and wrong things, and he always come up with sincere advice on any topic. His excellent mentorship, support and guidance led to realize this Thesis.

I am grateful to all my colleagues and friends in our FoN group. During my Ph.D., I have been lucky to collaborate with very supportive, patient and bright people. I would like to especially thank Mariona for providing PbS quantum dots. Without her endless patience and support, this Thesis would not have been possible. Guy deserves huge gratitude as almost my second mentor, he was always being around when I needed help. He always tried to answer my reasonable or unreasonable questions. I feel very fortunate to share my office with Onur, Guy, Katerina, Biswajit and Miguel. Guys, you are amazing, you were making the office an enjoyable place to work and Lunchhh!!. To Shanti and Katerina for their sincere friendship, for our endless funny conversations especially about Bears, and of course their skills in beach-volley, thank you. To my teammates of "Mint & Parsley", I will miss you certainly. Thank you Hamed for our conversions about everything. I would also like to thank Santanu and Sotirios for our irregular and fruitful discussions about the semiconductor physics. I am also thankful Yongjie, Gaurav, Avijit, Zhouran and Stephy for their help in the lab and our scientific and non-scientific conversations. I would like to thank all the past and present members of FoN: Shuchi, Yu, Alberto, Ignasi, Iñigo, Yurong, Adi, Rajesh, Debranjan, Jae Taek, Lucheng, Hyun-Soo, Marinos. Special thank goes to Miguel and Mariona for helping me with Latex and the *Resumen*. I would like to thank Bahare for her support in designing the cover of this Thesis.

I would like to thank our collaborators: Prof. Koray Aydin and Ibrahim Tanriover from Northwestern University and Prof. Andreas Othonos from University of Cyprus. My special thank goes to Prof. Aydin for his support during my applications.

I am very grateful to all the ICFOnians and people who make ICFO an amazing place. ICFO truly provide a perfect environment from all aspects to learn the most from the institute. I owe a huge thank to all the HR especially Anne and Ingrid for their sincere support. I am also thankful to ICONS, management, KTT, frontdesk, IT, workshops, utility and purchasing departments. I would like to thank the BIST and the PREBIST fund program under Marie Skłodowska-Curie action for financial support during my Ph.D.

Dostum *Zafer*, vay be sonuna geldik hocam!. Geçirdiğimiz tüm zamanlar için çok teşekkür ederim hocam. Mesela güzel bir kahve keyfi manzaraya karşi özlemedim değil, ya mesela düşünüp düşünüp restoran aramak. Hatta uzun uzun hiç bir maksadi olmayan yürümeği bile...Neyse en iyisi... Başka bir zaman'da görüşmek dileyiğle efendim.

Last but not least, from the bottom of my heart, I would like to express my deepest gratitude to my dad Hamidollah, my mom Mehrangiz and my brother Pouya for their endless love, sincere support and encouragement throughout my life. I must also express my profound gratitude to my love Samira for her endless love and support during these years. She colored my life as a sky blue...

Nima Taghipour, December 2022, Barcelona

Contents

Acronyms and Symbols

1D/2D/3D One/two/three-dimensional

1PA/2PA One/two photon absorption

AFM Atomic force microscopy

ASE Amplified spontaneous emission

C/A-S Core/alloyed-shell

CQD Colloidal semiconductor quantum dot

CB Conduction band

CMOS Complementary metal-oxide semiconductor

DFB Distributed feedback

DOS Density of states

EL electroluminescent

Ethanol Et-OH

IR/NIR/MIR/SWIR Infrared/Near infrared/Mid infrared/short-wave infrared

ITO Indium tin oxide

LASER Light amplification by stimulated emission of radiation

LED Light emitting diode

LIDAR light detection and ranging

Methanol Me-OH

NC Nanocrystal

PL-QY Photoluminescence quantum yield

PIC Photonic integrated circuit

SEM Scanning electron microscopy

TA Transient absorption spectroscopy

TAS Thermal admittance spectroscopy

TE/TM Transverse electric/magnetic

TRPL Time-resolved photoluminescence

TCSPC time-correlated single-photon counting

VB Valence band

VCSEL vertical-cavity surface-emitting

XPS X-ray photoelectron spectroscopy

XRD X-ray powder diffraction

1

Introduction

"Learn from yesterday, live for today, hope for tomorrow. The important thing is not to stop questioning."

-Albert Einstein

Photonics is the science of controlling, manipulating, detecting, generating, and amplifying the light. Photonics technology plays a crucial role in the development of innovation across a broad range of applications including lighting [1, 2], energy production [3], display [4], healthcare [5], global security and safety [6], telecommunication [7], and manufacturing industry [8]. It offers unique and novel solutions to the challenges of current technologies based on electronics where their performance is limited in terms of speed, accuracy, and capability. Specifically, photonics technology is used for generating low-cost, high-quality, and environmentally safe light sources. Among all , coherent light sources are those sources which emit the light at the same frequency and the same phase. Especially, the fundamental principle to achieve coherent amplified light is **L**ight **A**mplification by **S**timulated **E**mission of **R**adiation which is known by the acronym **LASER**. Laser device is an optical oscillator, in which the optical amplification in the gain medium is incurred in a round trip through a positive feedback loop. This process proceeds indefinitely until the amplification in the gain medium is larger than the losses of the feedback system, in which the output frequency is determined by the resonance frequency of the oscillator.

Lasers have become a versatile tool for our daily lives, they are used in printers, barcode readers, medical surgery, medical treatments, free-space optical telecommunication, semiconductor device fabrication, and military applications. Based on the employed gain medium in the laser devices, its output wavelength is tuned across the electromagnetic spectrum ranging from ultraviolet to the mid-infrared. Specifically, infrared lasers can be used in optical telecommunication [8], photonics integrated circuits (PICs) [9], 3D imaging [10], medical diagnostics [11] and light detection and ranging (LIDAR) applications [12]. The current technology for the infrared lasers is based on costly III-V epitaxially grown semiconductors [13] or Erbium-doped optical fiber technology [14]. The mentioned techniques are neither compatible with silicon CMOS technology nor cover the full optical telecommunication transparency window. Colloidal semiconductor quantum dots (CQDs) which are produced through low-temperature colloidal synthesis, representing a promising alternative to high-temperature vapor-phase epitaxy grown semiconductors. In addition to the low-cost production method, CQDs can be transferred onto any arbitrary substrate thanks to their solution processability. They also show size-tunable optical properties and CMOS compatibility.

In principle, CQDs are an attractive material platform for the realization of solution-processed lasers in a broad range of spectrum extending from the visible to the infrared. However, up to now, their performance has been hindered because of some fundamental issues making CQDs-lasers impractical for daily life applications. The limitation in CQDs-lasers arises from the non-unity degeneracy of the involved band-edge state in the light amplification process, which is associated with an additional complication known as Auger recombination. In which, the released energy from the recombination of the electron-hole (e–h) pair is transferred to a third carrier. This non-radiative process results in fast annihilation of the gain-active optical states. Another important challenge is the low optical gain coefficient in un-engineered CQDs stemming from a small stimulated emission cross-section of the CQDs. Therefore, developing such a CQD system, which simultaneously reduces the degeneracy of the band-edge state, suppresses Auger recombination and achieves large stimulated emission cross-section is highly favorable to the development of the practical CQDs-lasers.

In this Thesis, we have developed and demonstrated breaking record infrared optical gain and lasing performance employing a hybrid of PbS CQDs/ZnO nanocrystals as a gain medium that accomplishes record long Auger recombination, low threshold, and highly stable infrared optical gain/laser devices. Our approach to suppress the Auger process in PbS CQDs has unleashed the capability of engineering optical properties of CQDs at the supra-nanocrystalline level. In addition, using PbS/PbSSe CQDs led us to achieve a record low-threshold infrared optical gain/laser devices along with a

record high infrared optical gain coefficient among all solution-processed semiconductors. We have also reported the first dual function structure in a full-stack CQDs-LED device, which shows strong spontaneous- and stimulated- emission under electrical- and optical- excitation, respectively. Overall, our findings in this thesis have contributed to understanding the excitonic and device properties of infrared-emitting CQDs for the development of efficient solution-processed infrared laser devices.

1.1 Thesis outline

In chapter 2, we discuss the optical and electronic properties of CQDs. We also discuss their single- and multi-excitonic properties. Moreover, we introduce the optical gain and lasing mechanisms in CQDs. We finally outline the challenges of the realization of lasing action in CQDs especially in the infrared region.

In chapter 3, we introduce a new method to control the Auger process in CQDs. In doing so, we employ a solid film by using binary nanocomposites of the semiconductor nanocrystals, in which the trap-assisted Auger recombination is suppressed in the gain medium. This approach allows us to achieve a remarkable reduction in gain/lasing thresholds compared to bare gain medium devices. Furthermore, we show that our single-mode infrared laser is highly stable under continuous pumping.

In chapter 4, we develop a new heterostructure of infrared-emitting CQDs that show optical gain/lasing performance beyond the state of the art. In this study, our proposed architecture exhibits record low threshold infrared lasing along with record long gain lifetime. Also, we achieved record high modal gain coefficient in our devices.

In chapter 5, we report on a full-stack CQD LED device architecture that besides operating as a LED, when electrically driven, it also serves to emit stimulated emission upon optical pumping that stems from the LED's active layer. That was due to the realization of ultra-thin film gain medium and the use of graphene as one of the LED electrodes. The latter has been instrumental in the realization of stimulated emission from an active LED device due to suppressing optical losses typically found in metal structures.

2

Scientific Background

"One never notices what has been done; one can only see what remains to be done."

-Marie Skłodowska-Curie

The central topics of this thesis are solution-processed infrared lasers based on CQDs and understanding excitonic properties of these material to achieve highly-performed laser. The key concept is engineering optical and electronics properties of the CQDs for overcoming fundamental issues in CQDs-lasers. In this chapter, before presenting our findings, we provide basic information about CQDs including their size-dependent electronic properties and excitonic properties. Then, we discuss about optical gain and lasing mechanisms in CQDs and their fundamental limitations for having efficient CQD-lasers.

2.1 Colloidal semiconductor quantum dots

Colloidal semiconductor quantum dots are nano-sized crystalline semiconductors containing of hundreds to thousands of atoms having a diameter size smaller than Bohr radius (r_b), which is the natural extent of an exciton (bound e–h pair via Coulomb force) [15, 16]. Owing to quantum confinement observed at this length scale, these nanocrystals (NCs) show size-dependent optical and electronic properties which are significantly different than their bulk semiconductor counterparts. In bulk semiconduc-

tors, valence and conduction bands are formed as continuous energy bands which are separated with a given band-gap energy depending on the crystalline structure and the composition of the semiconductor [17]. On other hand, because of quantum confinement effect, semiconductor quantum dots (QDs) exhibit discretized energy levels having a tunable band-gap energy which can be engineered by changing their size, shape and composition [15, 16].

2.1.1 Exciton

In semiconductors, a bounded electron–hole pair is created by absorbing the incident light which known as exciton. Eventually, the photo-generated excitons vanish through either the radiative or non-radiative recomibnations. The former results in generating the photons, whereby the latter releasing phonons which dissipate as heat. Because of the Coulomb interaction between the electron and hole, the required energy for generating the exction is slightly lower than the material band gap. The energy of this attractive Coulomb interaction known as exciton binding energy (E_X) which can be calculated from the following expression [18]:

$$E_X = 1.765 \frac{e^2}{\epsilon_\infty r} \tag{2.1}$$

Here, $\epsilon_\infty = \epsilon$ is high frequency dielectric constant, and r is the radius of the molecule.

2.1.2 Quantum confinement and tuning band gap

Density of states

The density of states (DOS) is the basic concept of the quantum confined structures that determines the electronic and optical properties of the low dimensional system. The density of states (D) of a particular system is defined as the available energy states per unit energy per unit volume [19, 20]. In bulk semiconductors, the electrons are free to move in three dimensions, then DOS of electrons ($g(E)$) can be calculated from:

$$g(E) = \frac{1}{2\pi^2} \left(\frac{2m^*}{\hbar^2} \right)^{3/2} \sqrt{E} \tag{2.2}$$

where m^* is the effective mass of electron and E is the energy. Thus, the electron can be found in a continuum of the energy levels. Reducing the dimensionality from three-

dimension (3D) to 2D system (e.g., quantum well system), the electron is confined in one dimension and can freely move in the other two dimensions, the DOS follows a step-like function. $g(E) = \frac{m^*}{\pi\hbar^2}$, which is independent of the energy. In 1D system such as nano-wires, for which the electron is confined in two dimensions and is free to move in one dimension, the DOS exhibits an array of spikes: $g(E) = \frac{1}{\hbar\pi}\sqrt{\frac{m^*}{2E}}$. Quantum dots which are considered as 0D system, the electrons is confined in 3D, the DOS is defined as δ-functions: $g(E) = 2\delta(E)$

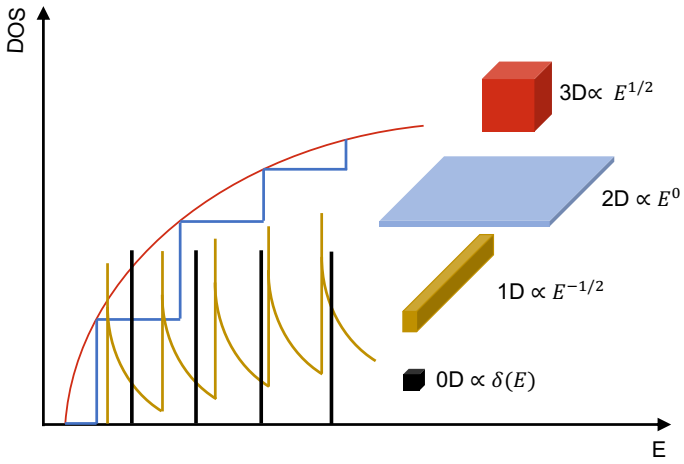

Figure 2.1: Schematic representation of DOS for various dimensionalities

Quantum confinement in quantum dots

The quantized energy levels of electron and hole in a quantum confined structure can be approximated as a "particle in a box". Specifically, in zero-dimensional (0D) QDs – 3D spherical confinement– the quantized energy levels can be calculated from [21]:

$$E_{n,l} = \frac{\hbar^2}{2m_0 r^2} \tag{2.3}$$

where, $\hbar$ is the reduced Planck constant, $\alpha_{n,l}$ is the n^{th} zero of l^{th}-order spherical Bessel function arising from spherical boundary condition, $n(1, 2, 3, \dots)$ and $l(s, p, d, \dots)$ are the quantum numbers, and m_0 is the particle mass. Figure 2.2a schematically represents the simple model of a QD which is embedded in an insulating matrix. As can be seen in Figure 2.2b, quantum confinement in QD results in larger band-gap energy compared to their bulk counterparts, which is the origin of size-dependent optical and electronic

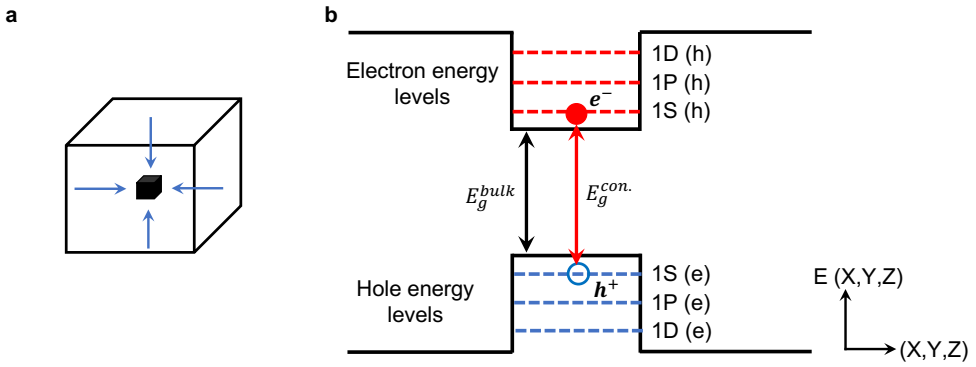

Figure 2.2: (a) Schematic illustration of a quantum dot (particle in a box). (b) Quantum confined energy levels for electron and hole at any dimension (X, Y, and Z) where E_g^{bulk} and E_g^{con} is band-gap energy of bulk semiconductor and effective band-gap energy of quantum dot respectively.

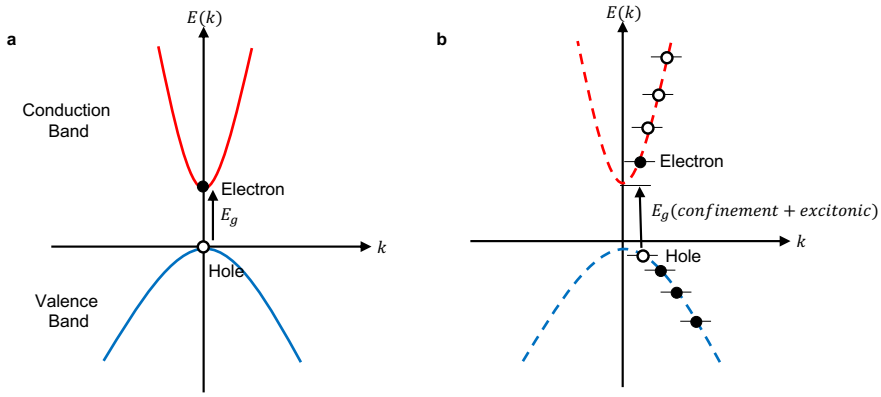

Figure 2.3: Band diagram of direct band gap for bulk semiconductor (a), and semiconductor QD (b).

properties of QDs. Upon photoexcitation of semiconductors with energies higher than their band-gap energy, excitons are generated.

Then, considering excitonic effects in quantum confined semiconductors yields the following expression for size-dependent band-gap energy [18]:

$$E_g = E_g^{bulk} + \frac{\hbar^2 \pi^2}{2 m_{eh} r^2} - 1.765 \frac{e^2}{\epsilon_\infty r} \tag{2.4}$$

This expression accounts for quantum confinement and excitonic binding effects in QDs. The first term refers to bulk semiconductor band-gap energy, the second arises

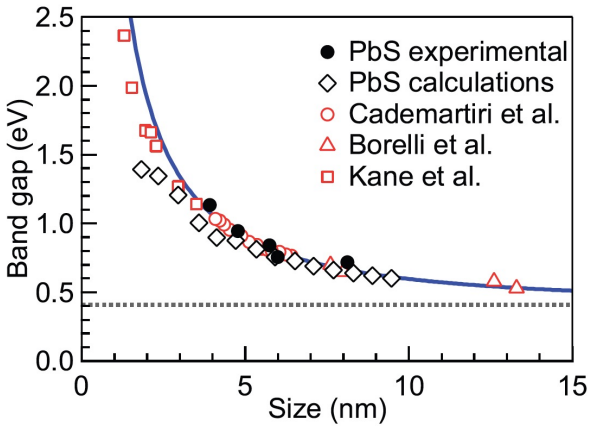

Figure 2.4: PbS CQDs band gap as a function of particle size. Note, the black dots represent the experimental data. The dotted line shows the PbS band gap. Reprinted with permission from [22]. Copyright 2009 American Chemical Society.

from confinement effect and the last attributes to the exciton binding energy. Note, $m_{eh} = (m_e m_h)/(m_e + m_h)$ is the reduced e–h mass, in which m_e and m_h are the electron and hole effective masses, respectively [18]. Figure 2.3 plots the band diagram of a simple two-level system for a direct gap semiconductor in bulk and QD form. In the case of the QD, the electronic bands are discretized due to the quantum confinement, in which the band gap energy changes because of the excitonic effect as shown in Equation 2.4. Energy in small size QDs scales with $1/r^2$ due to quantum confinement effect, while excitonic effect contributes as $1/r$. Therefore, the band gap energy of a QD is basically dictated by the size of the QD not by the Coulomb interaction between e–h pair [18]. As an exemplary case, Figure 2.4 exhibits size-dependent PbS CQDs band gap adapted from [22].

In a more realistic band structure diagram, the band diagram of II-VI and IV-VI is more complicated, where complex interactions are raised. Particularly, in lead chalcogenide (i.e., PbS, PbSe, PbTe) semiconductors, the band gap occurs at the L-edge of the Brillion zone ((111) direction, $k = \pi a$ where k is the wave vector and a represents bulk lattice constant), while the bad gap of II-VI semiconductors occurs at the Γ-point of the Brillouin zone (k=0). This is originated by the anomalous bonding in IV-VI semiconductor materials. In the bulk structure, the conduction band (CB) formed by Pb 6s atomic orbitals which significantly shows lower energy due to strong spin-orbital coupling. This results in leaving p-states especially those involved in p-p transition, leading to produce band gap at L-edge [23, 24]. It is usually assumed that the L-edge point at Brillouin zone holds 4 equivalent maxima along with a 2-fold spin degeneracy, leading to 8-fold degeneracy of the lowest excitonic transition [24–26].

2.2 Excitonic properties of PbS colloidal quantum dots

2.2.1 Excitonic transitions

In this section, we specifically discuss about the excitonic properties of PbS CQDs which emit the light across the infrared. Figure 2.5a shows a schematic of a PbS CQD along with a picture of a vial containing the dispersed PbS CQDs in toluene. Transmission electron microscopy (TEM) image of a single PbS CQD is illustrated in Figure 2.5b having a diameter size of 4.85 nm. As can be seen, the crystalline shape of the CQD is obvious. Figure 2.5c plots the absorption spectrum against wavelength, where the excitonic transitions are indicted by the arrows. Here, four lowest energy excitonic transitions are clearly distinguishable. The first excitonic feature, also known as band-edge state absorption, is indicated by $1S_h - 1S_e$. In addition, higher order excitonic transition occurs at higher frequencies where $1P_h - 1P_e$ corresponds to one-photon absorption (1PA) transition. While, two other transitions (dashed blue lines) occur at the energies where theoretical mode predicts only two-photon transitions are allowed [27]. Therefore, one can extract photo-physical behaviours of the CQDs by monitoring the excitonic features under optical or electrical excoriations. In the next section, we discuss about the different processes that can occur for an exction after generated under optical excitation.

2.2.2 Journey of an exciton

After creation of an exciton state in a CQD, different processes can be occurred, in which their time scale depends on the material properties. Radiatively recombination of electron and hole that results in emission of a photon, or nonradiative recombination that does not generate photons and the energy of recombination is released as heat.

Here, we consider the journey of an exciton in a PbS CQD as an exemplary case under optical excitation (see Figure 2.6). After creation of an exciton, the electron and hole are very rapidly relaxed to the band-edge state within a typical time scale of 10 ps, this process is called carrier cooling (Figure 2.6b). Another possible process in CQDs is capturing the carriers via trap/defect sites causing nonradiative recombination. Depending on trap-states density and energetics, the lifetime of this process can be varied from sub-ps to a few hundreds of ps. Figure 2.6d shows stimulated emission process, in which a photon stimulates an excited electron in CB to radiatively recombine and thus generate another photon. The generated two photons are identical in terms

of mode frequency, polarization, and propagation direction. The typical stimulated emission lifetime for un-engineered PbS CQDs is in less than 40 ps [28–30].

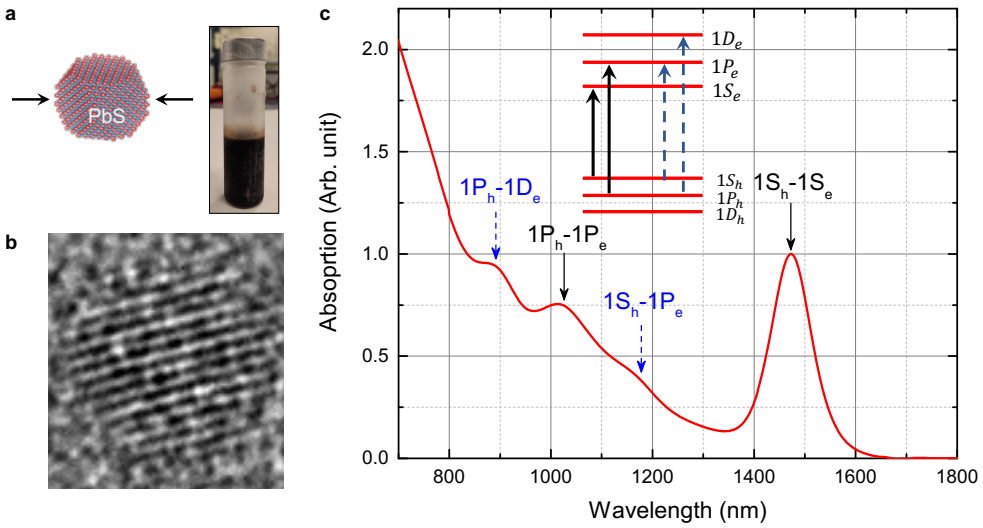

Figure 2.5: (a) Schematic representation of PbS CQD and a vial of PbS CQDs in toluene. (b) TEM image of PbS CQD. (c) Absorption spectrum as a function of wavelength, in which the first four excitonic transition are indicated by arrows. Inset shows a schematic of those excitonic transitions.

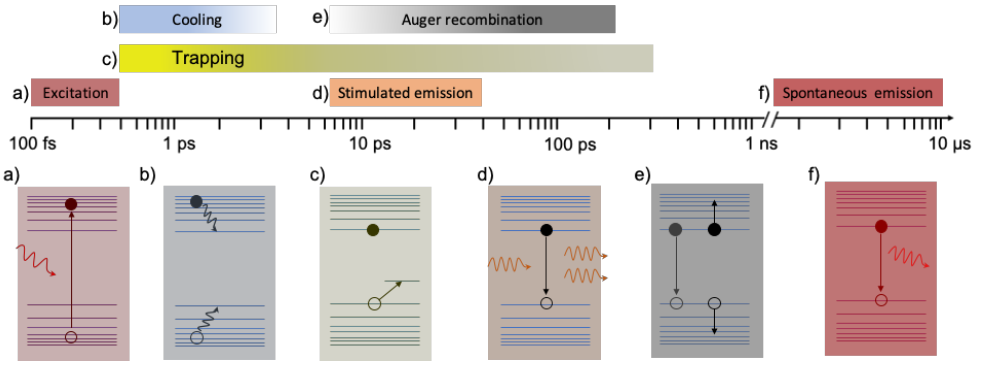

Figure 2.6: (a) excitation of the quantum dot under pulsed laser. (b) cooling process of excited exciton. (c) Trapping the holes in the trap states. (d) Stimulated emission, where an incident photon, produces an additional photon at the same frequency, polarization, and propagation direction. (e) Auger decay process, where the energy of an exciton recombination is transferred to either an electron or hole. (f) Spontaneous emission, where an electron and hole are radiatively recombined, results in randomly polarized photon.

This light amplification is the process that underpins lasing action. Another nonradiative recombination is Auger process, in which the released energy from recombination of electron and hole is transferred to another carrier either electron or hole, in which the energy dissipates as heat in the lattice. (Figure 2.6e) Also, the radiative recombination of a single exciton results in spontaneous emission (Figure 2.6f), the energy of the emitted photon equals the band gap energy of the semiconductor and it may have a random phase, polarization, and direction. If the energy of this process is provided by optical excitation, it is called photoluminescence (PL).

2.3 Optical gain in colloidal semiconductor quantum dots

2.3.1 Optical gain: fundamentals

In this section, we specifically discuss about the optical gain process which is the underlying principle for achieving lasing action. In principle, stimulated emission allows a photon in a given mode to trigger the excited electron in an upper energy to relax to the lower energy level, in which the process results in emitting another photon which maintains the same properties of the initial photon in terms of frequency, direction and polarization. Consequently, these two photons stimulate the emission of two additional photons while conserving the same characteristics. This process results in coherent optical gain.

Now, we discuss about three fundamental optical processes including spontaneous emission, stimulated emission, and absorption in an atom. For simplicity, we consider two-level system as shown in Figure 2.7. The carrier population in level 1 and level 2 is defined as N_1 and N_2, respectively. Therefore, the change of the population of the atoms in level 2 for spontaneous emission (SP) can be written as:

$$\frac{dN_2}{dt} = -P_{sp}N_2 \tag{2.5}$$

where, P_{sp} is the probability of spontaneous emission (per second) which can be expressed as: $P_{sp} = \frac{c}{V}\sigma_{21}(\nu)$, here c is the speed of light, V is the volume of a given cavity, and σ_{21} defined as transition cross-section between the energy level 2 and level 1. Therefore, by solving Equation 2.5, the number of atoms in level 2 can be described as $N_2(t) = N_2(0)e^{-t/t_{sp}}$, where t_{sp} is the spontaneous emission lifetime which is related

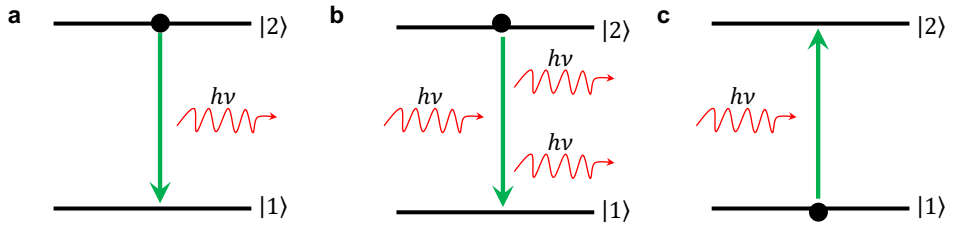

Figure 2.7: (a) Spontaneous emission of a photon having an energy of $h\nu = E_2 - E_1$. (b) Stimulated emission, in which one photon stimulates an excited electron in the upper level to emit another identical photon. (c) Absorption process of a photon with an energy of h leading to excite an electron from energy level 1 to energy level 2.

to the probability as:

$$P_{SP} = \frac{1}{t_{sp}} \tag{2.6}$$

Also, If the atom is excited by a monochromatic light in a given frequency ν, the stimulated emission (ST) rate from level 2 to level 1 (W_{21}) can be expressed as:

$$W_{21} = P_{st} = \phi\sigma_{21}(\nu) \tag{2.7}$$

ϕ is the photon flux density (photons/cm^2.s) which can be defined as $\phi = n\frac{c}{V}$ n is the number of photons in a given mode. $\sigma_{21}(\nu)$ is the effective stimulated emission cross-section. Similarly, the absorption rate (abs) from level 1 to level 2 (W_{12}) can be described as:

$$W_{21} = P_{abs} = \phi\sigma_{12}(\nu) \tag{2.8}$$

where, $\sigma_{12}(\nu)$ is the effective absorption cross-section between the states 1 and 2. The $\sigma_{21}(\nu)$ and $\sigma_{12}(\nu)$ are related to each other through the degeneracy of the level 1 and

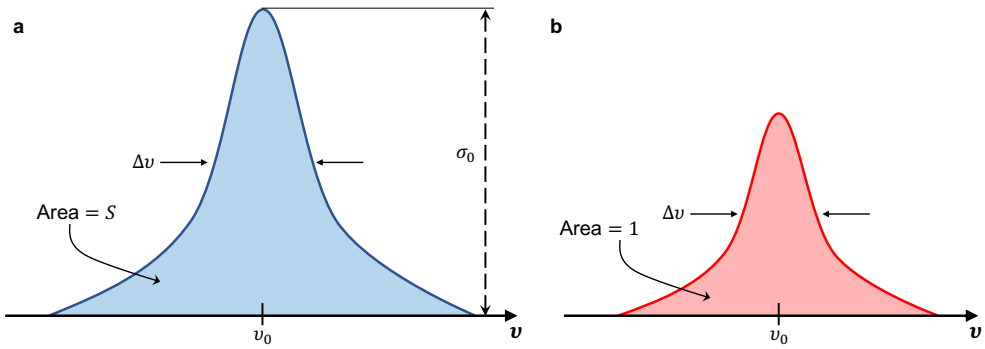

Figure 2.8: (a) The transition cross section $\Sigma(\nu)$. (b) The lineshape function $g(\nu)$.

level 2:

$$\sigma_{12}(\nu)g_1 = \sigma_{21}(\nu)g_1 \tag{2.9}$$

For simplicity, we assume $g_1 = g_2$. Also, the transition cross-section (stimulated emission or absorption) can be defined in terms of oscillator strength (S) and lineshape function ($g(\nu)$):

$$\sigma(\nu) = Sg(\nu) \tag{2.10}$$

The largest value for $\sigma(\nu)$ occurs at the resonance frequency ν_0 where the lineshape function is centered, and its value drops gradually as ν deviates from resonance frequency shown in Figure 2.8. Note, $\Delta\nu$ is the linewidth of lineshape function defined as the full-width at half-maximum (FWHM) of $g(\nu)$. By considering a three-dimensional cavity, where the density of modes can be calculated as $M(\nu) = 8\pi\nu^2/c^3$, the spontaneous emission rate can be defined as:

$$P_{sp} = \frac{1}{t_{sp}} = M(\nu_0)cS = \frac{8\pi S}{\lambda^2} \tag{2.11}$$

In the case of multimode polychromatic illumination ($\varrho(\nu)$) (energy per unit bandwidth per unit volume), in which the excitation signal is broadband with respect to the atomic

linewidth $\Delta(\nu)$. The stimulated rate can be written as:

$$W_i = B(\varrho(\nu_0)) \tag{2.12}$$

where $B = \frac{\lambda^3}{8\pi h t_{sp}}$ is the Einstein B coefficient which is related to the stimulated transition. Also, Einstein A coefficient that is defined as $A = P_{sp} = 1/t_{sp}$ is associated with spontaneous transition.

2.3.2 Optical gain mechanism in colloidal quantum dots

Solution-processed semiconductor quantum dots offer promising opportunities as an optical gain medium in solution-processable lasers that can be engineered via cheap and easily scalable chemical techniques [31, 32]. Owing to quantum confinement, their lasing emission can be precisely tuned from the visible [33–43] to the infrared [26, 28–30, 44, 45]. In addition to the size-dependent optical properties, CQD-lasers also exhibit lower operating lasing thresholds, high temperature stability compared to their bulk counterparts. These favorable properties stemming from their atomic-like discrete energy levels, in which large separation between electronic states impede thermal annihilation of the carriers at the band-edge [31, 46, 47]. This characteristic of the quantum confined systems was studied by Asada et al., where the maximum gain coefficient was calculated as a function of inject current density for four different material structure of $GaAs/Ga_{0.8}Al_{0.2}As$ (quantum-box, -wire, -film and bulk) as shown in Figure 2.9a [46]. In the same study, they also showed that the gain coefficient of $Ga_{0.47}Al_{0.53}As/InP$ enhances by increasing the confinement dimensionality (see Figure 2.9b).

Optical gain threshold

The light amplification in the CQDs can be modeled by approximating the first excited emitting state as a two-level system, in which its valence band (VB) state contains two electrons with opposite spins (see Figure 2.10a) It worth to mentioning that lowest-energy emitting state in common II-VI semiconductors (visible-emitting CQDs including CdSe, ZnSe, and CdS) show two-fold degeneracy, while infrared-emitting CQDs such as PbS and PbSe CQDs exhibit 8-fold degeneracy at the band-edge state. By absorbing the incident photon, one of the electrons promoted to the CB, results in generation of one exciton and is called single-exciton state (Figure 2.10b). This state can emit light as spontaneous emission; however it cannot provide optical gain, since the probability of the stimulated emission by the excited electron in CB state equals

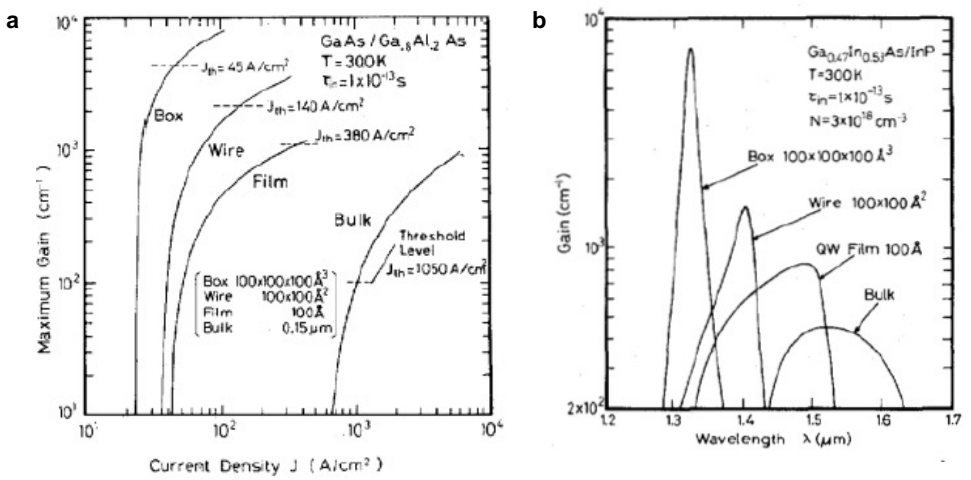

Figure 2.9: (a) Calculated peak gain coefficient versus injected current density for different quantum confinement (from bulk to quantum dot). Note, the dashed lines represent the required gain to achieve lasing action. (b) Theoretically predicted gain coefficient in $GaInAs/InP$ semiconductor with respect to different quantum confinement dimensions. [1986] IEEE Reprinted, with permission, from [M. Asada, Y. Miyamoto, Y. Suematsu, Gain and the threshold of three-dimensional quantum-box lasers, IEEE Journal of Quantum Electronics, and September/1986]

to the absorption of the remaining in the VB state. Therefore, net optical gain can be achieved if both electrons in the VB state are excited to the CB, indicating population inversion is essential for realization of lasing action in CQDs (see Figure 2.10c).

Therefore, the optical gain threshold for a simplified case of excitons distribution in two-fold degenerate system $g_e = g_h = 2$ where (g_e and g_h is the degeneracy of electron and hole in the CB and VB state, respectively) can be calculated from the following expression:

$$\langle N_g \rangle = \frac{g_e g_h}{g_e + g_h} \tag{2.13}$$

here, we assume charge neutral CQD, $\langle N_e \rangle = \langle N_h \rangle = \langle N \rangle$. Then, the optical gain threshold in two-fold system is $\langle N_g \rangle = 1$, whereas for 8-fold degenerate ($g_e = g_h = 8$) system $\langle N_g \rangle = 4$. In the case of optical excitation with high-energy, the excitation across the ensemble of CQDs follows Poisson statistic [42]:

$$P(n) = \frac{e^{-\langle N \rangle} \langle N \rangle^n}{n!} \tag{2.14}$$

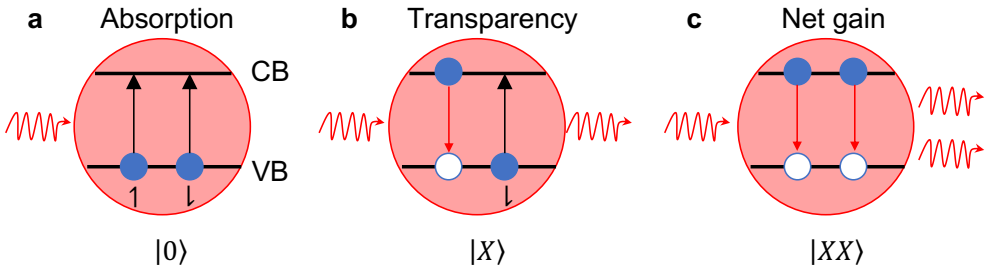

Figure 2.10: Optical gain model in a CQD. Note, for the simplicity the band-edge state of the CQD is modeled as a two-level system hold two-fold degeneracy in CB and VB states. In the ground state (a), both electrons with the opposite spin can absorb the incident light. In single-exciton state (b), when an electron is excited to the CB, the energy from the recombination of e–h pair is absorbed by the remaining electron in the VB. This condition called as optical transparency. In biexciton state (c), in which two electrons are excited to the CB, then the ground-state absorption is blocked which the condition called as population-inversion. In this condition the incident photon can induce stimulated emission, in which the radiative recombination of the biexciton results in stimulated emission.

here $P(n)$ is the probability of finding a CQD having n excitons when the average excitonic occupancy per CQD is $\langle N \rangle$. Then, the probability of finding more than 2 excitons in an ensemble of CQDs (P_{xx}) can be written as: $P_{xx} = 1 - P_x - P_0$, where P_x and P_0 is the probability of finding 1 and 0 exciton per-dot, respectively. In the case of two-fold system, the net gain coefficient is determined by the difference of biexciton and ground state: $G = (P_{xx} - P_0)\sigma(\nu)$ [42]. From Equation 2.14, $P_0 = e^{-\langle N \rangle}$ and $P_x = P(1) = \langle N \rangle e^{-\langle N \rangle}$. Therefore, the gain threshold for two-fold degenerate system under optical excitation is $P_{xx} = P_0$, where $P_{xx} = 1 - e^{-\langle N \rangle} - \langle N \rangle e^{-\langle N \rangle}$. By substituting the expression, the gain threshold in terms of averaged number of excitons per-dot is $\langle N_g \rangle = 1.15$. Furthermore, using Equation 2.14 for 8-fold degenerate system (e.g., Pb-chalcogenide CQDs), the optical gain threshold under optical excitation equals to $\langle N_g \rangle$ =4.04 [29, 48].

Optical gain and lasing challenges: Auger recombination

The multiexcitonic nature of the light amplification in CQDs suggest that the optical gain kinetics are typically controlled by multiexciton recombination not single-exciton decay. This is associated with a nonradiative recombination called Auger process [21, 40, 49–53], which results in high lasing thresholds and ultrashort gain lifetime. In this process, the energy from recombination of an exciton does not emit light, instead the released energy is transferred to a third carrier such as electron in the CB or hole in the VB state (see Figure 2.11b). In epitaxial grown QDs, Auger process is not a limitation

factor for lasing, since radiative recombination is faster than Auger recombination [31]. On other hand, Auger process in un-engineered CQDs show very fast relaxation time which is orders of magnitude faster than stimulated emission [31, 40, 49]. Previous studies showed that Auger recombination lifetime in CQDs follows a linear function of CQD volume, is referred as V-scaling [31, 40]. Interestingly, this behavior was observed in almost all kind of semiconductor NCs including CdSe, InAs, PbSe, PbS, Si and Ge [28, 36, 41, 49, 50, 54, 55]. The implication of Auger recombination for CQD lasing was firstly discussed by Klimov et al., in which authors reported amplified spontaneous emission (ASE) as a first account under high pumping intensities using short pulse excitation to reduce Auger effect during the pumping [40]. However, Auger process acts as the major obstacle for the realization of practical lasers including continuous wave and electrically-pumped lasers based on CQDs. Thus, manipulating Auger decay has been at the center of attention for lasing application.

Effect of Auger process on optical gain thresholds

As discussed above, the gain threshold under pulsed-excitation for 2-fold degenerate system is $\langle N_g \rangle = 1.15$. Besides,$\langle N \rangle$ can be translated into the pump fluence: $\langle N \rangle = f \times \sigma_a(\nu)$, here f is the fluence (joule/unit area) and $\sigma_a(\nu)$ is the frequency-dependent absorption cross-section (unit area). The gain threshold in terms of per-pump fluence (f_g) equals to f_g =1.15 $h\nu_p/\sigma_a(\nu)$. Thus, in the case of ultra-shot pulsed-pumping ($\tau_p \ll \tau_A$), Auger process does not affect the optical gain threshold. As a result, f_g is primarily determined by the absorption cross-section, which is directly related to the volume of the CQDs [31, 56].

Effect of Auger recombination on ASE and lasing thresholds

In contrast to optical gain threshold, ASE and lasing thresholds are characterized by Auger recombination. Previously, Park et al. introduced a truncated-energy-spectrum mode to quantitatively analyze the effect of Auger process on CQDs lasing [56]. In the case of lasing, stimulated emission primarily must compete with reabsorption losses through the gain medium (indicating the gain threshold), another loss mechanism has been induced due to photon escaping from the cavity [56]. To assess the effect of Auger recombination on the lasing threshold, the authors considered a coupled CQD-cavity system, in which CQDs were modeled as a three-level with a 2-fold degeneracy gain system. The results show that the lasing threshold in terms of average number of

excitons ($\langle N_{las} \rangle$) can be defined as [56]:

$$\langle N_{las} \rangle = 1 + \sqrt{\frac{\tau_{se}}{\tau_A}} \tag{2.15}$$

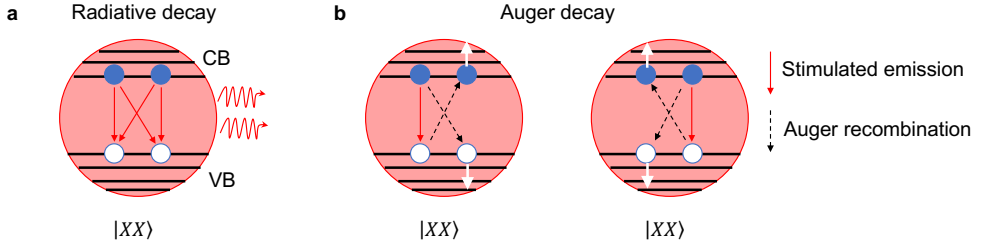

Figure 2.11: (a) Radiative emission of the biexciton state, results in stimulated emission (red arrows). (b) Cartoon of Auger recombination, in which the energy of e–h recombination (red arrows) is nonradiatively transferred (dashed black arrows) to a third carrier.

where τ_{SE} and τ_A are defined as stimulated emission in the cavity and Auger decay lifetime, correspondingly. Note, to simplify the calculations, the cavity was considered to be lossless, where i.e. the cavity lifetime ($\tau_c \longrightarrow \infty$). Then, for realization of the lasing action; lasing lifetime (τ_{las}) needs to be shorter than τ_A. Note, lasing lifetime is approximately defined as stimulated emission lifetime in a lossless cavity, where by decreasing τ_A, obtaining lasing action requires higher stimulated emission rates leading to greater lasing thresholds (as shown in Equation 2.15) [56].

Engineering CQD properties for reducing lasing threshold

As discussed earlier, the gain/lasing thresholds are determined by the absorption cross-section ($\sigma_a(\nu)$) which directly scales with the volume of the CQD. In doing so, one may use core/shell heterostructure, in which the small band-gap emitting core is enclosed by a wider band-gap shell semiconductor which acting as a light harvesting region. In addition to increasing $\sigma_a(\nu)$, employing core/shell architecture allows to manipulate the wavefunctions of the carriers (see Figure 2.12). Depending on the band-edge offset between the core and shell materials, various types of heterostructures will be created including type-I, type-II and quasi-type-II electronic band-alignment (see Figure 2.13). As shown in Figure 2.13a, both electron and hole wavefunctions in type-I heterostructure are confined inside the core region with a slight tunneling to the shell region.

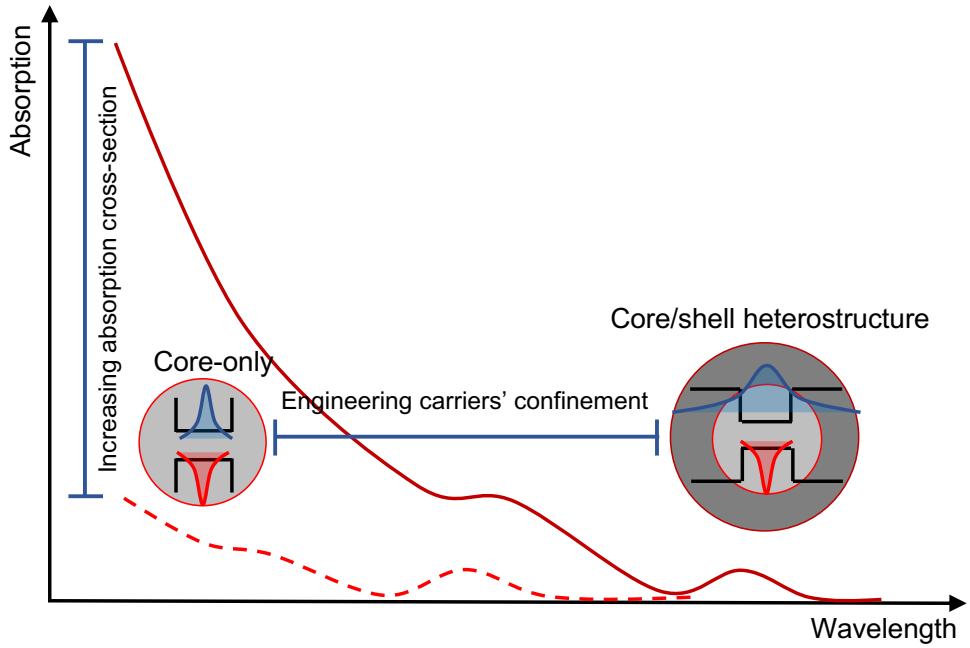

Figure 2.12: Engineering CQD by manipulating its shape and composition. In core/shell heterostructure, a smaller band-gap material (i.e., core) is surrounded by a wider band-gap semiconductor (i.e., shell). Note, blue wavefunction represents electron wavefunction and the red is for hole wavefunction

The first successful demonstrations of type-I core/shell CQD heterostructures were performed by growing ZnS shell on top of CdSe core [57,58]. In type-II heterostrcuture (Figure 2.13b), the charges are separated from each other, where the hole wavefunction completely moves to the shell region while electron wavefunction is confined in the core material. It is worth to mention that this type of wavefunctions localization enhances the repulsive Coulomb interaction between generated excitons and reduces the Coulomb attraction. This type of band alignment previously was shown in CdSe/CdTe core/shell CQDs [59]. Core/shell heterostructure with quasi-type-II electronic band-alignment results in delocalization of one of the wavefunctions over the entire CQD while the other one is confined in either core or shell material. For instance, CdSe/CdS CQDs have been mostly studied quasi-type-II material among limited number of choices [60,61].

Recently, some efforts have been conducted to reduce the lasing threshold in CQDs including increasing absorption cross-section of the CQDs using large-volume core/shell CQDs [34,62–64] and the suppression of Auger recombination by engineering the shape of potential confinement in the core/shell heterostructure through "smoothening" of the confinement [56,65–67]. As theoretically predicated by Cragg and Efros, smooth-

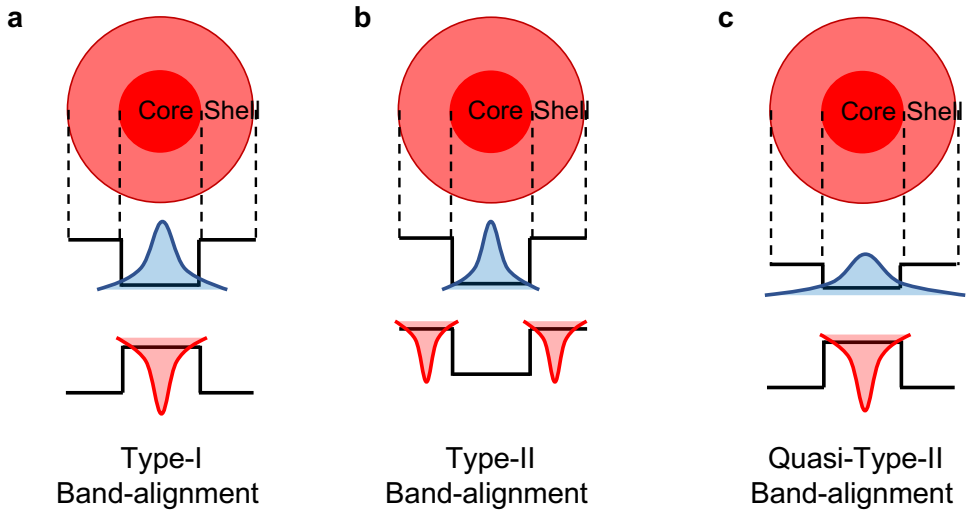

Figure 2.13: Core/shell CQD heterostructure having various electronic band-alignment (a) Type-I, (b) Type-II and (c) Quasi-Type-II

ing the potential confinement at the interfaces of the core/shell heterostructures can reduce the rate of the intra-band transitions involved in Auger process as an energy-accepting carrier either electron or hole [68]. Thanks to this, the reported value for Auger decay lifetime in such a structure is longer than the conventional core/shell structures with abrupt interface. For instance, Kilmov et al. reported the bi-exciton lifetime for core/shell and core/alloyed-shell CQD heterostructures with the same core radii (r_c =1.5 nm) and the same total radii (r_t =7 nm). Here, an alloyed composition of CdS_xSe_{1-x} with a thickness of 1.5 nm is introduced between CdSe core and CdS shell. In this study, they employed single-particle spectroscopic method to extract single-exciton and bi-exciton kinetics. The results are shown in Figure 2.14, in which the bi-exciotn lifetime (Figure 2.14c and g) in alloyed CQD is 4-fold longer than core/shell with abrupt interface [65]. Additionally, manipulating the confinement potential CQDs allows to obtain significant suppression of Auger recombination whereas preserving the strong quantum confinement. However, this property is not achievable in large-volume CQDs, wherein the suppression of Auger decay is accompanied by reducing the spatial overlap between the electron-hole due to unfavorable losing of the confinement energy [31].

Additionally, some other parallel efforts have focused on engineering the absorption cross-sections of the NCs toward achieving large-volume structures including nanoplatelets heterostructures [36, 38, 69, 70], core/giant-shell CQDs [62], large perovskite NCs [39], quasi-2D [71], nanowires [72] and dot/rod [41] heterosructures. By

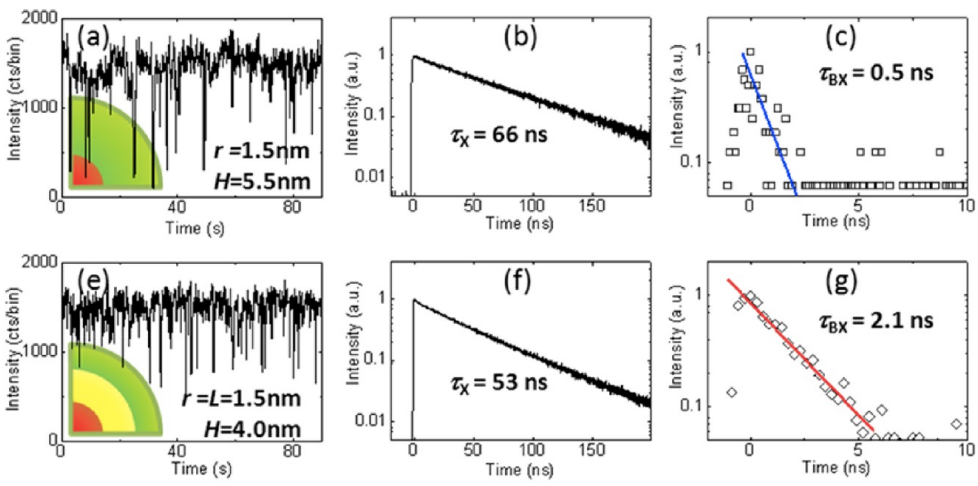

Figure 2.14: PL intensity of a single CQD along with time-correlated single-photon counting (TCSPC) measurements for core/shell (a-c) and core-alloyed (e-g) heterostructures. Reprinted with permission from [65]. Copyright 2014 American Chemical Society

considering $\langle N \rangle = f \times \sigma_a(\nu)$, in a given $\langle N \rangle$, increasing $\sigma_a(\nu)$ leads to lower pump intensities.

Novel optical gain mechanism

Single-exciton gain mechanism. Novel lasing mechanism has been introduced for lowering the optical gain/lasing thresholds. One of the promising approaches is obtaining stimulated emission in single-exciton regime, in which the Auger decay is inactive. In doing so, two different methods have been introduced in the literature: 1) controlling the exciton–exciton (X–X) interaction, in which because of strong X–X repulsion, the emission from the recombination of the bi-exciton state is not absorbed by ground-state [59, 73, 74] which is achieved in type-II heterostructure such as CdS/ZnSe core/shell [59]. 2) controlling the Stokes shift of the stimulated emission compared to the ground-state absorption [36, 41, 43].

Using charged CQDs as the gain media. The opportunity of strongly suppressed Auger decay in CQDs developed an interest to consider novel gain mechanism. In particular, charging the CQDs with permanent electrons or holes, can potentially reduce the optical gain threshold [37, 42]. The principle of this approach underpins on partially/totally blocking the ground-state absorption. The concept of using charged CQDs for reducing the gain threshold is depicted in Figure 2.15 for two-fold CQD system. In CQDs with one extra electron (Figure 2.15a), the ground-state absorption is partially blocked due to pre-existing electron in the CB. Therefore, generating one-exciton should be enough to achieve stimulated emission. Furthermore, introducing

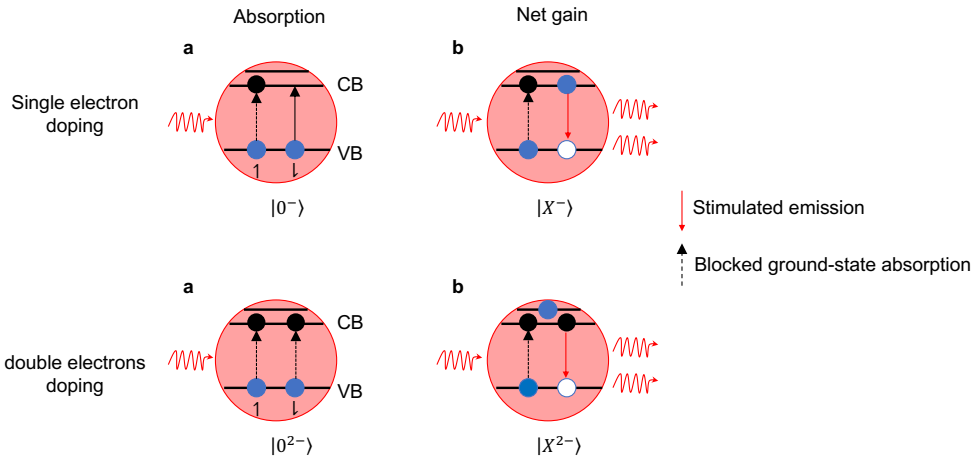

Figure 2.15: The concept of doping in two-fold system. The top panel is for single-electron doped CQD and the bottom panel shows a CQD with two extra electrons. The solid black and red arrows represent stimulated emission, respectively, Note, black dashed-arrows correspond to blocked ground-state absorption.

two permanent extra electrons results in totally blocking the ground-state absorption, which implying "zero-threshold optical gain" [42]. Hence, the gain threshold formula in Equation 2.13 in the presence of permanent electrons can be written as the following expression:

$$\langle N_g \rangle = \frac{(g_e - n_e)g_h}{g_e + g_h} \tag{2.16}$$

here, n_e, is the average number of pre-existing electrons per-dot. For the first time, Klimov et al. employed this approach to reduce the optical gain threshold as low as $\langle N_g \rangle = 0.02$ when $\langle n_e \rangle = 6$ [42]. In this study, they used photochemical doping method to introduce the permanent charges. In addition to reducing the gain threshold, using doping strategy leads to achieve longer optical gain lifetime compared to the neutral bi-exciton gain system. For instance, the gain lifetime of the especially engineered CdSe-based CQDs with one extra electron and two extra electrons were reported to be 4.5 and 2.5 ns, respectively. While, undoped-CQDs showed an optical gain lifetime of 1.5 ns [42].

Infrared optical gain in colloidal quantum dots

The best developed IR-emitting CQDs are Pb-chalcogenides (e.g., PbSe and PbS CQDs). These NCs have been extensively utilized in light-harvesting applications [23, 75, 76].

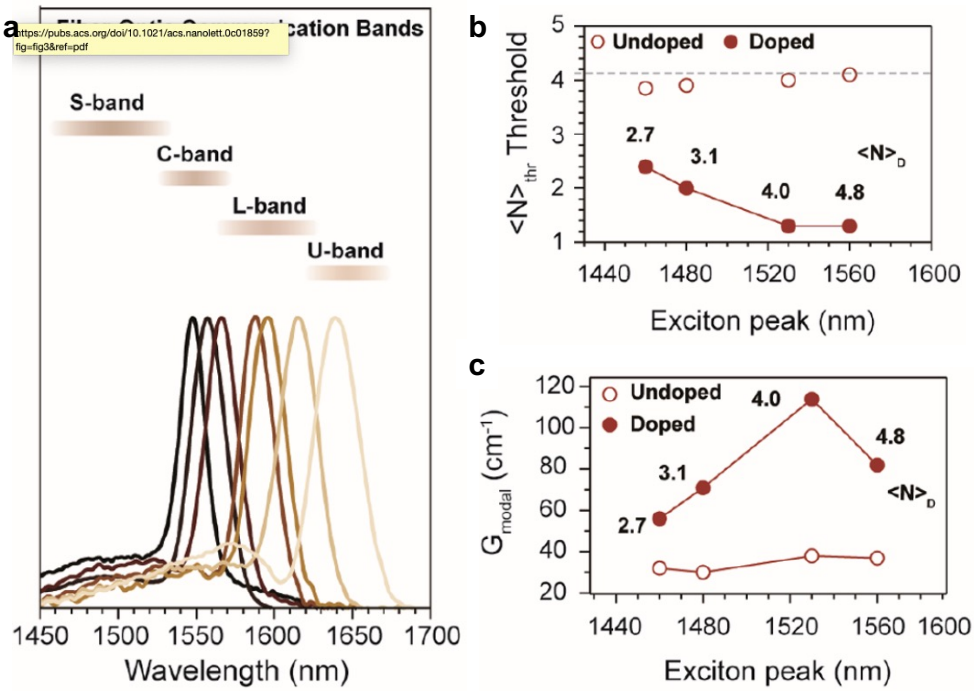

Figure 2.16: (a) Tuneable infrared ASE spectra across the telecommunication band using different size of PbS CQDs. (b)$\langle N_{th} \rangle$ as a function of the excitonic peak of the employed CQDs. (c) Net modal gain coefficient for doped and undoped CQDs. Reprinted with permission from . Copyright 2020 American Chemical Society

However, their optical gain performance has been limited because of 8-fold degeneracy of their band-edge state. As discussed earlier, the gain threshold is 4 excitons per-dot, leads to very fast Auger decay since its lifetime scales with the number of excitons [77]. Recently, Christodoulou et al. reported room-temperature tuneable stimulated emission across the telecommunication band using different sizes of the surface-treated PbS CQDs. Particularly, they applied a ligand exchange procedure, in which the ligand is a hybrid of ZnI_2/MPA. This ligand exchange action allowed them to electronically doping PbS CQDs, leading to reduce the ASE threshold down to ∼1.5 excitons per dot. Figure 2.16 shows the results of this study [29]. This study showed interesting results and demonstrates the capability of using CQDs as a gain media in the infrared lasers. However, their performance suffer from very high pumping intensities, very short gain lifetime and low net modal gain, precluding them from reaching a stage for practical applications.

2.4 Laser amplification in colloidal semiconductor quantum dots

2.4.1 Laser amplification: fundamentals

In this section, we discuss about the theory of laser amplifiers. Figure 2.17 depicts the variation ($d\phi$) of an input photon flux (ϕ) after travelling a distance of dz in the gain medium. It is assumed that some of the atoms in the gain medium are in the excited state that potentially can make stimulated emission. Also, the incoming light can be absorbed by the medium. The former results in amplification, while the latter leads to attenuation of the input signal. The rate of these process can be expressed as $W_i = \phi\sigma(\nu)$. Assuming the two-level system, the average density of the absorbed photons is $N_1 W_i$, and the average density of the stimulated emission is $N_2 W_i$. Therefore, the changes of the photon flux can be written as:

$$d\phi = (N_2 - N_1)W_i dz = N\phi\sigma(\nu)dz \tag{2.17}$$

here, $N = N_2 - N_1$ is referred as the population inversion condition, in which the gain medium can potentially act as a light amplifier. If $N < 0$, the medium attenuates the input signal which reduces the flux density at the output. The $N = 0$ is the transparency condition, in which the photon flux remains constant. By solving Equation 2.17, the photon flux density in the medium can be expressed as:

$$\phi(z) = \phi(0)exp(N\sigma(\nu)z) = \phi(0)exp(Gz) \tag{2.18}$$

here in, the gain coefficient is defined as $G = N\sigma(\nu)$ representing the light amplification per unit length.

Rate equations

Now, we discuss rate equations to understand the kinetics of optical gain in terms of population densities of the atomic levels, radiative and nonradiative recombinations. In doing so, we start with a two-level system in the presence of amplifier radiation $W_i = \phi\sigma(\nu_{(0)}) = W_{st} = W_{abs}$. As schematically depicted in Figure 2.18, level 1 is the atomic ground state, and level 2 is the atomic excited state. The rate equations for

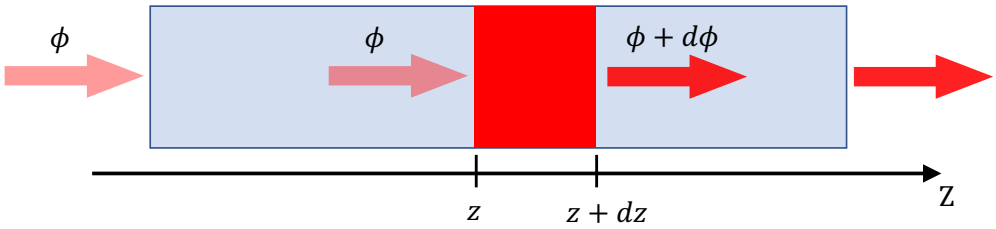

Figure 2.17: Schematic of photon flux density ϕ (photons/cm2.s) entering a medium, in which it changes to $\phi + d\phi$ after traveling dz inside the gain medium.

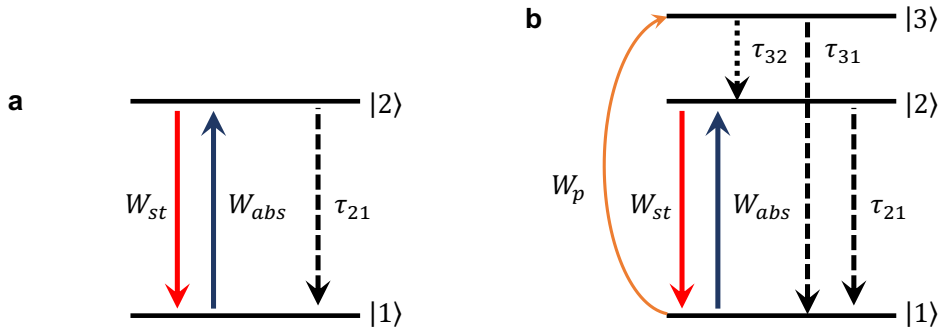

Figure 2.18: optical gain systems for two-level system (a), and three level system. Note, the population densities (N) of the energy levels are determined by the processes of pumping rate W_p, the rate of the stimulated emission W_{st} and the absorption transition W_{abs}, and the decay of the excited states.

this system under optical excitation can be written as:

$$\frac{dN_2}{dt} = W_{abs}N_1 - W_{st}N_2 - \frac{N_2}{\tau_{21}} \tag{2.19}$$

$$\frac{dN_1}{dt} = \frac{N_2}{\tau_{21}} + W_{st}N_2 - W_{abs}N_1 \tag{2.20}$$

for the steady state condition ($\frac{dN_{1,2}}{dt} = 0$), the relation between N_1 and N_2 can be expressed as:

$$N_2 = \frac{W_{st}}{W_{st} + 1/\tau_{21}} N_1 \tag{2.21}$$

Therefore, $N = N_2 - N_1 \leq 0$ means that two-level system cannot achieve population inversion condition, then net gain is not possible in such a system.

Gain action in three-level system occur between level 2 (metastable state) and level 1 (ground state) as shown in Figure 2.18b, in which excited atoms in level 3 decay very fast to level 2 (τ_{32} is very small).

$$\frac{dN_3}{dt} = W_p N_1 - \frac{N_3}{\tau_{32}} - \frac{N_3}{\tau_{31}} \tag{2.22}$$

$$\frac{dN_2}{dt} = \frac{N_3}{\tau_{32}} + W_{abs} N_1 - W_{st} N_2 - \frac{N_2}{\tau_{21}} \tag{2.23}$$

$$\frac{dN_1}{dt} = \frac{N_3}{\tau_{31}} + \frac{N_2}{\tau_{21}} + W_{st} N_2 - W_{abs} N_1 - W_p N_1 \tag{2.24}$$

here τ_{21} is the lifetime of the level 2 including radiative and nonradiative transitions. Since τ_{32} is very small, we assume $N_3 = 0$. Then, $N_3 + N_2 + N_1 = N_a$ turn to $N_2 + N_1 = N_a$ where N_1 is the total population density. After solving Equations 2.22-2.24 under steady state condition, population difference $N = N_2 - N_1$ can be written as:

$$N = \frac{W_p - 1/\tau_{21}}{2W_{st} + W_p + 1/\tau_{21}} \tag{2.25}$$

here, under small gain assumption (i.e., $W_{st} = 0$), then gain coefficient can be written as:

$$G = (\frac{W_p - 1/\tau_{21}}{W_p + 1/\tau_{21}}) N_a \sigma_{21}(\nu) \tag{2.26}$$

Therefore, in a three-level system, the net gain threshold is $W_p = 1/\tau_{21}$, where above this threshold stimulated emission is achievable.

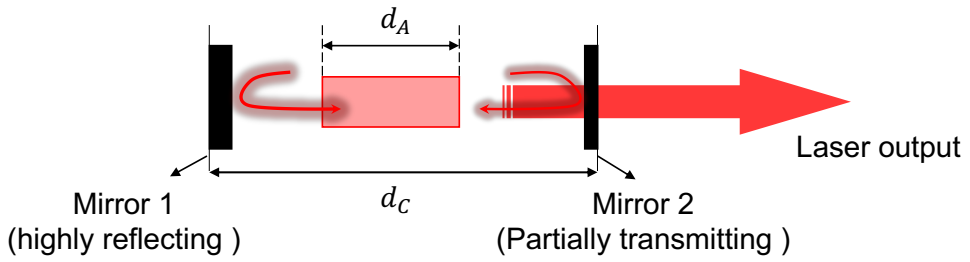

Figure 2.19: A laser oscillator consists of a light amplification material having thickness of d_A is placed in an optical resonator with a thickness of d_c. Note, the reflectivity of mirror 1 and mirror 2 are R_1 and R_2.

Laser oscillator

Next, we introduce a basic laser amplifier where the gain medium is placed between two mirrors (see Figure 2.19), in which the gain coefficient and total loss coefficient of the medium defined as G and α, respectively. For realizing lasing action in this cavity, the gain coefficient should overcome the total loss of the cavity (α_{tot}) including attenuation coefficient of the gain medium (α) and the mirror losses (α_m). Lasing threshold for a round trip can be calculated from the following expression:

$$R_1 R_2 exp((G - \alpha_{tot})2d_c) = 1 \tag{2.27}$$

here, $\alpha_{tot} = \alpha + \alpha_m = \frac{1}{2d_c}(ln(\frac{1}{R_1}) + ln(\frac{1}{R_2}))$, By substituting α_{tot} in Equation 2.27:

$$G = \frac{1}{2d_c} ln \frac{1}{R_1 R_2} + \alpha \tag{2.28}$$

Since α_{tot} is the total loss of energy per unit length in the cavity, then the total loss of photons per second is defined as $\alpha_{tot} c_n$, resulting the cavity photon lifetime of:

$$\tau_c = \frac{1}{\alpha_{tot} c_n} \tag{2.29}$$

where c_n is the speed of light in the cavity. Also, the quality factor (Q) of the cavity

can be calculated from the spectral analysis of the cavity output:

$$Q = \frac{\nu_0}{\Delta\nu} \tag{2.30}$$

by defining $\Delta\nu$ as the linewidth of the cavity resonance mode. Then, Q is related to the cavity photon lifetime as $Q = 2\pi\nu\tau_c$.

2.4.2 Colloidal semiconductor quantum dot lasers

In this section, we discuss about the lasing action in CQDs. Following the first successful demonstration of room-temperature CQD lasing in the visible regime [43], this field has experienced extraordinary progress. Recent advances in CQD synthesis along with the device engineering led to achieve several state-of-the-art results including optically-excited CW lasing [35, 78], and the realization of a dual functional electroluminescent devices which also operates as a laser under the optical excitation [79].

Up to date, to realize optically-pumped CQD lasing, various cavity designs have been explored including Fabry–Perot [43], whispering-gallery mode [80], vertical-cavity surface-emitting (VCSEL) [34], microring [81], and distributed feedback (DFB) resonators [35, 37, 82]. Among those, DFB lasers show low lasing thresholds, high modal selectivity and compatibility with solution-processed gain media [35, 79, 82]. DFB-lasers are considered as the ideal industrially relevant optical resonator to realize practical CQD-lasers.

Following the demonstration of tuneable infrared stimulated emission between 1.5-1.6 μm using PbS CQDs, we coupled this gain media to a DFB cavity for realization of the first room-temperature infrared lasers in the eye-safe window [44]. We employed sapphire (Al_2O_3) as the substrate which shows high thermal conductivity. In doing so, we fabricated the gratings on top of Al_2O_3 using electron beam lithography and subsequent reactive-ion etching, schematically shown in Figure 2.20a. Then, PbS CQDs were transferred on top of the grating via spin-coating technique. Figure 2.20b depicts DFB laser under optical excitation. To tune the lasing emission, we varied DFB grating period and used different size of PbS CQDs which provide ASE signal at different wavelengths. As a result, we precisely tuned the lasing from the central C-band to the ultra-long U-band of the infrared regime, where the results shown in Figure 2.20c. Summary of the corresponding lasing thresholds are plotted in Figure 2.20d, in which the lasing threshold varied from 800 to 2000 μJ.cm^{-2}. Although, our results in this work showed the feasibility of using CQD for true lasing action in the infrared, their

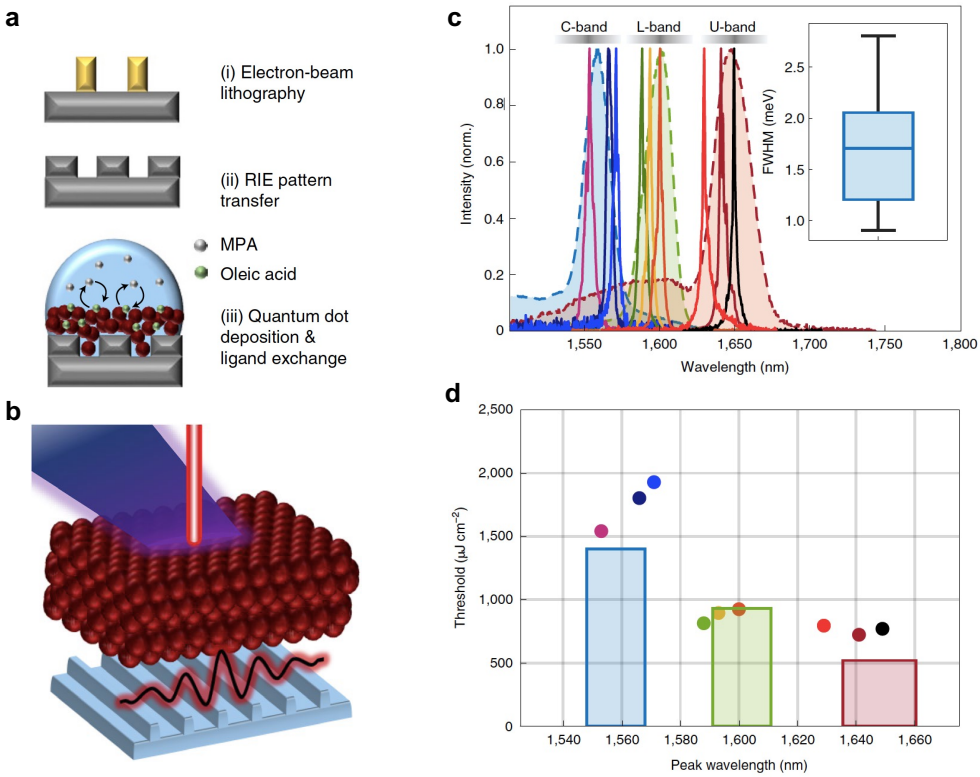

Figure 2.20: CQD-DFB infrared lasers. (a)Schematic work flow of the fabrication process used for the CQD DFB lasers. (b) Diagram illustrating DFB lasing. (c) Infrared lasing tunablity with correponding ASE spectra. Note, inset shows a summary of DFB lasers linewidth. (d) Plot of the measured lasing threshold as function of peak wavelength position of each DFB laser are shown in b. Reprinted with permission from [44]. Copyright 2021 Nature Photonics, Springer Nature.

lasing thresholds are orders of magnitude higher than their visible counterparts.

In this thesis, we aim to further develop CQD infrared lasers taking advantageous of a large arsenal of previously established synthetic tools in the visible-emitting CQDs system. Besides, we will introduce new approaches and methods to address the fundamental challenges of PbS-based CQDs for realization of high performance infrared lasers. In addition to improving material properties, we will focus on device engineering to overcome the practical challenges to realize the "Holly Grail" in the CQDs field, which is the realization of CQD laser diodes.

3

Low-threshold infrared laser: Engineering PbS colloidal quantum dots at supra-nanocrystalline level

"Measure what is measurable, and make measurable what is not so."

-Galileo Galilei

In this chapter, we disclose a novel approach to engineer the single- and multi-excitonic properties of PbS CQDs as the gain medium for the short-wave infrared (SWIR) laser. Here, we show manipulation of Auger decay in PbS CQDs at the supra-nanocrystalline level via a robust method. This leads us to achieve a low-threshold and highly-stable SWIR laser, operating in the U-band of the telecommunication window.

This chapter is based on the publication "Low-Threshold, Highly Stable Colloidal Quantum Dot Short-Wave Infrared Laser enabled by Suppression of Trap-Assisted Auger Recombination," N. Taghipour, G. L. Withworth, A. Othonos, M. Dalmases, S. Pradhan, Y. Wang, G. Kumar and G. Konstantatos, Advanced Materials 34, no. 3, pp. 2107532 (1–8), (2022). Adapted or Reproduced with permission from John Wiley and Sons. Copyright 2022. Wiley-VCH Verlag GmbH & Co. KGaA. Weinheim.

3.1 Motivation

As we discussed earlier, CQDs have shown great promise to use as gain media in solution-processed lasers. Thanks to quantum confinement effect, their excitonic properties can be precisely tuned via manipulating their sizes, compositions and shapes. CQD-based optical gain media enabled full-color lasers, in which the lasing emission can be precisely conrolled from the visble to the infrared. However, their optical amplification action is limited by Auger decay, where its ultrafast nature leads to annihilation of the carriers before those recombine radiatively [77]. In particular, the effect of Auger on lasing action was evidenced by a very high lasing thresholds and heat generation that precludes practical CQD-laser devices [18, 21, 31, 32, 36, 37, 42]. This is originally raised from the non-unity degeneracy of the band-edge state which is involved in the lasing action. Therefore, the Auger process in 8-fold degenerate infrared-emitting CQDs (e.g., IV-VI semiconductors) is more problematic than the visible CQDs (e.g., II-VI semiconductors) with 2-fold degeneracy. As discussed in the previous chapter, recent advances in the synthesis of Cd-based CQDs have led to the suppression of Auger for the realization of high performance visible lasers. On other hand, recently reported infrared ASE and lasing in PbS CQDs exhibit high thresholds which are attributed to very fast Auger recombination and high degeneracy of PbS CQDs [26, 29, 44]. One of the origins for fast Auger recombination in PbS CQDs is the existence of active mid-gap traps which capture the generated carriers, resulting in long-lived net charges in CQDs. The long-lived charges increase the probability of nonradiative Auger recombination, known as trap-assisted Auger decay [83–85].

Hence, passivation of the trap states should lead to suppress trap-assisted Auger process, thereby realizing high-performance laser devices. Given this, several studies have attemptted to passivate the trap states in infrared emitting CQDs via a chemical approach including core/shell heterostructures [86, 87], mixed organic-inorganic ligand treatment [88–91] and embedding CQDs in perovskite matrix [92]. Additionally, the remote charge passivation method has been considered a promising mechanism that is more efficient and robust compared to the chemical passivation [93–95]. Although this method has been successfully implemented in optoelectronic devices including LEDs and photovoltaics, operating in the single-exciton regime, its effect on multiexciton level relevant to lasing action has not been explored yet.

3.2 Results and discussion

In this part of the thesis, we achieved low-threshold lasers operating in the optical communication window with unprecedented operational stability. To do so, we employ a binary nanocomposite of PbS CQDs and ZnO NCs, in which the former acts as the infrared gain media, and the latter as remote passivant for in-gap trap states in PbS CQDs. The combination of these two nano-sized species drastically suppresses the trap-assisted Auger recombination, where its lifetime is prolonged by five-fold compared to bare PbS CQDs [29]. This results in a two-fold reduction of the ASE threshold, reaching down to $\backsim 430 \mu J.cm^{-2}$. By integrating this novel gain media into a DFB cavity, we realize a single-mode infrared laser operating at 1650 nm within a linewidth of 1.23 nm, and a record low threshold of $\backsim 385 \mu J.cm^{-2}$, which surpasses those of previous reports in PbS CQDs (800-2000 $\mu J.cm^{-2}$ [44]). This study discloses a novel method for engineering nanocrystalline solids for high-performance CQD-lasers and demonstrates that CQDs can be exploited as low-cost solution-processable and versatile gain medium for the lasers, operating at the telecommunication window.

As discussed earlier, the presence of mid-gap trap states in PbS CQDs causes fast trap-assisted Auger recombination which is expected to hamper efficient optical amplification [84, 85, 96, 97] Here, we posit that reducing the density of trap-states in PbS-emitter CQDs induced by a large band-gap electron rich ZnO NCs would enable us to engineer trap-assisted Auger decay leading to achieve low ASE and lasing thresholds. The concept of manipulating the trap-assisted Auger process at the supra-nanocrystalline level is schematically shown in Figure 3.1. Common Auger recombination (Figure 3.1a), the so-called trimolecular process, is an intrinsic material process that depends on the level of the excitation regardless of the number of trap states. Figure 3.1b illustrates another type of Auger process, which is mediated by the mid-gap trap states, which can be distinguished by its bimolecular kinetics [83–85]. These bimolecular Auger processes dominate the non-radiative recombination in the saturation pump fluence regime where, the number generate charge-carriers, defined as Δn, is much greater than the concentration of trap states, n_1, p_1 ($\Delta n \ll n_1, p_1$ [84,96]). At the fluences needed to observe ASE/lasing in PbS-emitter CQDs, the bimolecular Auger is the dominant nonradiative process. Therefore, to obtain an efficient infrared laser based on PbS CQDs, it is essential to suppress the trap-assisted Auger recombination. In our proposed binary blend architecture (Figure 3.1c), by bringing ZnO NCs in the vicinity of PbS- emitter CQDs, the deep electron acceptor sites (defined as mid-gap trap states) of PbS CQDs are passivated by the transferred electrons from electron-rich ZnO NCs [94, 95].

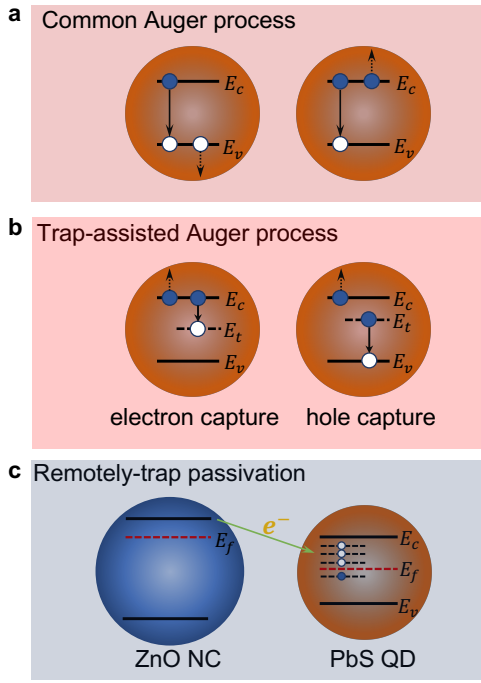

Figure 3.1: Concept of suppressing trap-assisted Auger process. (a) Band-to-band Auger recombination, where the recombination and nonradiative energy transfer occurring for band-edge carriers. (b) trap-assisted Auger mechanism, where the mid-gap trap state captures an electron (hole), and the released energy transferred to the CB electron. (c) The empty traps (electron acceptor sites) in PbS QD are filled with the electrons of n-type ZnO NC, leading to the reduction of the trap states density. Reprinted by permission from Wiley [28], Copyright 2022. Wiley-VCH Verlag GmbH & Co. KGaA. Weinheim.

To validate our hypothesis about trap-state passivation, we conducted thermal admittance spectroscopy (TAS). TAS enables us to characterize the energy and the density of trap states in photosensitive materials [98, 99]. The results and detailed analysis of our TAS measurements are described in Appendix B.5. The calculated density of the trap states, N_T versus the position of the trap states, E_T, in the band gap of CQDs is shown in Figure 3.2. There is a clear signature of the trap-state reduction using CQDs/NCs blending, where E_T is decreased from 0.101 eV in the bare PbS CQD device to 0.046 eV in the PbS/ZnO blend. Consequently, the overall trap-state density dropped by an order of magnitude, from 1.35×10^{17} in bare-PbS CQD device to 2.36×10^{16} in PbS/ZnO binary blend with 30% ZnO content. Therefore, with the reduction in the trap-state density by one order of magnitude, the probability of electron capturing should be significantly reduced in PbS-emitter CQDs which play a central role in trap-assisted Auger recombination.

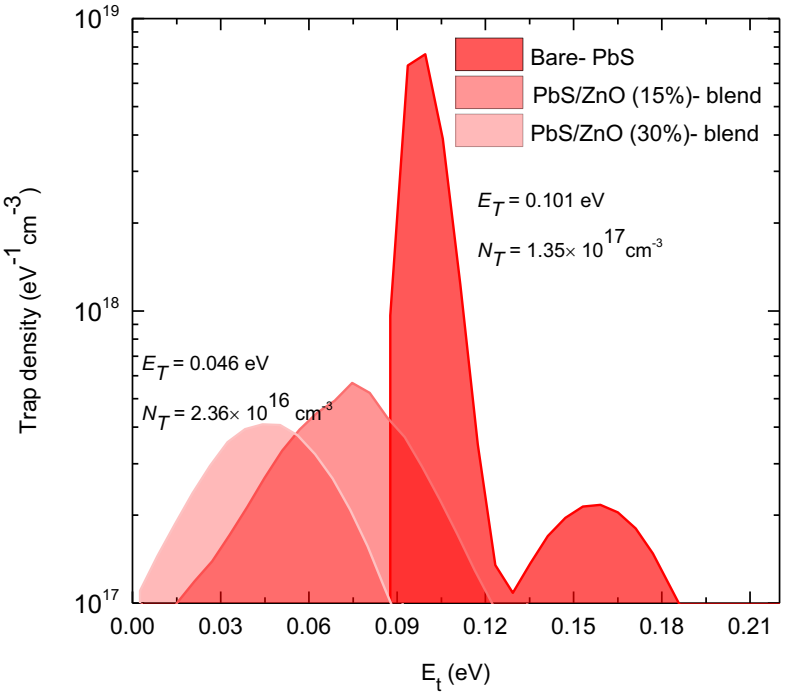

Figure 3.2: Calculated density of in-gap trap states N_T plot as a function of E_T for bare-PbS and PbS/ZnO-blebnd devices varying ZnO loading. By increasing the ZnO content in the binary devices, the trap states reduced along with decreasing the of the trap energy Reprinted by permission from Wiley [28], Copyright 2022. Wiley-VCH Verlag GmbH & Co. KGaA. Weinheim

3.2.1 Excitonic kinetics

Here, we investigated the effect of remote passivation of the trap states in our proposed binary nanocomposite on the excitonic effect. To do so, we employed two different spectroscopy methods including time-resolved PL spectroscopy (TRPL) and transient absorption spectroscopy (TA). The first was utilized to understand single-exciton dynamics (low carrier density regime,$\langle N \rangle \ll 1$), and the second for multiexciton kinetics (high injection level,$\langle N \rangle > 1$). Figure 3.3 depicts the TRPL measurements of bare-PbS and PbS/ZnO blend films, in which the fitting lifetime components are clearly elongated as parameters are provided in Table 3.1. The prolongation of the lifetime can be explained by the successful remote passivation of the trap-states in PbS-emitter CQDs. Consequently, photoluminescence-quantum yield (PL-QY) is extremely enhanced in blend device, for which PL-QY is reached $\approx 30-35\%$ in the PbS/ZnO binary films, while $< 3\%$ for the bare PbS CQDs devices. Moreover, to better understand the single-exciton kinetics, we considered the contribution factor of each fitting component

(columns 6 & 7 in Table 3.1). Therefore, it can be concluded that the τ_1 component in both samples translates the lifetime of the nonradiative recombination channel which induced by trap-states since the contribution of this channel is reduced (from 89% to 69%) by passivating the trap-states.

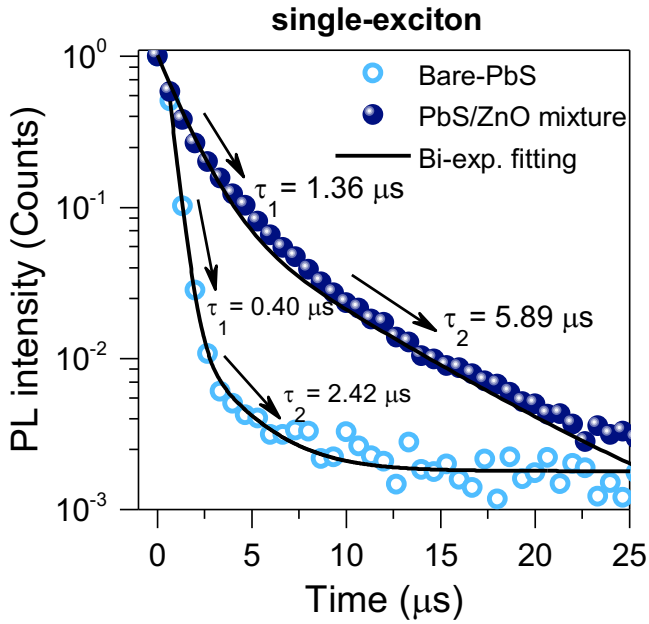

Figure 3.3: Single-exciton dynamics of bare-PbS and PbS/ZnO binary blend samples having 30 % ZnO loading. Reprinted with permission from Wiley [28], Copyright 2022. Wiley-VCH Verlag GmbH & Co.

Table 3.1: Fitting parameters of PL decay curve for bare-PbS QDs and PbS/ZnO having 30 % ZnO loading samples

Sample	A_1	τ_1 (μs)	A_2	τ_2 (μs)	$\frac{A_1\tau_1}{A_1\tau_1+A_2\tau_2}$ (%)	$\frac{A_2\tau_2}{A_1\tau_1+A_2\tau_2}$ (%)	$\tau_{ave} = \frac{\Sigma A_i\tau_i}{\Sigma A_i}$ (μs)
Bare-PbS	0.51	0.40	0.01	2.42	89	11	0.42
PbS/ZnO	1.19	1.36	0.12	5.89	69	31	1.77

Besides, τ_2 should indicate the lifetime of the radiative recombination channel, since the contribution is enhanced (from 11%-31%) in the binary blend samples. The measured PL-QY is in good agreement with the contribution factor of the radiative- and nonradiative- channels.

Then, we performed TA to extract the multiexciton kinetics of our proposed binary blend. The multiexciton dynamics of the samples were extracted using the simple subtractive method explained by Klimov et al [77]. We used the following equation to

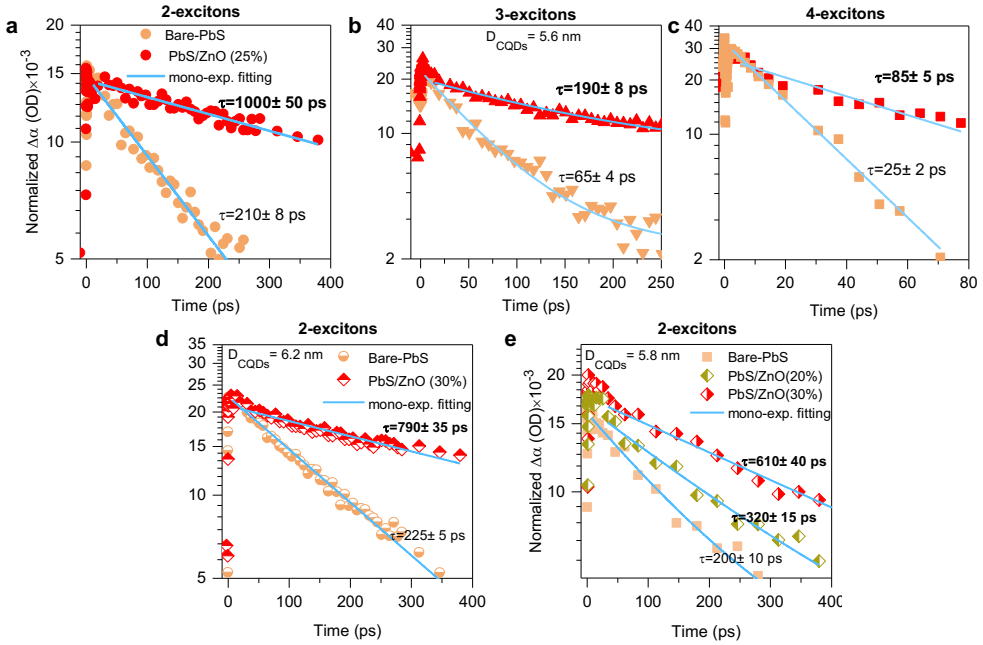

Figure 3.4: Multiexciton dynamics of bare-PbS and binary blend of PbS/ZnO. (a) Kinetics of 2-excitons, 3-excitons (b) and 4-excitons (c) for $D_{CQDs} = 5.6$ nm, where ZnO content is 25% in PbS/ZnO blend sample. (d), (e) Dynamics of 2-excitons as a function of ZnO NCs content in binary blend (symbols), obtained from TA spectra of the samples at the band-edge exciton absorption ($1S_e - 1S_h$ transition). $D_{CQDs} = 5.8$ nm (d) and $D_{CQDs} = 5.8$ nm (e). D_{CQDs} denotes the diameter of PbS-emitter CQDs. The blue solid lines represent the corresponding the mono-exponential fitting (lifetime component τ) which extracted from TA measurements based on the method described in , Reprinted with permission from Wiley [28], Copyright 2022. Wiley-VCH Verlag GmbH & Co. KGaA. Weinheim.

calculate the generated average number of excitons per-dot in our samples:

$$\langle N \rangle = \frac{E_i(I_0 - I_t - I_r)}{ATF} V \tag{3.1}$$

here, E_i denotes as the generated number of excitons at the excitation wavelength (800 nm). I_0, I_t, I_r are the intensities of the incident, transmitted and reflected of the pump beam, which were monitored during the experiment. A is the excitation area, T is the thickness of the thin films (measured by SEM and profilometry) and F is the filling factor of the film (which is 0.74 for bare-PbS film, and 0.52 for PbS/ZnO blend having 30 % ZnO loading). V denotes the volume of one PbS CQD. Particularly, to extract the

bi-exciton Auger decay in bare-PbS and PbS/ZnO binary blend samples, the recorded trace at low fluence ($\langle N \rangle \ll 1$) was subtracted from the traces at $\langle N \rangle \approx 0.4$ in both cases. This procedure was also applied to extract the dynamics of CQDs states with 3- and 4- excitons. Note that at these values of $\langle N \rangle$, the excess carrier density is on the order of $\Delta n \propto 10^{19}$ where trap-assisted Auger processes are dominant [83]. As shown in Figure 3.4a-c, all the multiexciton (2-, 3- and 4-exctions) lifetimes are prolonged in PbS/ZnO binary sample having $D_{CQDs} = 5.6$ nm. Notably, the bi-exciton lifetime (Figure 3.4a) is extended up to 1000 ps in the PbS/ZnO blend, which is 5 times longer than that of bare-PbS CQDs. The obtained lifetime is the longest reported bi-exciton Auger recombination lifetime in PbS(Se)-based QDs, which give infrared optical gain. This trend is also observed for different sizes of PbS-emitter CQDs, $D_{CQDs} = 6.2$ nm (Figure 3.4d) and $D_{CQDs} = 5.8$ nm (Figure 3.4e). As illustrated in Figure 3.4e, the Auger decay can be controlled by changing the loading amount of ZnO in the binary samples, for which the biexciton lifetimes are extended by increasing the content of ZnO.

3.2.2 ASE characterizations

We carried-out ASE measurements in bare-PbS QDs and Pb/ZnO binary blend devices to investigate the effect of suppressing trap-assisted Auger processes on optical gain performance. The details of the ASE measurements can be found in Appendix B.4. As an exemplary case, ASE spectra along with its FWHM of a PbS/ZnO binary blend having 30% ZnO loading are plotted in Figure 3.5a as a function of the absorbed fluence (See Figures 3.6 & 3.7 for other sizes). At low fluences, only spontaneous emission was observed in PL spectra within an FWHM of 94 nm (Figure 3.5a). With increasing pump intensity, the ASE peak is evident at $\backsim$ 1605 nm in the emission spectra, having a narrower FWHM of $\backsim$ 14 nm. In Figure 3.5b, we plotted the integrated intensity emission as a function of the absorbed fluence at the optical pumping wavelength (1030 nm) for bare-PbS CQDs and varying ZnO loading in PbS/ZnO binary blend. By increasing the pump intensity, the integrated PL intensity increases linearly at low fluences, and then at the ASE threshold exhibits a sharp transition to a super-linear behavior (Figure 3.5b). The ASE threshold (of absorbed pump fluence) for bare-PbS CQDs is 138 $\mu J.cm^{-}2$, while for 20%, 25%, and 30% ZnO loading in PbS/ZnO binary blends is 80, 58, and 39 $\mu J.cm^{-2}$, respectively; substantially reducing the ASE threshold up to 3-fold. We attribute this substantial reduction in ASE thresholds to: Firstly, the significant suppression of Auger recombination in our binary films, which limits the ASE and lasing thresholds in CQD system [56],and secondly, to reduced self-absorption losses at ASE wavelength in binary blends due to the decreased number of PbS-emitter

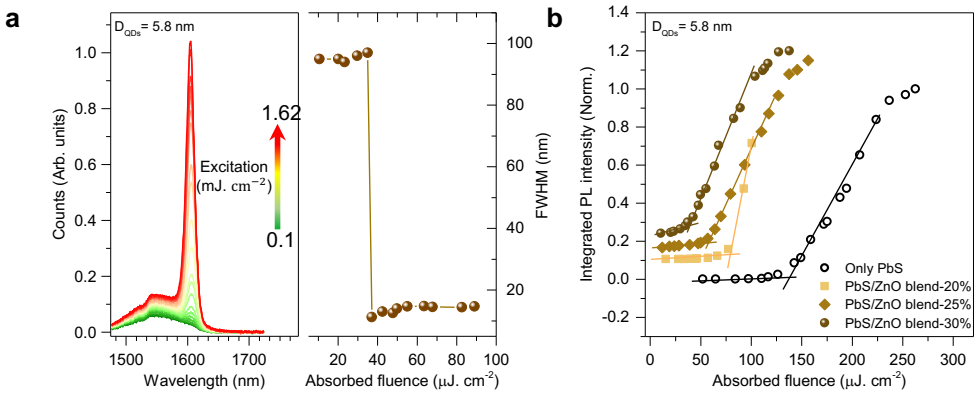

Figure 3.5: (a) Pump-dependent ASE spectra of PbS/ZnO (30% loading) binary blend samples, along with corresponding FWHM of each spectrum as function of excitation. D_{CQDs} denotes the diameter of PbS-emitter CQDs. (b) Integrated PL spectra depicted as a function of the absorbed fluence at the optical pumping wavelength (1030 nm) for bare-PbS emitter and PbS/ZnO binary blend having ZnO loading of 20 %, 25% and 30%. Reprinted with permission from Wiley [28]. Copyright 2022. Wiley-VCH Verlag GmbH Co. KGaA. Weinheim.

CQDs per unit-volume of the gain medium, which has been experimentally shown to be beneficial for reducing the ASE and lasing thresholds in other types of engineered CQDs [36, 42, 43, 45]. Here, we reduced the self-absorption losses by replacing the gain material (i.e., PbS-emitter QD) with a non-absorbing material (i.e., ZnO NC) which is more robust method compared to the methods previously reported.

In addition, varying the ZnO loading in binary blend led us to achieve fine-tuneable gain spectrum across the optical telecommunication band as depicted in Figure 3.8a, with resolution beyond what quantum size effect can achieve. Here, by increasing ZnO content in blend samples, the ASE spectra is gradually blue-shifted in the examined three different sizes of PbS-emitter CQDs. For instance, in 5.6 nm CQDs, the ASE spectra of PbS/ZnO blend samples having 15%, 20% and 25% ZnO loading is correspondingly blue-shifted by 17, 24, 30 nm with respect to their bare-PbS counterpart (light-orange coloured spectra in Figure 3.8a, A similar blue-shift is observed in the absorption spectra (Figure 3.9). We ascribe the blue-shifting of ASE and absorption spectra due to increasing inter-dot spacing of PbS-emitter CQDs [100, 101]. Figure 3.8b provides a summary of the measured ASE in different sizes of PbS-emitter cQDs as a function of ZnO content. As shown in Figure 3.8b, in all sizes of CQDs, the ASE thresholds are clearly reduced by increasing the amount of ZnO loading in binary blend. For instance, the pump fluence ASE threshold for bare-PbS CQDs having a diameter size of 5.8 nm is $\backsim 1060 \mu J.cm^{-2}$, which drops to $\backsim 430 \mu J.cm^{-2}$ in the binary blend

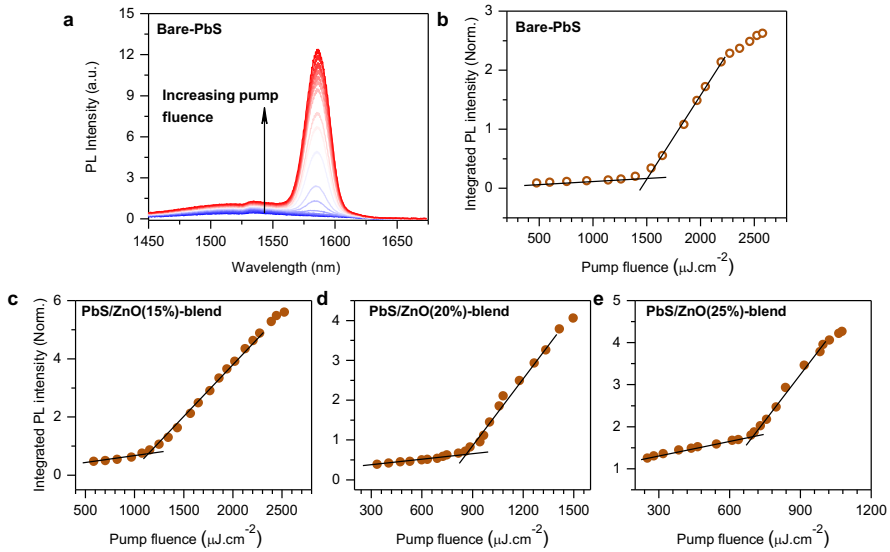

Figure 3.6: (a) Pump-dependent ASE spectra of bare-PbS CQDs having dimeter of 5.6 nm. (b) Integrated PL in intensity plotted against pump fluence for bare-PbS QDs sample. (c)-(e), Integrated PL intensity of ASE spectra versus pump fluence in PbS/ZnO binary blend having ZnO loading of 15% (c), 20% (d) and 25% (e). Reprinted with permission from Wiley [28], Copyright 2022. Wiley-VCH Verlag GmbH & Co. KGaA. Weinheim.

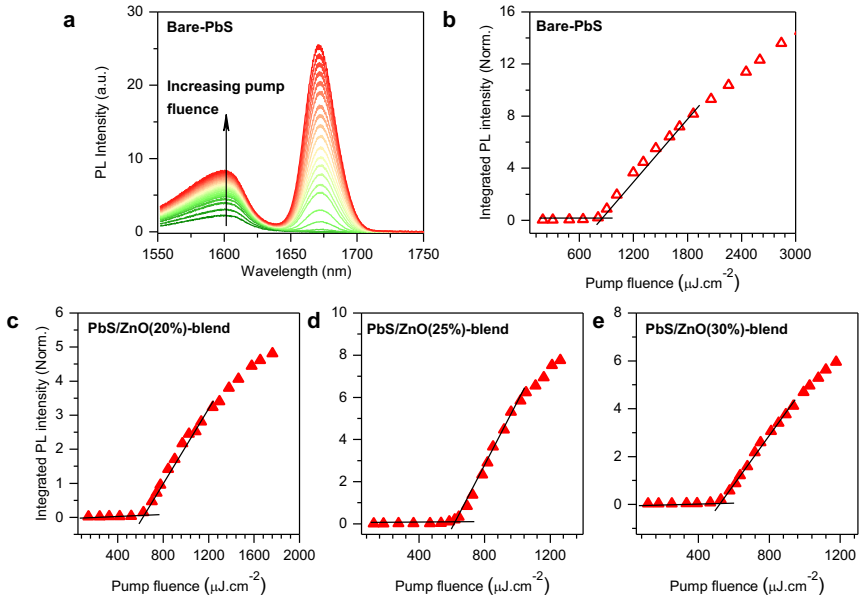

Figure 3.7: (a) Pump-dependent ASE spectra of bare-PbS QDs having dimeter of 5.8 nm. (b) Integrated PL in intensity plotted against pump fluence for bare-PbS QDs sample. (c)-(e), Integrated PL intensity of ASE spectra versus pump fluence in PbS/ZnO binary blend having ZnO loading of 20% (c), 25% (d) and 30% (e). Reprinted with permission from Wiley [28], Copyright 2022. Wiley-VCH Verlag GmbH & Co. KGaA. Weinheim

sample with 30% ZnO loading.

3.2.3 Lasing performance of PbS/ZnO blend

Finally, we combined the PbS/ZnO binary blend with 30% ZnO loading (our best performing ASE sample) with a second-order DFB resonator which provides strong in-plane feedback and lasing emission normal to the surface. Figure 3.10a illustrates the schematics of the DFB laser, where the film is pumped by a stripe excitation at normal incidence while the lasing emission is emitted from the surface of the device. A cross-sectional scanning electron microscopy (SEM) image of the PbS/ZnO binary blend on top of the DFB grating is given in Figure 3.10b, along with its parameters. By increasing the pump fluence, a single-mode lasing peak emerges at $\backsim$1650 nm with a linewidth of 1.26 nm (0.62 meV) (Figure 3.10c). This is accompanied by a clearly the lasing emission intensity versus the angle of the polarizer between the device and detector. The experimental data (symbols) are well-fitted with a function of $\cos^2(\theta)$, indicating a linearly polarized lasing emission with a polarization factor of R= 0.96, R is defined as $(I_{\parallel} - I_{\perp})/(I_{\parallel} + I_{\perp})$, where $I_{\parallel}$ and $I_{\perp}$ is the emission intensity

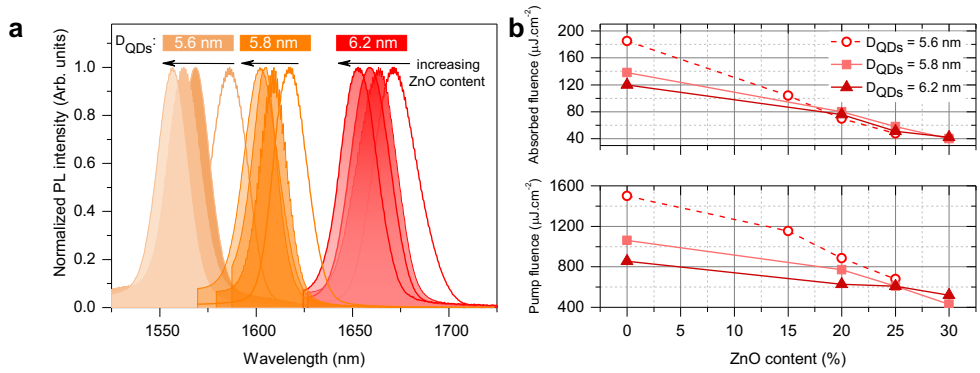

Figure 3.8: (a) Collective ASE spectra from a series of bare-PbS CQDs, and PbS/ZnO blend samples. Solid lines show the ASE spectra of bare-PbS CQDs samples, whilst the colour-filled spectra represent the ASE of binary blend samples with varying ZnO loading as shown by arrows. (b) The measured ASE thresholds as a function of ZnO content in PbS/ZnO blend sample for three different CQDs. The top panel shows the absorbed fluence ASE threshold of the films at 1030 nm (optical pumping wavelength). The bottom panel exhibits the pump fluence ASE threshold. Reprinted with permission from Wiley [28], Copyright 2022. Wiley-VCH Verlag GmbH & Co. KGaA. Weinheim.

parallel and vertical to the optical axis, respectively. This is accompanied by a clearly sharp growth in emission at a pump fluence of ≈385 $\mu J.cm^{-2}$ (corresponding to ∽46 $\mu J.cm^{-2}$ in terms of absorbed fluence) indicating lasing threshold (Figure 3.10d). The lasing emission intensity follows a S-shaped behaviour (changing the slopes in log-log scale) as a function of the pump intensity, which is a characteristic of lasing action (Figure 3.10d). This is the record lowest lasing threshold among other PbS-based CQDs infrared lasers [44]. In addition, our DFB laser devices show a lasing emission with an average FWHM of 1.45 ± 0.21 nm (0.68 ± 0.09 meV) outperforming the previously reported PbS-based DFB lasers [44]. This can be attributed to the reduction of the refractive index contrast between the gain medium (i.e., PbS/ZnO (30%) blend) and the grating (i.e., Al_2O_3), and the reduction of self-absorption in the cavity. Figure 3.10f plots further studied the lasing stability of our devices under continuous excitation of a pulsed-laser. As shown in Figure 3.10g, the lasing intensity is dropped to only 15% of the initial value after 5 hours continuous excitation at 10 kHz (corresponds to 180 millions laser shots). Notably the obtained stability in the present study is the highest lasing stability reported to date among all CQD-based lasers. We ascribe this to the significant reduction of Auger-assisted recombination, which cause heating issues in CQDs thin films leading to material degradation. The reduction in ASE and lasing thresholds owing to suppression of the trap-assisted Auger recombination in PbS/ZnO binary blend is consistently witnessed in all studied devices with an average reduction of 1.8-2.4 (see Figures 3.8b, 3.10d and 3.11).

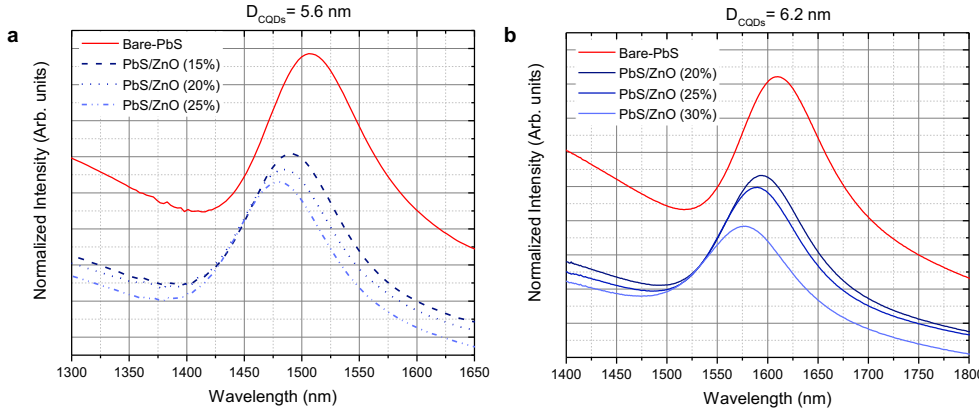

Figure 3.9: Absorption spectra of the bare-PbS and PbS/ZnO blend devices varying ZnO loading for (a) D_{CQDs} = 5.6 nm, and (b) D_{CQDs} = 6.2 nm. Reprinted with permission from Wiley [28], Copyright 2022. Wiley-VCH Verlag GmbH & Co. KGaA. Weinheim.

3.3 Summary

In summary, we demonstrated a new approach to engineer nanocrystalline solids for high performance CQD lasers. The use of an appropriate mixture of CQDs with ZnO NCs allows us to supress Auger recombination, which significantly reduces the ASE and lasing thresholds in PbS CQDs solid films. Additionally, this method led us to achieve a record stable lasing performance as well as an ultra-fine tuneable gain spectrum in near infrared spectrum. These results show that CQDs can emerge as a low-cost solution-processed and robust technology for infrared lasing application including LIDAR, biomedical imaging, and optical telecommunication.

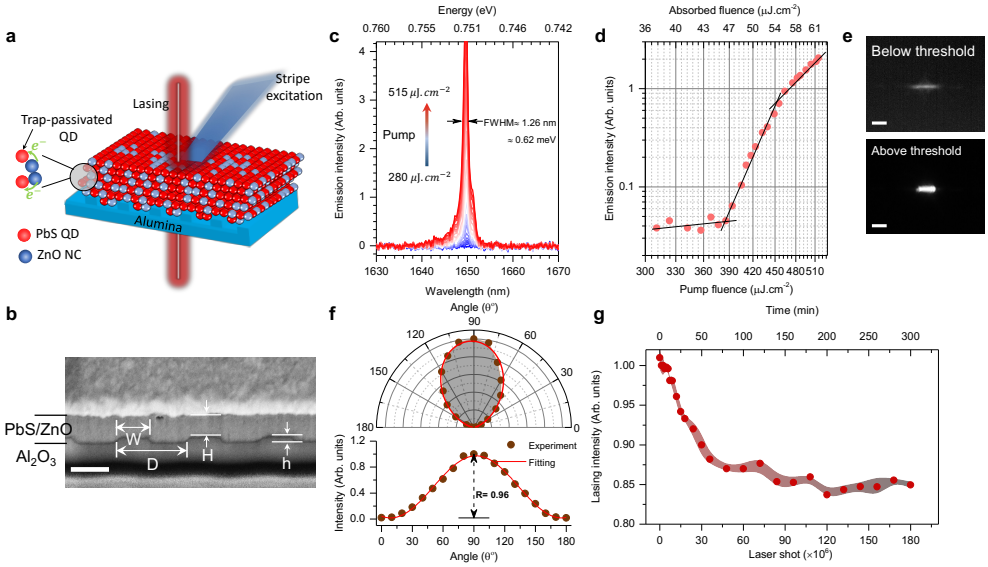

Figure 3.10: Lasing performance of a device made of Pb/ZnO binary blend integrated to a second-order grating. (a) Schematic representation of the DFB laser under optical pumping. Red and blue dots symbolized for PbS-emitter CQDs and ZnO NCs, respectively. (b) The SEM image of the PbS/ZnO blend on top of the DFB grating ("H" is the thickness of the PbS/ZnO thin film, width (W), period (D) and height (h) of the grating). The scale bar is 500 nm. (c) Emission spectra of the DFB laser are plotted as the pump fluence is progressively increased. (d) Emission intensity versus pump and absorbed fluence (at 1030 nm) of the device (symbols). The solid black lines indicating changes of the slope in log-log scale, as well as showing the lasing threshold at ∽385 $\mu J.cm^{-2}$. (e) Infrared picture of the device taken from surface of the device below and above lasing threshold as indicated taken ∽20 cm away from the DFB grating. The scale bar is 1 mm. (f) Normalized emission spectrum of DFB laser above the lasing threshold depicted against of the polarizer angle between the device and the detector. "R" denotes the polarization ratio. (g) Pump-dependent lasing intensity as a function of the pumping laser shot and corresponding time (symbols). The solid red line indicates the error bar of each symbol, stemming from fluctuation of the lasing intensity. The lasing intensity dropped by 15% after 180 million shots under continuous optical pumping at 10 kHz. Reprinted with permission from Wiley [28], Copyright 2022. Wiley-VCH Verlag GmbH & Co. KGaA. Weinheim.

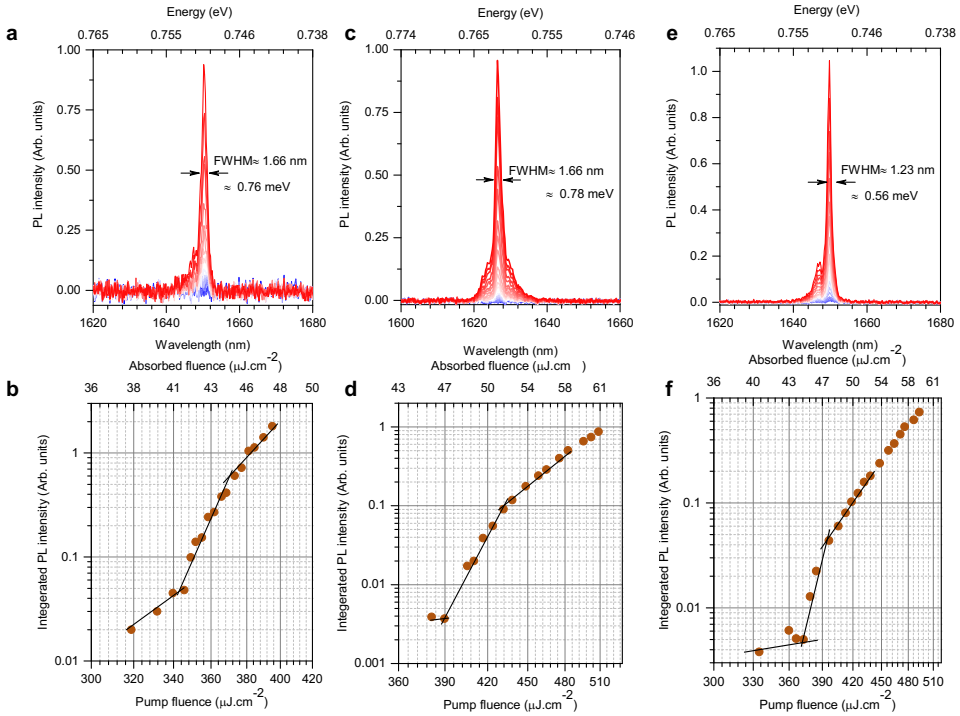

Figure 3.11: (a), (c) and (e) Pump-dependent lasing spectra of DFB devices along with corresponding integrated intensity of lasing emission against pump and absorbed fluence (b), (d) and (f), respectively. Reprinted with permission from Wiley [28], Copyright 2022. Wiley-VCH Verlag GmbH & Co. KGaA. Weinheim.

4

Sub-single-exciton infrared lasing: Doped colloidal quantum dot core/alloyed-shell heterostructures

"An expert is a man who has made all the mistakes, which can be made, in a very narrow field."

-Niels Bohr

In this chapter, we demonstrate that by properly synthesize a core/alloyed-shell heterostructured CQD comprising of PbS as core and PbSSe as shell allows to suppress band-edge Auger recombination. It further enabled us to achieve very high doping level with almost filling the first excited states of 8-fold degenerate CQDs system. By combining suppressed Auger decay in core/alloyed-shell CQDs with permanent doping for blocking the ground state absorption, we obtain sub-single-exciton gain, ASE and lasing for the first time in an infrared-emitting CQD material, bringing it on par with their visible counterparts. Additionally, utilization such a core/alloyed-thin shell heterostructure has drastically improved gain coefficient of the media and bring it on par with gain coefficients of commercial epitaxial grown III-V infrared semiconductors.

This chapter is based on the publication "Colloidal Quantum Dot Infrared Lasers fea-

turing Sub-single-exciton Threshold and Very High Gain," N. Taghipour, M. Dalmases, G. L. Withworth, Miguel Dosil, A. Othonos, Shanti Maria Liga, S. Chistodoulou, and G. Konstantatos. Advanced Materials, 35, 2207678 (2023). Adapted or Reproduced with permission from John Wiley and Sons. Copyright 2023. Wiley-VCH Verlag GmbH & Co. KGaA. Weinheim.

4.1 Motivation

The potential of broad range spectral tuneability, low-cost, solution-processability, and compatibility with any arbitrary substrates has led to tremendous progress toward successful realization of lasing action ranging from the visible to the infrared part employing CQDs as the active medium [28, 34–37, 43–45, 55, 71, 87, 102, 103]. Then, the possibility for stable- and low-threshold operating lasing would open a new realm in the lasing technologies which are not achievable with epitaxial grown semiconductor technology. In particular, the demonstration of solution-processed lasers in the eye-safe window between 1.5-1.6 μm operating robustly at room temperature and with low threshold is a prerequisite to enable applications including PICs, 3D imaging, medical diagnostics and optical theranostics.

Up to date, low threshold CQD-lasers have been reported for the materials which emit in the visible spectrum, with limited application capability. The gain medium for visible CQD-lasers have been based on CdSe/CdS core/shell NCs which offer two-fold degeneracy in the bad-edge state reaching low-pump lasing thresholds [34–36, 41, 43, 55, 62–65, 69, 87, 104–106]. Another approach for reducing the lasing threshold in the visible is obtained through populating of the CQDs' CB with permanent electrons, thus partially/totally bleaching the ground state absorption [37, 42]. Using charged CQDs has also been shown to prolong the gain lifetime since the Auger process of a charged exciton is reduced compared to that of multiexcitons in a neutral CQD [37].

On other hand, low threshold infrared lasing based on CQDs (PbX, X= Se, S) has been remained a challenge due to high degeneracy of the first excited state (8-fold). These lasers require high pumping intensities (800-2000 $\mu J.cm^{-2}$) for reaching gain/lasing as well as suffer from very fast Auger recombination ($\backsim$200 ps), gain lifetime ($<$ 30 ps) and low gain coefficients ($\backsim$ 120 cm^{-1}) [29, 44]. Specifically, the lasing thresholds in the infrared CQD-lasers are orders of magnitude higher than those in the visible engineered-CQDs. Moreover, the optical gain and Auger decay lifetime are much longer in the visible CQD-lasers compared to their infrared counterparts. Therefore, exploiting similar strategies should lead one to achieve highly performed infrared CQD-lasers to reach a viable stage for practical applications.

4.2 Results and discussion

In this part of thesis, we employ PbS/PbSSe core/alloyed-shell (C/A-S) CQDs as the infrared gain media that results in highly suppressed Auger recombination showing a lifetime of 485 ps, lowering the amplified spontaneous emission (ASE) threshold down to 300 $\mu J.cm^{-2}$, and exhibiting a record high net modal gain coefficient of 2180 cm^{-1}. By doping these engineered core/shell CQDs up to nearly filling the first excited state, we demonstrate a significant reduction of optical gain threshold, measured by TA, to an average–exciton population per dot $\langle N^{th} \rangle_g$ of 0.45 due to bleaching of the ground state absorption. This in turn have led us to attain a 5-fold reduction in ASE threshold at $\langle N^{th} \rangle_{ASE} = 0.70$ excitons per dot (corresponds to 90 $\mu J.cm^{-2}$), associated with a gain lifetime of 280 ps.

4.2.1 Core/alloyed-shell CQD band structure

To do so, we synthesized PbS/PbSSe C/A-S CQDs by the hot-injection method, with PbS core size of $\backsim$ 4.85 nm and a subsequent thin alloyed-shell ($\backsim$ 1.10 nm) of PbSSe grown around. We illustrate the schematic of the core/shell structure in Figure 4.1a, in which the band alignment indicates that our C/A-S CQD shows a quasi-type-II structure (Figure 4.1b) [107]. Figure 4.1c exhibits absorption spectra for core and core/shell CQDs. Because of the relaxation of quantum confinement, the excitonic peak of the CQDs is shifted to lower energies by growing the outer shell [36,42,67,107,108]. We show TEM images of our CQDs in Figure 4.2, where the top panel (Figure 4.2a) exhibits high-angle annular dark-field scanning transmission electron microscopy (HAADF-STEM) and bottom panel shows annular bright field STEM images (Figure 4.2b). TEM images show well-defined crystalline particles and STEM-EDS elemental mapping images (Figure 4.2c) corroborate the formation of alloyed-shell. The size distribution of TEM images for PbS-core and PbS/PbSSe C/A-S CQDs are depicted in Figure 4.3a and b, respectively. We employed X-ray powder diffraction (XRD) technique to conduct the structural characterization of the CQDs. As can be seen in Figure 4.4, PbS core and PbS/PbSSe core-alloyed shell show a halide structure. The reflections at 25°, 29.9° and 43° in PbS core correspond to (111), (200) and (220) planes, respectively. As expected, the growth of a PbSSe alloyed shell shifts the reflections to the lower angles, positioning them in between PbS and PbSe standard diffraction peaks [109–111].

Exploring the architecture of core/alloyed-shell CQDs

To shed light on the actual structure of our CQDs, we employed X-ray photoelectron spectroscopy (XPS) which allows us to extract the elemental composition of our CQDs.

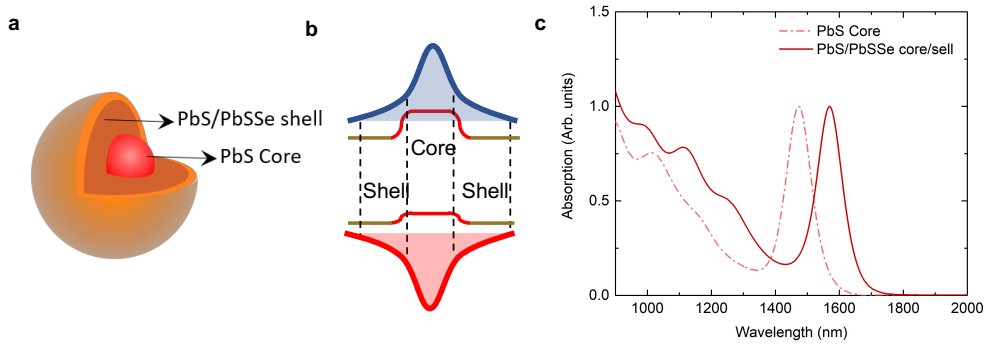

Figure 4.1: Structural characterization of PbS/PbSSe core/alloyed-shell (C/A-S) CQDs structure. (a) Schematic representation of core/shell architecture. (b) Band alignment of core/shell structure which shows quasi-type-II band alignment. (c) Absorption spectra of PbS core and PbS/PbSSe C/A-S CQDs. Reprinted with permission from Wiley [48], Copyright 2022. Wiley-VCH Verlag GmbH & Co. KGaA. Weinheim.

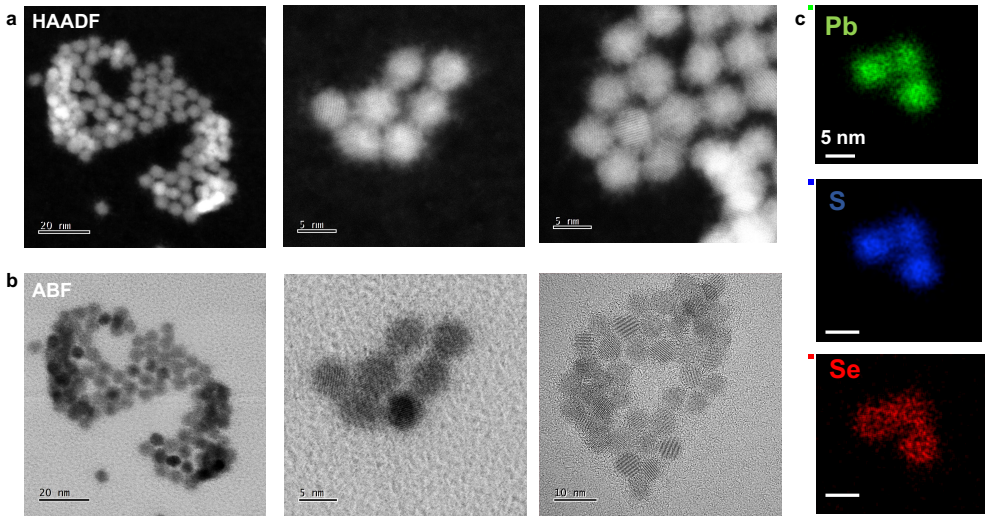

Figure 4.2: TEM images of PbS/PbSSe core/alloyed-shell QDs. a, HAADF STEM image. b, High resolution TEM images. c, Energy dispersive X-ray spectroscopy (EDS) elemental maps of C/A-S CQDs. Reprinted with permission from Wiley [48], Copyright 2022. W iley-VCH Verlag GmbH & Co. KGaA. Weinheim.

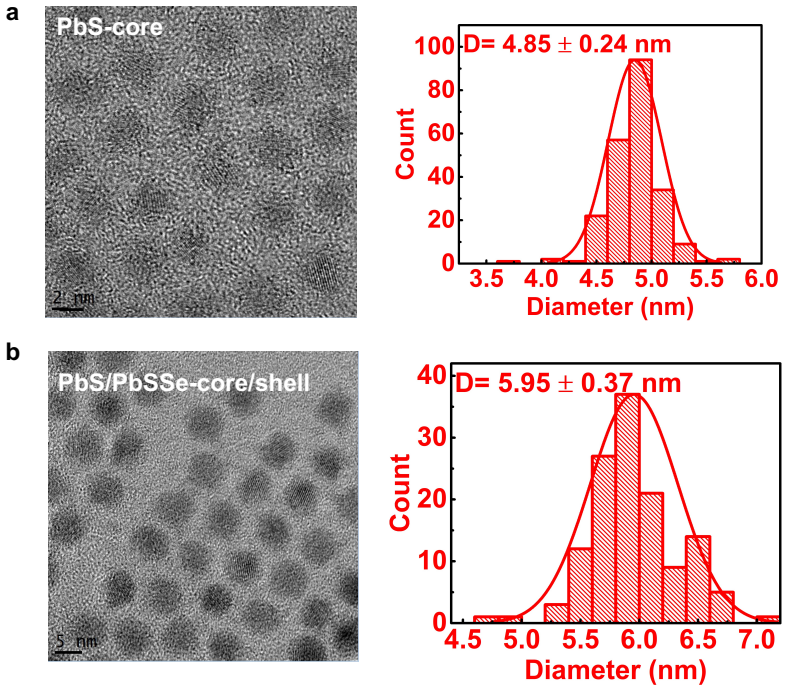

Figure 4.3: TEM images of PbS core (a) and PbS/PbSSe core/alloyed-shell QDs (b) along with their size distribution. Reprinted with permission from Wiley [48], Copyright 2022. W iley-VCH Verlag GmbH & Co. KGaA. Weinheim.

From the XPS analysis, the intensity ratio of Se(3d)/S(2s) is calculated to be 0.55 ± 0.09. Note, the XPS measurement results and analysis are shown in Figure 4.5 and Table 4.1. Besides, it has been previously shown that XPS can be employed to accurately calculate the thickness of the layers in core/shell architecture [34, 112–114]. To do so, we use the method that is previously described in [34] with slight modifications. Then, the infinitesimal intensity (dI) emitted from an infinitesimal volume (dV) is defined as:

$$dI = I_0 exp(-\frac{z}{\lambda_T})dV \tag{4.1}$$

here, z is the distance between the surface of the sample and the position of the emitted photoelectron signal, λ_T is the kinetic energy-dependent mean free path of the given material, and I_0 is defined as a constant, depending on the material properties and instrumental correction factors. In our XPS measurements, the instrumental factors are same for core and shell part of the CQDs, then the ratio between PbS and PbSe

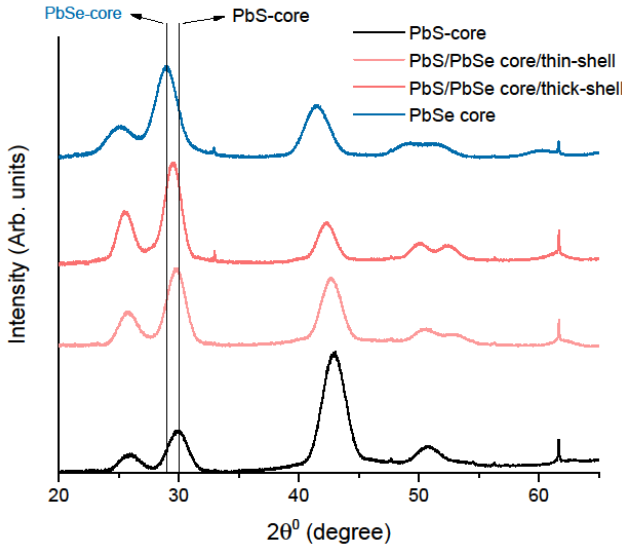

Figure 4.4: X-ray powder diffraction (XRD) characterization. Reprinted with permission from Wiley [48], Copyright 2022. Wiley-VCH Verlag GmbH & Co. KGaA. Weinheim.

can be expressed as:

$$\frac{I_0^{PbSe}}{I_0^{PbS}} = \frac{\rho^{PbSe}}{M^{PbSe}} \frac{M^{PbS}}{\rho^{PbS}} \tag{4.2}$$

where ρ and M are the density and the molecular weight of the corresponding material. For our purposes, these values have been set as: $\rho^{PbSe} = 8.1 g/cm^3, \rho^{PbS} = 7.6 g/cm^3, M^{PbSe} = 286.16 g/mol, M^{PbS} = 239.30 g/mol$. Therefore, the measured intensity of the emitted photoelectrons from the core or shell part of the CQD can be quantified from the following expression:

$$I = I_0 \int_0^R \int_0^\pi \int_0^{2\pi} exp(-\frac{f(r,\theta)}{\lambda_T}) r^2 sin(\theta)\, d\phi d\theta dr \tag{4.3}$$

here, $f(r,\theta) = \sqrt{R^2 - r^2 sin^2(\theta)} - r cos(\theta)$ is the distance between the point where the photoelectron is generated and the surface of the sample. Thus, $exp(-\frac{f(r,\theta)}{\lambda_T})$ represents the probability of the detecting a photoelectron originated at an arbitrary position inside the CQD at a certain kinetic energy. By assuming that there is no alloy region

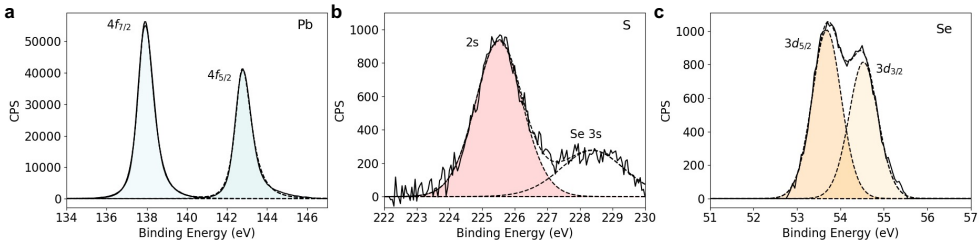

Figure 4.5: High resolution XPS spectra of PbS/PbSSe core/alloyed-shell QDs at different binding energies indicating the Pb 4f (a), S 2s (b) and Se 3d (c) peaks. Reprinted with permission from Wiley , Copyright 2022. Wiley-VCH Verlag GmbH & Co. KGaA. Weinheim.

Table 4.1: The results of the XPS signal analysis. R.S.F is the relative sensitivity factor

Name	Position	FWHM	R.S.F	Area
Pb 4f	137.92	0.88	22.70	55911.60
Pb 4f	142.77	0.88	22.70	43344.10
S 2s	225.52	1.70	1.43	1547.10
Se 3d	53.68	0.80	2.29	753.00
Se 3d	54.53	0.80	2.29	610.50

and the interface between the core and the shell is abrupt (see Figure 4.6a), the ratio of the emitted photoelectron from the shell (PbSe) to the core (PbS) can be calculated:

$$\frac{I_{shell}}{I_{core}} = \frac{I_0^{PbSe}}{I_0^{PbS}} \frac{\int_{R_c}^{R_t} \int_0^{\pi} exp(-\frac{f(r,\theta)}{\lambda_{T,Se}}) r^2 sin(\theta)\, d\theta dr}{\int_0^{R_c} \int_0^{\pi} exp(-\frac{f(r,\theta)}{\lambda_{T,S}}) r^2 sin(\theta)\, d\theta dr} \tag{4.4}$$

here, R_c and R_t is the radius of the core and total radius of the CQD, respectively. From TEM images, the R_c is calculated to be 2.45 nm and the R_t is found to be 3 nm. By considering the kinetic energy (T) of the emitted photoelectron as $T = E - BE$. Here, E is the energy of the radiation and BE is the binding energy of the analyzed XPS peak (2s for sulfur and 3d for selenium). Since we employed Al K-alpha radiation, the mean free paths for PbS and PbSe are 2.66 and 2.54 nm, respectively [115]. Using these parameters in Equation 4.4, we found the intensity ratio of Se(3d)/S(2s) as

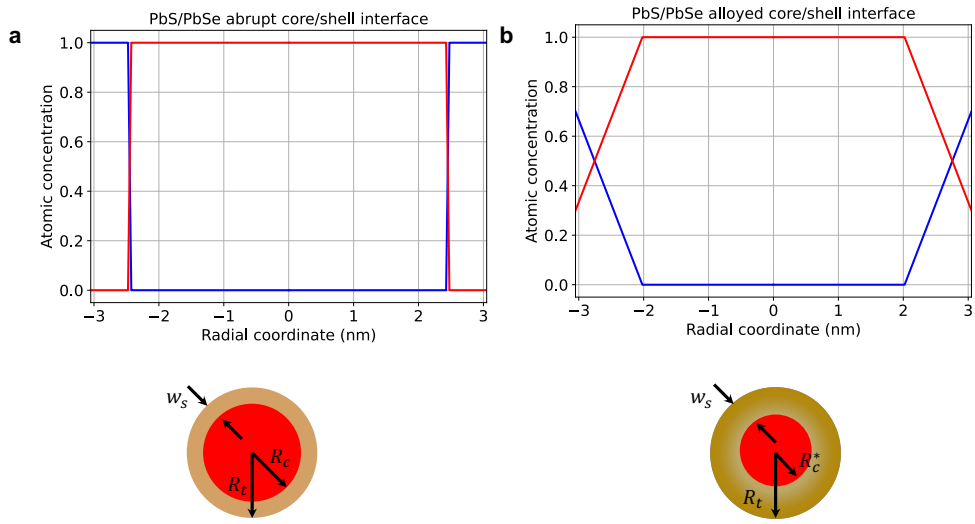

Figure 4.6: Band diagram of abrupt core/shell interface of PbS/PbSe (a) and core/gradient alloyed-shell PbS/PbSSe CQD (b). Note, the bottom panel shows the schematic representations of the corresponding CQD. Reprinted with permission from Wiley [48], Copyright 2022. Wiley-VCH Verlag GmbH & Co. KGaA. Weinheim.

1.12 for abrupt interface between the core and shell which is not consistent with our experimental observation from XPS where the measured value is 0.55. This discrepancy shows us that our shell should be formed as PbSSe gradient alloy rather than being as pure PbSe. This is originated from the diffusion of the Se to the core and S to the shell region, should result in lower Se/S ratio. Thus, we consider a gradient alloyed shell of $PbSe_xS_{1-x}$, where the atomic percentage of the Se linearly increases as a function of the radius. The final composition is set to be $PbSe_{0.7}S_{0.3}$, where final value for x is chosen based on XPS analysis. In new core/alloyed-shell model, the width of the shell region is defined as w_s (see Figure 4.6b), then the intensity ratio of Se/S is expressed as:

$$\frac{I_{shell}}{I_{core}} = \frac{I_0^{PbSe}}{I_0^{PbS}} \frac{\int_{R_c^*}^{R_t} \int_0^{\pi} X(r) exp(-\frac{f(r,\theta)}{\lambda_{T,Se}}) r^2 sin(\theta)\, d\theta dr}{\int_0^{R_c^*} \int_0^{\pi} (1 - X(r)) exp(-\frac{f(r,\theta)}{\lambda_{T,S}}) r^2 sin(\theta)\, d\theta dr} \tag{4.5}$$

where $X(r)$ and $1 - X(r)$ are the radial atomic percentages of Se and S, respectively

that defined as:

$$X(r) = \begin{cases} 0 & \text{if r}< R_c^* \\ \frac{0.7}{R_t - R_c^*}(r - R_c^*) & \text{if r}> R_c^* \end{cases} \tag{4.6}$$

here, R_c^* is defined as the actual radius of core by considering the diffusion of Se to the core. By inserting $X(r)$ in Equation 4.5, where Se/S ratio is 0.55, the thickness of alloyed-shell in our CQDs is found to be $w_s \approx 1 \pm 0.3$ nm, and the $R_c^* = 2 \pm 0.3$ nm (Figure 4.6). This observation indicates that the composition of our CQDs is PbS/PbSSe.

Calculation of radial wavefunction distribution in PbS/PbSSe core/alloyed-shell CQDs

Next, we calculated the radial distribution of the electron and hole wavefunctions using the effective mass approximation:

$$\begin{aligned} \Bigg[&- \frac{\hbar}{2}\nabla_e\left(\frac{1}{m_e^*(r)}\nabla_e\right) + U_e(r) - \frac{\hbar}{2}\nabla_h\left(\frac{1}{m_h^*(r)}\nabla_h\right) + U_h(r) \\ &- \frac{e^2}{k\left|\vec{r}_e - \vec{r}_h\right|}\Bigg] \phi_{nlm}^{exc}(\vec{r}_e, \vec{r}_h) = \epsilon_{nlm} phi_{nlm}^{exc.}(\vec{r}_e, \vec{r}_h) \end{aligned} \tag{4.7}$$

where $\hbar$ is reduced Planck constant $m_{e(h)}^*(r)$ and $U_{e(h)}(r)$ are the position-dependent effective mass and the confinement potential seen by the electron (hole), respectively, ε_{nlm} is the exciton energy eigenvalue, and $\psi_{nlm}^{exc}(\vec{r}_e, \vec{r}_h)$ is the wavefunction of the exciton. Then, the wavefunctions for both 1s electron and hole were obtained by solving their corresponding Schrödinger equation inside the CQD employing Hartree-Fock approach. Given the small electron and hole effective masses and the large value of the dielectric constant, electrostatic interaction in these materials leads to a very small correction in energy. Hence, we have omitted the Coulombic interaction term in our subsequent calculations. Under these assumptions, simplified Equation 4.7 [116,117]:

$$\left[-\frac{\hbar}{2}\nabla_{eh}\left(\frac{1}{m_{eh}^*(r)}\nabla_{eh}\right) + U_{e(h)}(r)\right] R_{e(h)}(r) = \epsilon_{e(h)} R_{e(h)} \tag{4.8}$$

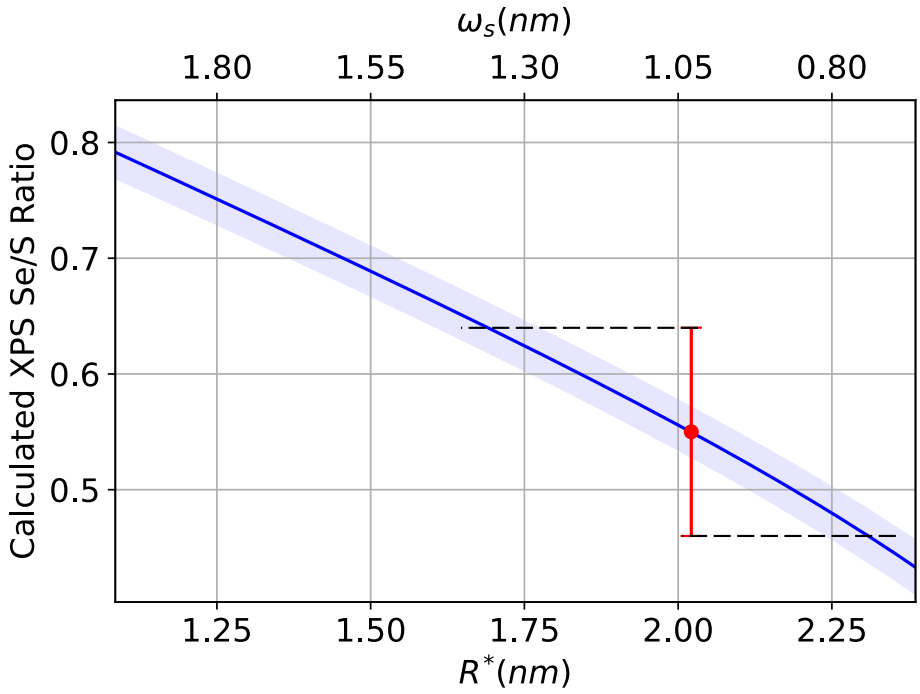

Figure 4.7: Calculated XPS Se/S as a function of actual size of the core radius (blue solid line). The red circle shows the XPS experimental result while the error bars represents the standard deviation. The dashed lines are for eye guiding. Reprinted with permission from Wiley [48], Copyright 2022. Wiley-VCH Verlag GmbH & Co. KGaA. Weinheim.

where the parameters are defined as following [107]:

$$U_e = -4.6 + 0.155x \tag{4.9}$$

$$U_h = -5.01 + 0.025x \tag{4.10}$$

$$m^*_{e(h)}\,[PbSe_xS_{1-x}] = (x)m^{PbSe}_{e(h)} + (1-x)m^{PbS}_{e(h)} \tag{4.11}$$

here, x represents the alloy fraction. All energy levels are defined with respect to the vacuum level. The energy levels outside the CQD was chosen as the bulk electron affinity for both carriers [107]. Effective masses of electron and hole in PbS and PbSe are: $m^{PbS}_{e(h)} = 0.12m_0$ $(0.11m_0)$ and $m^{PbSe}_{e(h)} = 0.084m_0$ $(0.070m_0)$ [25]. The band alignment of core/gradient-alloyed shell CQD is depicted in Figure 4.8.

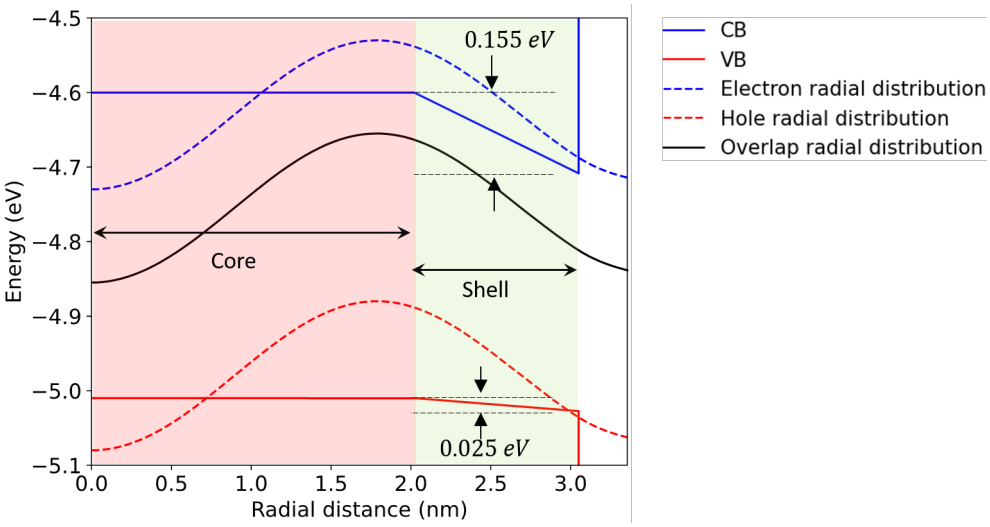

Figure 4.8: Radial density function of the first excited state electron and hole wavefunctions in core/gradient alloyed-shell CQD. The dashed lines are for eye guiding. Reprinted with permission from Wiley [48], Copyright 2022. Wiley-VCH Verlag GmbH & Co. KGaA. Weinheim.

Suppression of Auger recombination in core/alloyed-shell CQD

We plot the calculated radial density function of electron ($r^2R_e^2(r)$) and hole ($r^2R_h^2(r)$) in Figure 4.8, Here, $R_{e(h)}(r)$ is the radial component of the wavefunction of the electron and hole. As can be seen, both wavefunctions tunnel to the shell region due to the small band-offset and similar effective masses of the core and shell materials. The solid black line in Figure 4.8 shows the spatial overlap density function of the two carriers ($\rho\,(r) = r^2R_e(r)R_h(r)$). Evidently, $\rho\,(r)$ is distributed throughout the whole CQD, where the probability of recombination in the core region is $\backsim$60% of the total recombination probability (see Figure 4.8). This reduction originates from the spreading of the electron and hole wavefunctions to the shell region, resulting in suppression of Auger recombination. In particular, smoothening (alloyed) the potential confinement at the interface of the core and shell region results in strongly suppressed Auger recombination [56, 66, 118]. Efros et al. previously reported that the alloyed shell effectively smoothens the quantum potential confinement at the interface which leads to reduced non-radiative Auger process [68]. In contrast, the abrupt heterointerface between core and shell region has been reported to lead to increased rate of Auger processes [119].

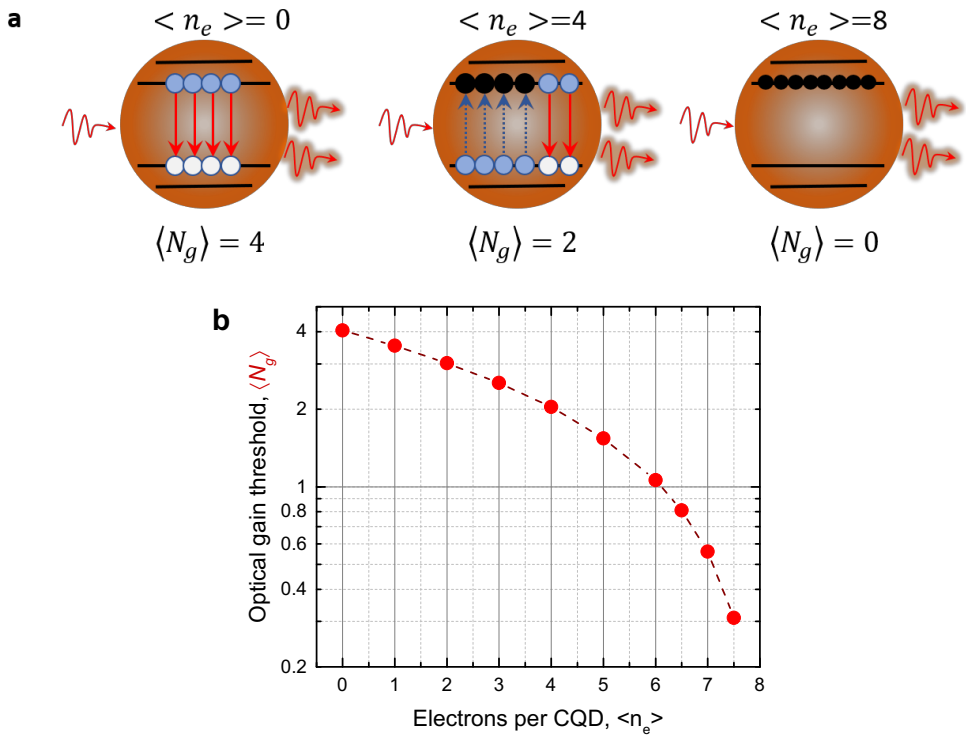

Figure 4.9: Optical gain for neutral and doped CQDs. (a) The optical gain condition for neutral, doped $\langle n_e \rangle$=4 and $\langle n_e \rangle$=8. (b) N_g, optical gain threshold versus number of electron dopants per dot $\langle n_e \rangle$. Reprinted with permission from Wiley [48], Copyright 2022. Wiley-VCH Verlag GmbH & Co. KGaA. Weinheim.

Concept of CQD charging for reducing gain threshold

The idea of CQD charging toward reducing the optical gain threshold is schematically illustrated in Figure 4.9 assuming the 8-fold degeneracy of the first excited state. In the case of neutral-charged CQD (Figure 4.9a), optical gain occurs on emission of a state having 4-exctions, since below this number of excitons stimulated emission by the electrons in the CB state is absorbed by the remained electrons in the VB state (see Figure 4.9b). By considering the short-pulse optical excitation, the photon absorption statistics follows Poisson distribution (Equation 2.14), the optical gain threshold calculated as $\langle N_g \rangle$= 4.04. In general, optical gain is realized by the difference of the fraction (percentage) of CQDs in the ensemble that provide gain, P_G and P_A the fraction of CQDs that contribute to the ground state absorption. This condition can be written as $G \propto \gamma(P_G - P_A)$, G is the gain coefficient, and γ represents the rate of absorption or stimulated emission for the allowed transition. So, the gain threshold is defined as G =0, which yields $P_G = P_A$. By assuming Poisson distribution of the

electron-hole pairs in ensembled of CQDs, the probability of a CQD having n excitons is $P(n) = e^{-\langle N \rangle}\langle N \rangle^n / n!$. Therefore, the P_G and P_A can be expressed as the following equations:

$$P_G = \sum_{n=1}^{8} p(n) \frac{(N_e + n_e)N_h}{g_e g_h} \tag{4.12}$$

$$P_A = \sum_{n=0}^{7-n_e} p(n)(1 - \frac{N_e + n_e}{g_e})(1 - \frac{N_h}{g_h}) \tag{4.13}$$

Here, $N_e = N_h = n$ and g_e, g_h is the degeneracy of electrons and holes respectively, where $g_e = g_h = 8$ in PbS-based CQDs. n_e is the number of permanent electron dopants. Then, we calculate the theoretical optical gain threshold as a function of n_e, shown in Figure 4.9b. In order to permanently dope our solid films, we carried out a ligand exchange process, using 1-ethyl-3-methylimidazolium iodide (EMII) as a ligand, in this process the S^{2-} were substituted by I^- on the (100) crystalline facet of the CQDs, as represented schematically in Figure 4.10. Subsequently, a thin layer of alumina is deposited via atomic layer deposition (ALD) to protect the treated surface of CQDs from atmospheric electron acceptors (oxygen/water) [29, 120]. This iodide ligand exchange procedure populates the CB of the CQDs with permanent electrons. Bleaching of the first excitonic feature due to Pauli blocking is a clear signature of doping the CQD films (Figure 4.11). $\langle n_e \rangle$ is defined as the averaged number of doping electrons per quantum dot in the films, calculated from the quenching of absorption in the area of the first excitonic transition. To compute $\langle n_e \rangle$ in the doped films, a baseline correction was applied to the raw absorption measurement to remove the background curve from the before and after doping process. Then, the integrated intensity of the excitonic peak in baseline corrected absorption spectra were calculated for before doping (I_1) and after doping (I_2) cases. In 8-fold degenerated PbS CQDs, the average number of electrons in the conduction band, $\langle n_e \rangle = 8(1 - I_2/I_1)$.

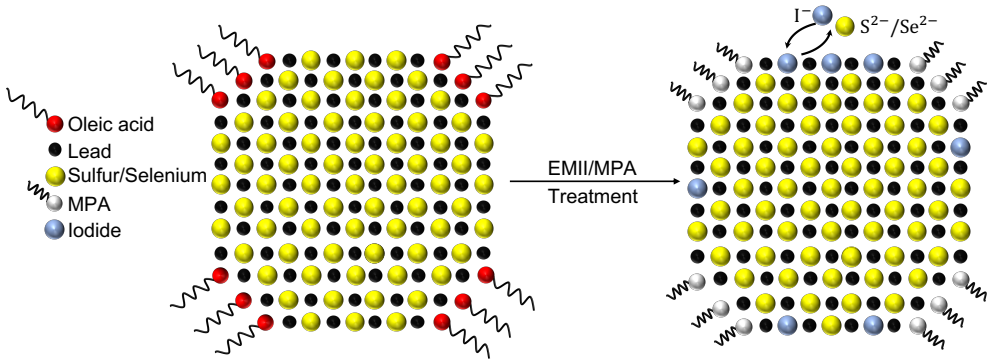

Figure 4.10: Doping mechanism. Schematic representation of before (left) and after (right) ligand exchange procedure. Reprinted with permission from Wiley [48], Copyright 2022. Wiley-VCH Verlag GmbH & Co. KGaA. Weinheim.

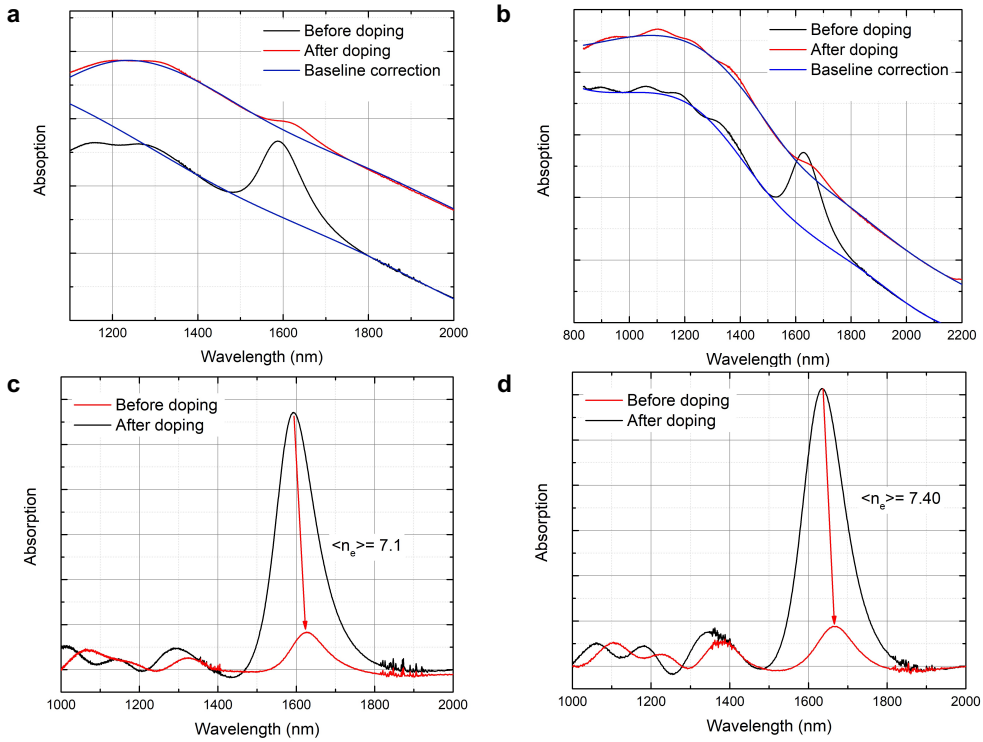

Figure 4.11: Analysis of CQDs thin film absorption as exemplary cases. The raw absorption of core/shell CQD solid film within an excitonic peak of 1592 nm (before doping) and 1628(after doping) (a), 1630 (before doping) and 1672 (after doping) (b). Note, the blue lines represent Spline interpolation the background curve. (c),(d), After subtraction of the interpolating, resulting in several Gaussian absorption peak. Note, to calculate the doping level, we use the lowest excitonic transition peak. Although, the intensity of other higher energy peaks is very sensitive to the interpolation parameter, which are not relevant to the main scope of this study. Reprinted with permission from Wiley [48], Copyright 2022. Wiley-VCH Verlag GmbH & Co. KGaA. Weinheim.

4.2.2 Observation of sub-single-exciton gain in doped C/A-S CQDs

To evaluate the optical gain performance of core and C/A-S CQDs, we carried out ultrafast TA spectroscopy on thin films. To quantify the optical gain threshold, we plot $\Delta\alpha/\alpha_0$ as a function of N at ASE wavelengths in Figure 4.12a-c. The optical gain threshold in terms of average number of excitons per dot, $\langle N_g^{th} \rangle$ is determined from the intersection of the experimental data (symbol) with horizontal line shown by $|\Delta\alpha|/\alpha_0 = 1$.

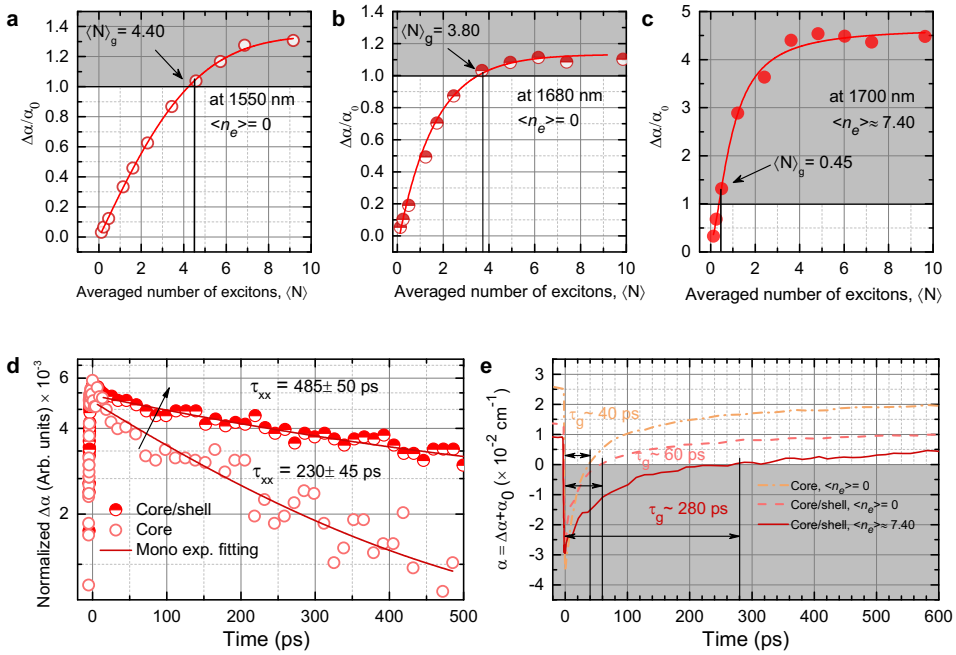

Figure 4.12: Optical gain in undoped and doped core and C/A-S CQDs. Normalized absorption bleaching as a function of N (N is the average number of excitons per dot) at the corresponding ASE peak position for (a) undoped solid film of PbS core CQDs, (b) undoped and (c) doped solid film of PbS/PbSSe C/A-S CQDs. The solid lines are for the eye guidance. The shaded region corresponds to optical gain regimes $\Delta\alpha/\alpha_0 > 1$ which implies a gain threshold of $\langle N_g \rangle = 4.40$, 3.80 and 0.45 for undoped core (a), undoped C/A-S (b) and doped C/A-S CQDs (c). (d) Dynamics of bi-excitons (symbol), obtained from TA at the corresponding ASE peak. The red solid line shows single exponential fitting to experimental data. (e) Nonlinear absorption ($\alpha = \alpha_0 + \Delta\alpha$) as a function of time delay at the ASE peak position for undoped core, undoped C/A-S and doped C/A-S CQDs, indicating net optical gain lifetime of $\tau_g \approx 40$, 60 and 280 ps, respectively. The shaded region shows optical gain ($\alpha < 0$). Reprinted with permission from Wiley [48], Copyright 2022. Wiley-VCH Verlag GmbH & Co. KGaA. Weinheim.

For the neutral-charged PbS core CQDs sample, this was measured to be $\langle N_g^{th} \rangle = 4.40$ (Figure 4.12a), which is close to theoretical value of 4.04 expected from Poisson statistics (see Figure 4.9b). For calculating average number of excitons, we employed the same method described in section 3.2.1, and using Equation 3.1. The gain threshold in neutral PbS/PbSSe C/A-S CQD sample drops to 3.80, ascribed to the suppression of Auger recombination and the reduction in self-absorption losses. As previously shown, a large shift of the stimulated emission spectrum with respect to the excitonic absorption reduces the re-absorption losses in the materials [36,42,43,121,122]. The TA characterization on heavily doped C/A-S CQDs (with $\langle n_e \rangle \approx 7.40$) shows a significant reduction of the gain threshold to $\langle N_g^{th} \rangle$ 0.45. This observation demonstrates a considerable reduction (almost 10-fold) of the optical gain threshold in heavily doped C/A-S CQDs compared to the neutral-charged core CQDs, which paves the way for sub-single-exciton infrared lasing from an 8-fold degenerate PbS-based CQD system. Another important observation in using PbS/PbSSe C/A-S CQDs as a gain medium is the prolongation of the biexciton Auger lifetime (Figure 4.12d) that is measured to be is 485 ps in C/A-S CQDs, while core CQDs shows a value of $\backsim$230 ps. In Figure 4.12e, we plot the sum of the linear absorption, α_0, and the TA dynamics, $\Delta\alpha(t)$ at the corresponding ASE wavelengths, to measure the time for which gain persists in the CQDs ($\alpha_0 + \Delta\alpha < 0$) denoted as the gain lifetime τ_g. For the heavily doped C/A-S CQDs ($\langle n_e \rangle \approx 7.40$) was measured τ_g to be $\backsim$280 ps which is remarkably longer than that of the neutral core CQDs (40 ps) and the neutral C/A-S CQDs (60 ps). Thus, the synergism of C/A-S CQDs with very strong doping successfully addresses the issues of high optical gain thresholds and very fast optical gain relaxation in the infrared-emitting CQDs.

4.2.3 ASE and gain coefficient characterizations

Next, we examined the optical gain performance of undoped and doped C/A-S CQDs by conducting ASE measurements on thin films. To do so, we excited the samples with fs-laser using stripe excitation and the emission was collected perpendicular to the excitation axis as explained in the Appendix B.4 (see Figure B.5). The collected emission as a function of the excitation fluence shows a clear transition from spontaneous emission to ASE through an abrupt change in the slope of the output intensity and the spectral narrowing (Figure 4.13a,b). We display the output intensity as a function of pump fluence in Figure 4.13a, in which the ASE thresholds for undoped-C/A-S CQDs film is measured as $\backsim$300 $\mu J.cm^{-2}$, while the ASE threshold for the similar size undoped-core sample is $\backsim$520 $\mu J.cm^{-2}$. Interestingly, by doping the C/A-S film ($\langle n_e \rangle = 7$), the ASE threshold drops by 70% to $\backsim$90 $\mu J.cm^{-2}$, which represents an improvement of almost one order of magnitude from commonly reported values

(500-800 $\mu J.cm^{-2}$) for similar emission wavelengths [28, 29, 44]. The measured ASE thresholds in terms of average number of excitons per dot, $\langle N^{th} \rangle_{ASE}$, correspond to a value of 3.80 (before doping) and 0.70 (after doping). The observation of ASE at sub-single-exciton per-dot population regime for the doped system suggests that the gain originates from charged single-excitons, for which the estimated gain threshold is 0.56 (see Figure 4.9b). It is worth mentioning that the attained ASE thresholds in our C/A-S CQDs is more than one order of magnitude lower than corresponding core CQDs ($> 1 mJ.cm^{-2}$) [44]. In general, the observed lower ASE thresholds in C/A-S compared to core-only CQDs is due to increasing absorption cross-section, suppressing of Auger recombination (see Figure 4.12d) and reducing the re-absorption losses. Particularly, spectral analysis of the ASE spectra (Figure 4.13b) suggests that the ASE peak of C/A-S CQDs is 32 meV shifted to longer wavelengths with respect to the first excitonic transition, while this value is 18 meV (Figure 4.14) for core-only CQDs with similar ASE wavelengths. Lowering the ASE threshold owing to reducing the self-absorption has been reported previously in visible emitting -CQDs [43, 121], -colloidal quantum wells [36] and organic dye [123] gain media. Another important benchmarking parameter for the laser devices is the net modal gain coefficient (g_{net}) of the gain medium, which quantifies light amplification per unit length and is of paramount importance for integrated and compact laser diodes. Recent advances in visible-emitting CQDs led to achieve g_{net} values as high as 6600 cm^{-1} for colloidal nanoplatelets [124], and 2800 cm^{-1} for core/shell CQDs [108]. However, to date infrared counterparts have reached much lower g_{net} of less than 120 cm^{-1} for PbS core CQDs [29, 44] and 2.4 cm^{-1} for HgTe CQDs [125].

We thus sought to measure the net modal gain coefficient of our C/A-S CQDs, characterized by the variable stripe length (VSL) method. The sample was excited by a stripe-shaped, where the length of stripe was controlled by an adjustable slit. Note, the details of VSL measurements are described in Appendix B.4. As an exemplary case, we display the integrated emission intensity of the ASE peak in Figure 4.13c against stripe length for the case doped C/A-S CQDs thin film. The integrated emission intensity raises exponentially as a function of the stripe length. This relation is generally expressed as $I(l) = A(e^{g_{net} l} - 1)$ [126], in which l is the stripe length, and g_{net} is the net modal gain coefficient. Using this equation, we extract g_{net} as 2180 $\pm$ 180 cm^{-1} at a fluence of 2200 $\mu J.cm^{-2}$. VSL measurements at different pump fluences are provided in Figure 4.14. Figure 4.13d shows that the net modal gain increases with pump fluences in the range of 200-750 $\mu J.cm^{-2}$, then deviates from this behavior and saturates at almost 2000 cm^{-1} for higher pump fluences. This behavior is consistent with ASE measurements (Figure 4.13a), in which the ASE signal output also saturates at high

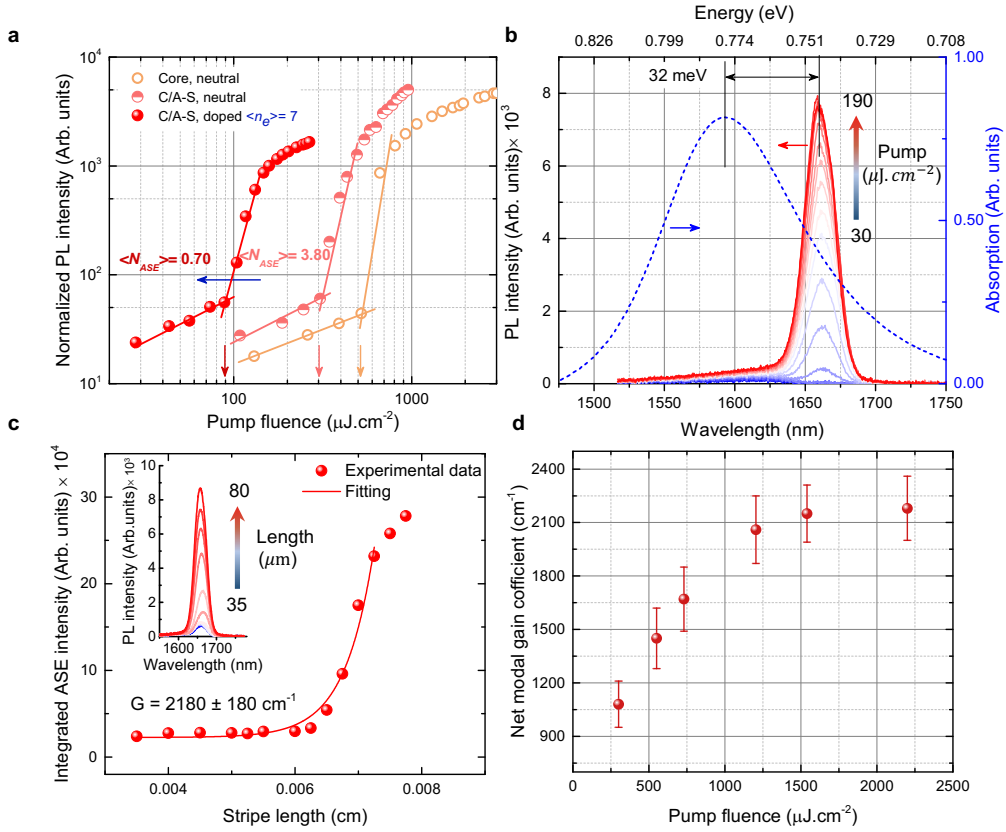

Figure 4.13: ASE and VSL characterizations of undoped- and doped -C/A-S CQDs. (a) Integrated intensity of ASE as a function of pump fluence for undoped-core, undoped-C/A-S and doped-C/A-S CQDs, with arrows indicating the ASE thresholds of ∽500, ∽300 and 90 $\mu J.cm^{-2}$, respectively. The latter corresponds to $N_{ASE} = 0.70$. (b) Spectral analysis of ASE with respect to the lowest excitonic transition of undoped C/A-S CQDs (blue dashed line). The absorption peak is isolated from full spectrum (see Figure 4.11). The ASE peak is red-shifted by 32 meV compared to the first excitonic peak. (c) Integrated intensity (ASE spectrum) of doped-C/A-S CQD thin film as a function of stripe length at a pump fluence of 2200 $\mu J.cm^{-2}$. Inset shows the PL of the sample as function of stripe length. Based on analysis of VSL measurements, the net modal gain coefficient calculated as 2180 ± 180 cm^{-1}. (d) The net modal gain coefficient obtained from VSL measurements varying the pump fluence. The maximum net modal gain is measured as 2180 cm^{-1}. Note, the error bars originated from the fitting. Reprinted with permission from Wiley [48], Copyright 2022. Wiley-VCH Verlag GmbH & Co. KGaA. Weinheim.

fluences. Our achieved g_{net} sets a record among any other solution-processed infrared gain material, and is found to be on par with epitaxially grown infrared semiconductors such as GaInAs/InP quantum dots [46]. This high gain coefficient in PbS/PbSSe C/A-S (thin shell) CQDs can be ascribed to three factors: i) PbSSe shell effectively

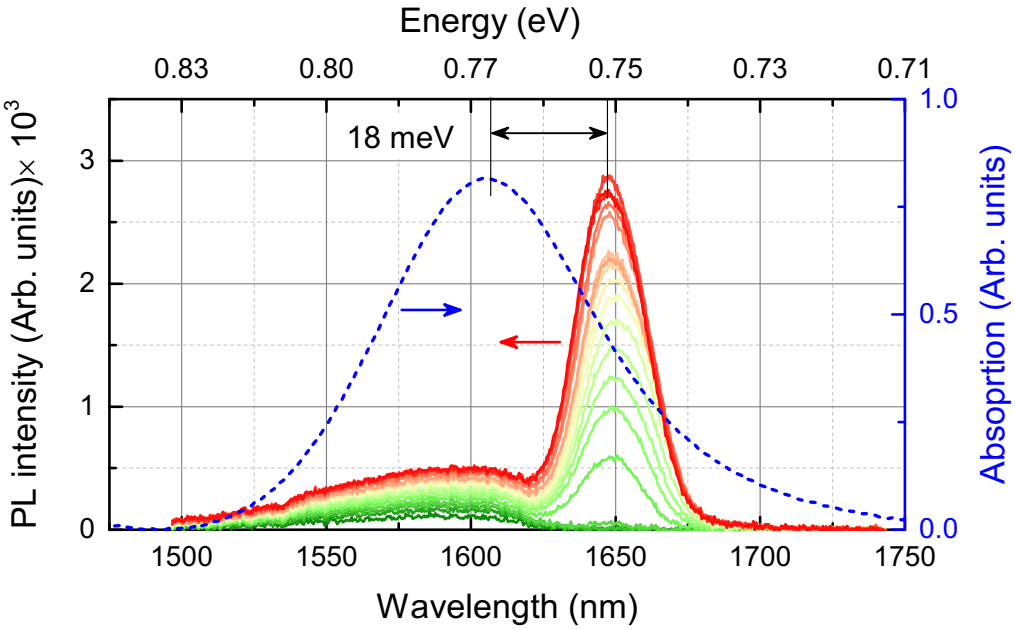

Figure 4.14: Spectral analysis of ASE compared to the lowest excitonic transition of undoped PbS core (blue dashed line). We used similar interpolation technique (explained above) to isolate the first excitonic peak transition from the background of the raw absorption spectrum. Reprinted with permission from Wiley [48], Copyright 2022. Wiley-VCH Verlag GmbH & Co. KGaA. Weinheim.

suppresses the nonradiative Auger processes, ii) A large-core/thin-shell architecture maximizes the volume fraction of the emitting PbS core over the PbSSe shell, and iii) the attractive Coulombic exciton–exciton interactions shift ASE away from the ground-state absorption (Figure 4.13b) [108].

4.2.4 Effect of CQDs doping on lasing threshold

Lastly, following the successful realization of sub-single-exciton stimulated emission using doped-C/A-S CQDs, we aimed to fabricate the first solution processed infrared laser with sub-single-exciton threshold. To do so, we deposited the CQDs on top of nanostructured gratings in order to make second-order distributed feedback (DFB) structures. The DFB grating parameters were precisely designed to provide in-plane resonance at the ASE peak, the fabrication of is given in Appendix A.3. We depict the integrated spectral output of lasing emission as a function of the excitation fluence in Figure 4.16a for undoped- and doped-CQD/DFB devices, indicating the lasing thresholds of 430 and 160 $\mu J.cm^{-2}$, respectively. To quantify the lasing thresholds in terms of N, we assumed a packing density of 74% for the CQDs thin film, and

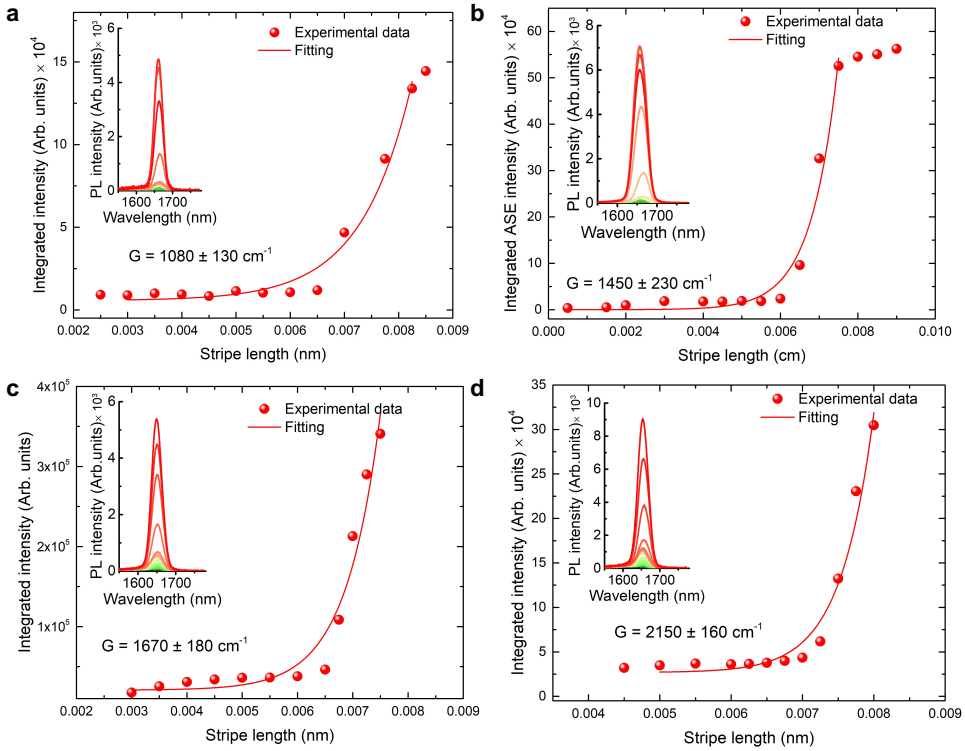

Figure 4.15: VSL measurements at different fluences. Integrated intensity against stripe length at a fluence of 300 (a), 550 (b), 730 (c) and 1540 $\mu J.cm^{-2}$ (d). Note, insets show the corresponding PL spectra as a function of stripe length. Reprinted with permission from Wiley [48], Copyright 2022. Wiley-VCH Verlag GmbH & Co. KGaA. Weinheim.

with a measured 19% absorption at the excitation wavelength 1030 nm, the latter fluence equals to an average exciton occupancy per CQD of $\langle N^{th} \rangle_{las} = 0.87$. Figure 4.16b shows the collected lasing spectra (perpendicular to the surface) above the lasing threshold for neutral- (left panel) and doped-C/A-S CQDs (right panel) at N= 5.07 and 1.05, respectively. The single-mode lasing of neutral device is centered at 1660 nm within a linewidth of $\backsim$0.9 nm (0.41 meV), while doped device operates at 1670 nm having a linewidth of $\backsim$1 nm (0.46 meV). Optical images of the surface of the CQD-DFB device below and above the threshold given in Figure 4.16c. The laser device exhibits strong linear polarization with a ratio of polarization of $(I_{\parallel} - I_{\perp})/(I_{\parallel} + I_{\perp}) = 0.94$, where $I_{\parallel}$, $I_{\perp}$ are the lasing intensity parallel and perpendicular to the optical axis, correspondingly (Figure 4.16d). Finally, our laser device operated at room temperature for more than 8 hours under uninterrupted pumping at 10 kHz (Figure 4.16e), setting a new stability record for a CQD laser. Over this time, we did not witness any thermal or optical damage to the laser device.

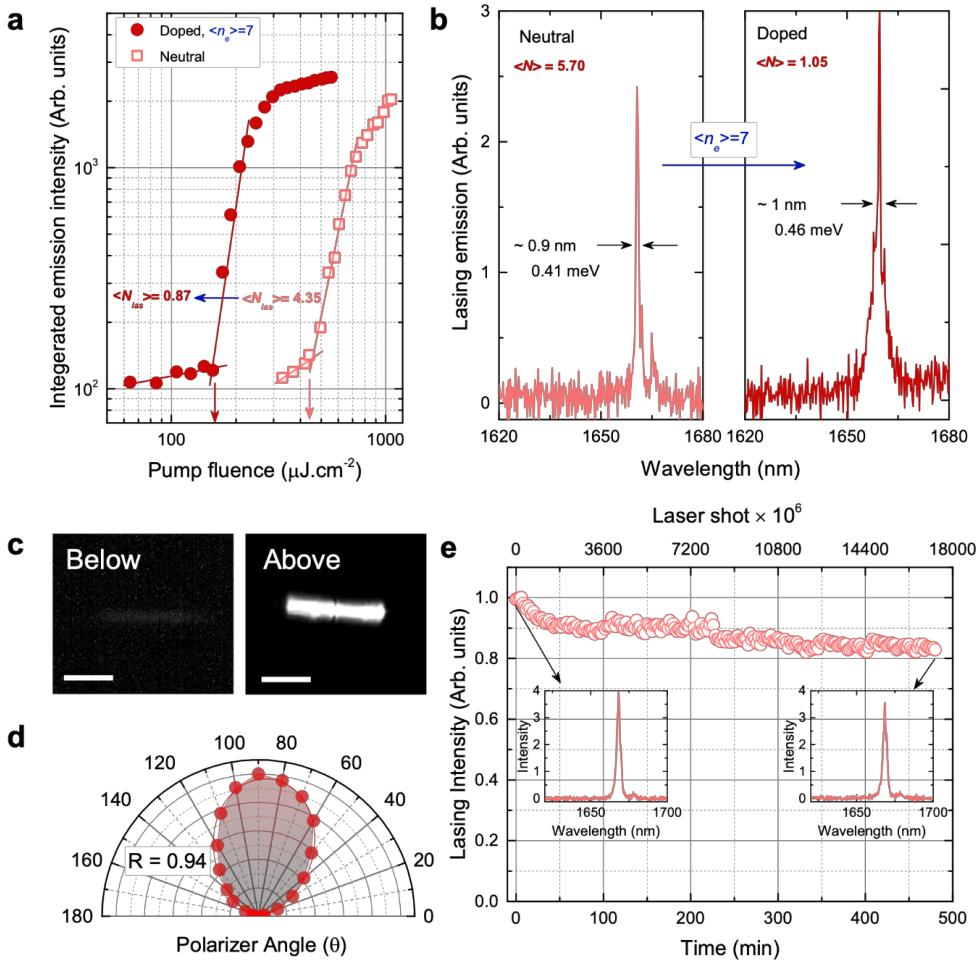

Figure 4.16: Sub-single-exciton infrared lasing demonstrated in doped-C/A-S CQDs device. (a) Integrated intensity of lasing peak of C/A-S CQDs (neutral doped) coupled to a second-order DFB grating (out-plane emission) versus excitation intensity. Note, open squares represent neutral CQDs and filled circles are for doped CQDs. By applying permanent doping to the devices, $\langle n_e \rangle = 0$ to 7, the lasing threshold decreases from $\backsim$430 to 160 $\mu J.cm^{-}2$, for which the latter equals to $\langle N_{las} \rangle$ =0.87. (b) Single mode lasing spectra for neutral- and doped- CQD/DFB devices at the corresponding fluences. Note, the exhibited spectra are just above the lasing threshold. (c) Infrared images of the device below and above the lasing threshold. The scale bars, 0.5 mm. (d) The polar plot represents the lasing emission intensity of the 1668 lasing mode as a function of the polarization angle (θ). Note, the solid line shows quadratic cosine function. "R" denotes the polarization ratio. (e) Stability of lasing intensity over the course of 8 h of continuous excitation at 10 kHz. Insets show the lasing spectra at the corresponding time (arrows) of the exposure. Reprinted with permission from Wiley [48], Copyright 2022. Wiley-VCH Verlag GmbH & Co. KGaA. Weinheim.

4.3 Summary

We have reported sub-single exciton gain and lasing in an infrared CQD laser, matching the performance of previously reported visible counterparts, albeit infrared CQDs possess an 8-fold state degeneracy. This was achieved by employing a PbS/PbSSe C/A-S CQD heterostructure doped up to almost filling the first excited state with 7 electrons per dot. This synergistic effect facilitated suppressed Auger recombination evidenced by a gain lifetime of 300 ps and very high gain on the order of 10^3. Our work facilitates a path towards the realization of practical infrared laser devices for silicon integrated photonics.

5

Toward colloidal quantum dot laser diodes: Optically-pumped infrared stimulated emission in LED device

"Nothing is too wonderful to be true if it be consistent with the laws of nature."

-Michael Faraday

In this chapter, we introduce a novel method and structure to address two fundamental challenges toward the realization of the electrically-driven CQD-laser. To reach this major breakthrough, we demonstrate the optical gain in a ultra-thin active medium that would allow efficient electrical injection as well as the demonstration of stimulated emission in a real LED device. In doing so, we employ a binary blend of CQDs comprising a host matrix of ZnO NCs serving as nano-sized scatterers and PbS CQDs as the emitting media. Incorporation of ZnO NCs allowed us to achieve stimulated emission beyond the slab waveguide theoretical limit. Next, we employed such a thin active media in a full-stack LED to demonstrate the first dual function device, showing infrared electroluminescence and stimulated emission.

This chapter is based on the publication "Ultra-thin Infrared Optical Gain Medium and Optically-pumped Stimulated Emission in PbS Colloidal Quantum Dot LEDs," N. Taghipour, G. L. Withworth, A. Othonos, M. Dalmases, S. Pradhan, Y. Wang, G.

Kumar and G. Konstantatos, vol. 34, no. 3, pp. 1–8, (2022). Adapted or Reproduced with permission from John Wiley and Sons. Copyright 2022. Wiley-VCH Verlag GmbH & Co. KGaA. Weinheim.

5.1 Motivation

Recent efforts have paved the way for the realization of room-temperature solution-processed infrared lasers which so far are optically pumped [28,29,44,45,127]. However, nonradiative Auger process results in extremely fast (typically sub-100 ps) deactivation of gain in CQDs and high operating thresholds. These highly complicate the realization of gain/lasing especially in the case of practical devices including direct current electrical and continuous wave (C.W.) optical excitation. Recent progress in the development of practical methods for engineering Auger process in infrared-emitting CQDs, leads to achieve efficient optically-pumped infrared lasers with low operating thresholds and long optical gain lifetimes. On the other hand, in order to unleash the potential of this technology for a broad range of applications covering optical communications, silicon photonics, LIDAR and medical applications, the optical gain medium needs to be excited electrically, which is the "Holy Grail" in the CQD field.

To eventually realize electrically-driven infrared stimulated emission and lasing in CQDs, the following challenges should be addressed: 1) to demonstrate optical gain in a full-LED device stack including conductive layers and contacts, 2) to obtain net gain and stimulated emission in ultrathin film gain media in order to facilitate efficient electrical injection and 3) to increase the robustness of the device upon high current density needed to achieve population inversion [32,79]. It is noteworthy that although Klimov and colleagues has shown lasing action in LED-like device in the visible emitting CQDs [79], none of those devices include the anode electrode which is crucial for a true EL device where the lasing emission was observed to disappear in the vicinity of electrical contacts because of the optical losses.

5.2 Result and discussion

In this section, we introduce a novel LED structure to address the first two challenges and demonstrate a functional EL device in a full-stack all colloidal LED device, which exhibits stimulated emission under optical excitation. In chapter 3, we showed that blending ZnO NCs with PbS CQDs allow us to improve the electronic properties of PbS CQDs as the gain material toward supression of Auger process and obtaining low-threshold ASE/lasing devices. Herein, we demonstrate an EL device architecture with

a PbS/ZnO blend acting as the thin film active media of an LED device. Additional to improving ASE performance, the ZnO NCs are also observed to form nanoclusters that act as scattering sites that facilitate ASE propagation below the waveguide cut-off thickness. By carefully adjusting the loading amount of ZnO in PbS/ZnO blend, we are able to attain stimulated emission at a record subwavelength gain medium thickness of 16 nm (i.e., $\lambda/100$). Importantly, stimulated emission is also realized in a complete LED device structure including an anode electrode that is made of a single layer of graphene.

5.2.1 ASE characterizations of thin films

The standard architecture for demonstrating ASE in a thin film is a slab waveguide where the stimulated emission is confined in a high refractive index gain medium. A homogenous thin film asymmetric waveguide has a minimum thickness for which it can still support a guiding mode for a given wavelength. We posited that the presence of low refractive index ZnO NCs blended with PbS CQDs active medium at the nanoscale would allow us to overcome this critical thickness threshold by assisted scattering induced by ZnO nano-clusters. Figure 5.1a illustrates the configuration for ASE measurements of the thin films, showing how spontaneous emission is propagated in-plane, and then amplified along the pump stripe. The resultant ASE signal is then collected at the edge of the film, perpendicular to the excitation beam. Using our proposed architecture, we would be able to achieve ASE in the thicknesses that are required for high current injection in LED structures. Using scanning transmission electron microscopy (STEM)-energy dispersive X-ray spectrometry (EDS) elemental mapping, shown in Figure 5.1b superposed on a dark field image, the ratio of Pb to Zn was measured to be 68:32%. From TEM images, we extracted the diameter of PbS CQDs and ZnO NCs as ≈5.8 and 6 nm respectively, and as shown in Figure 5.1b, ZnO NCs tended to form nano-clusters. Furthermore, the scanning electron microscopy (SEM) images of bare-PbS and PbS/ZnO blends are displayed in Figure 5.1c and 5.1d, respectively. As can be seen, introducing ZnO NCs improved the uniformity of the thin film formation which can be attributed to better nucleation of PbS CQDs during the spin-coating process. This results in a smooth thin film gain medium with the PbS/ZnO blend, in which the surface coverage reaches near unity for a single layer deposition, with no noticeable cracks or voids.

To investigate the optical gain performance of our devices, we spin-coated the PbS/ZnO blend, with a ratio of 7:3, on a glass substrate. We controlled the thickness of the samples via repeated spin-coating and ligand exchange procedures. We employed atomic force microscopy (AFM) to assess the thickness and surface morphology of our

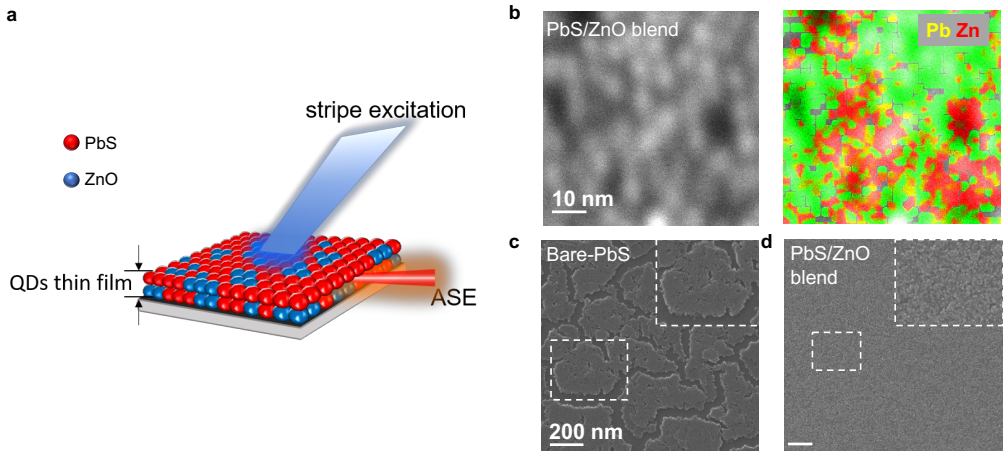

Figure 5.1: Characterization of bare-PbS and PbS/ZnO blend samples. (a) Schematic illustration of ASE measurement. (b) STEM-EDS elemental mapping PbS/ZnO blend, where Pb:ZnO is 68:32%. SEM image of a single layer of (c) bare-PbS and fd PbS/ZnO blend on silicon substrate. Insets show the zoom-in image of the indicated region. Reprinted with permission from Wiley [33], Copyright 2022. Wiley-VCH Verlag GmbH & Co. KGaA. Weinheim.

samples, the results of which are illustrated in Figure 5.2 where the thickness of the film is measured to be ≈16 nm with an r.m.s. value of 0.86 nm. ASE from a sample as thin as ≈16 nm $\left(\frac{\lambda}{100}\right)$ are plotted in Figure 5.3a as a function of pump fluence.

Figure 5.3b depicts the integrated intensity of the ASE spectra against pump fluence along with the corresponding FWHM of each spectrum. The photoluminescence (PL) intensity increases linearly with pump intensity at low fluences and then exhibits a super-linear behavior above the threshold of 2.9 $mJ.cm^{-2}$, a clear signature of light amplification above the ASE threshold, the FWHM of the spectra drastically drops from ≈125 nm to ≈17 nm. To the best of our knowledge, this is the thinnest attained thickness for ASE using a colloidal gain medium with a thickness of ≈16 nm and an ASE peak wavelength of ≈1675 nm. Note that 16 nm is below the theoretical waveguide cut-off thickness or a homogenous medium at this wavelength (56 nm). As discussed above, for electrically pumped CQD lasers, it is essential to achieve an optical gain in ultra-thin films in order to facilitate charge injection into the active medium for achieving population inversion; as thin-active media results in a balanced carrier supply to the CQDs [95]. Furthermore, as shown in Figure 5.4a, by increasing the thickness of the PbS/ZnO films, the ASE peak is gradually blue-shifted. For instance, the ASE peak for a 70 nm thick film appears at ≈1604 nm. This blue-shifting of the ASE peak can be attributed to the increased scattering in thicker films. The ASE thresholds for films with varying thicknesses are summarized in Figure 5.4b, decreasing from 2.9 to

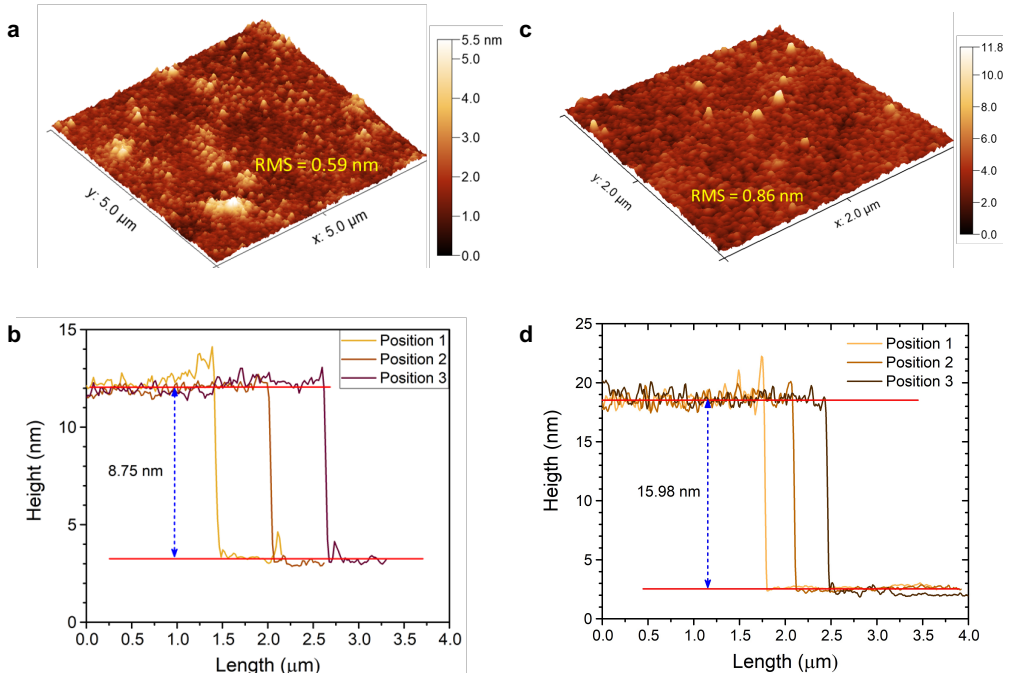

Figure 5.2: AFM image showing morphology of PbS/ZnO blend thin film having a thickness of ∽9 and 16 nm (a,c) along with height profile of PbS/ZnO blend thin film (b,d). Reprinted with permission from Wiley [30], Copyright 2022. Wiley-VCH Verlag GmbH & Co. KGaA. Weinheim.

0.5 $mJ.cm^{-2}$ having a film thicknesses of 16 and 140 nm respectively. We measured net optical gain (G) and waveguide loss coefficients (α) for bare-PbS and PbS/ZnO blend with varying thickness via VSL technique. The VSL measurements and calculated G are depicted in Figures 5.5. At similar pump fluences, G is lower in the PbS/ZnO blend compared to bare-PbS films due to the reduced amount of gain material in the blend. Similarly, thanks to the reduction of re-absorption losses in blends, α dropped to 9 cm^{-1} in PbS/ ZnO blend sample within a thickness of ≈25 nm, while it is 23 cm^{-1} for bare-PbS samples having a thickness of ≈110 nm. The analyses for calculating waveguide loss coefficient are shown in Figure 5.6 for different cases.

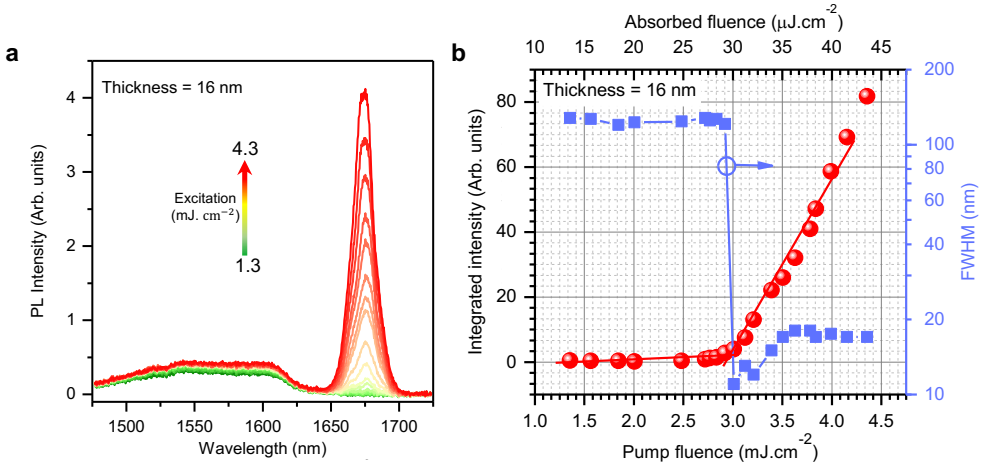

Figure 5.3: (a) ASE spectra from a blend of PbS/ZnO (30%), having a thickness of 16 nm, as a function of fluence. (b) Normalized integrated intensity of the spectra as a function of pump fluence, with corresponding FWHM. Reprinted with permission from Wiley [30], Copyright 2022. Wiley-VCH Verlag GmbH & Co. KGaA. Weinheim.

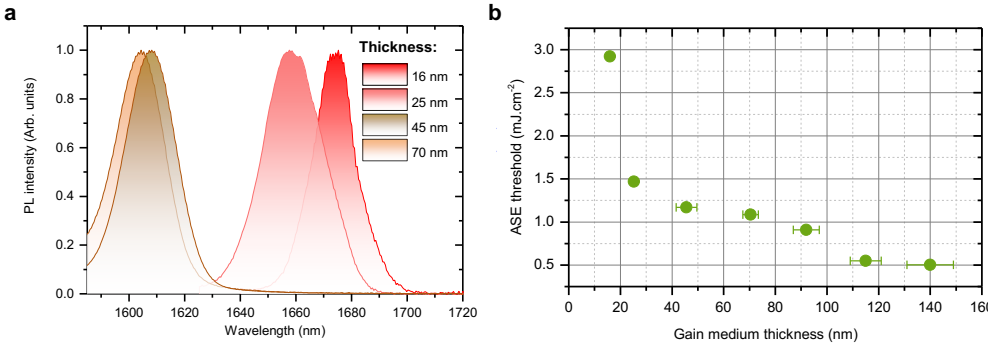

Figure 5.4: (a) Emission spectra of PbS/ ZnO (30%) blend sample with different thicknesses of 16, 25, 45 and 70 nm. (b) Evolution of ASE threshold with increasing thickness of thin films. Reprinted with permission from Wiley [30], Copyright 2022. Wiley-VCH Verlag GmbH & Co. KGaA. Weinheim.

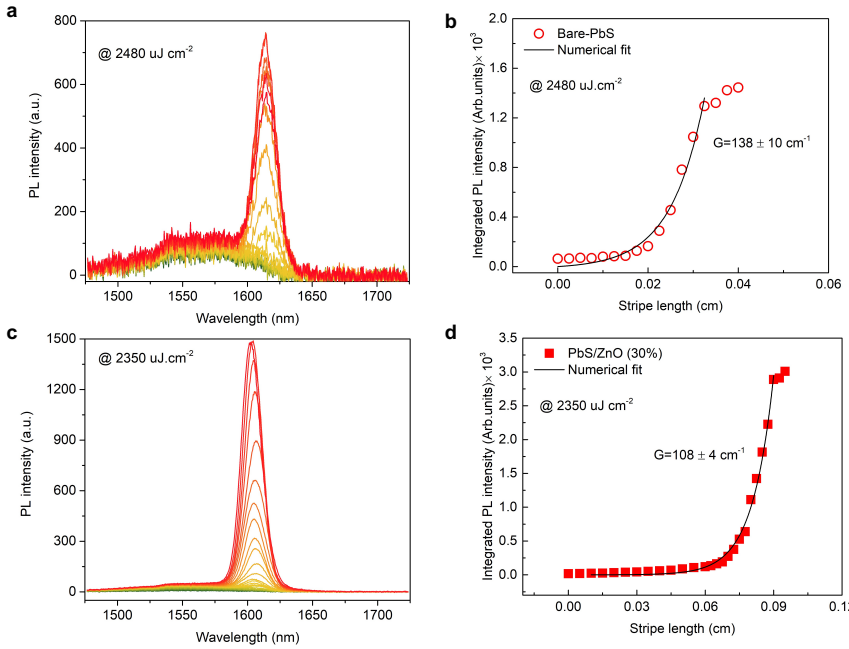

Figure 5.5: VSL characterizations. ASE spectra as a function of stripe length for bare-PbS (a) and PbS/ZnO blend (c). (b,d) Integrated PL intensity versus stripe excitation length, showing 138 ± 10 cm-1 (for bare-PbS) and 108 ± 4 cm-1 (for PbS/ZnO(30%) blend). Reprinted with permission from Wiley [30], Copyright 2022. Wiley-VCH Verlag GmbH & Co. KGaA. Weinheim.

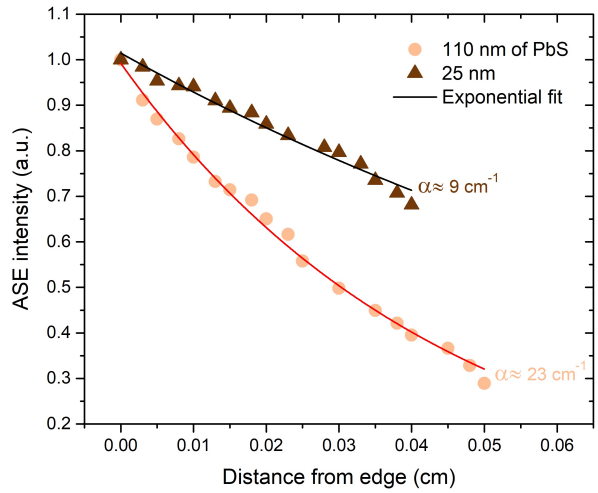

Figure 5.6: Waveguide loss coefficient measurement for bare-PbS and PbS/ZnO (30%) blend devices within a thickness of 25 and 110 nm. Reprinted with permission from Wiley [30], Copyright 2022. Wiley-VCH Verlag GmbH & Co. KGaA. Weinheim.

5.2.2 Full electromagnetics model

To gain further insights into our experimental ASE observations of the CQD ultra-thin films, we employed a full-field electromagnetic numerical model. In principle, our structure can be modeled as an asymmetric slab waveguide, in which the gain medium is sandwiched between semi-infinite fused silica and air layers. Figure 5.7a,b depict the asymmetric planar waveguide enabling electromagnetic modes to propagate along the waveguide, while fundamental transverse electric field (TE) and transverse magnetic field (TM) modes require a minimum thickness to be confined inside the active region. The critical thicknesses for TE and TM can be calculated from the following expressions [128]:

$$t_{TE} = \frac{\lambda}{2\pi\sqrt{n_2^2 - n_3^2}} \left[m\pi + \arctan\left(\sqrt{\frac{n_3^2 - n_1^2}{n_2^2 - n_3^2}} \right) \right] \tag{5.1}$$

$$t_{TM} = \frac{\lambda}{2\pi\sqrt{n_2^2 - n_3^2}} \left[m\pi + \arctan\left(\frac{n_2^2}{n_1^2} \sqrt{\frac{n_3^2 - n_1^2}{n_2^2 - n_3^2}} \right) \right] \tag{5.2}$$

Using Equations 5.1 & 5.2, the waveguide cut-off thickness is plotted against wavelength in Figure 5.7c for the fundamental TE and TM modes (m = 0). For λ = 1675 nm, the minimum thicknesses for propagation of TE_0 and TM_0 in PbS solid film are 56 and 158 nm, respectively. However, for PbS/ZnO blends, t_{TE_0} and t_{TM_0} are 106 and 220 nm. In PbS/ZnO blends, the onset experimental thickness for observing ASE signal in thin film configuration is ≈16 nm (Figure 5.3a). Therefore, the mode confinement in our architecture does not obey the rules of a conventional slab waveguide. We modeled our thin film devices using an FDTD solver (see Appendix B.6 for details). In the case of bare- PbS, the thin film of CQDs is approximated as a homogenous medium, while for PbS/ZnO blend, the ZnO NCs are located inside the homogenous medium of PbS thin film as shown in Figure 5.7b. Note, the loading of ZnO NCs is 30% of the whole volume, which was extracted from STEM-EDS mapping images (see Figure 5.1b). In our model, the semi-infinite SiO_2 substrate extends from $z = -\infty$ to $z = 0$, the active medium spreads from $z = 0$ to $z = 16$ nm, and above the structure is air. Figure 5.8a plots the electric field (E-field) intensity distribution in z-direction ($|E_z|^2$) along the lateral direction of the sample at different z positions within a bare-PbS film, where the majority of E-field propagates in the substrate and air. Figure 5.8b displays the E-field distribution over the xy-plane (in the middle of the gain medium, $z = 8$ nm)

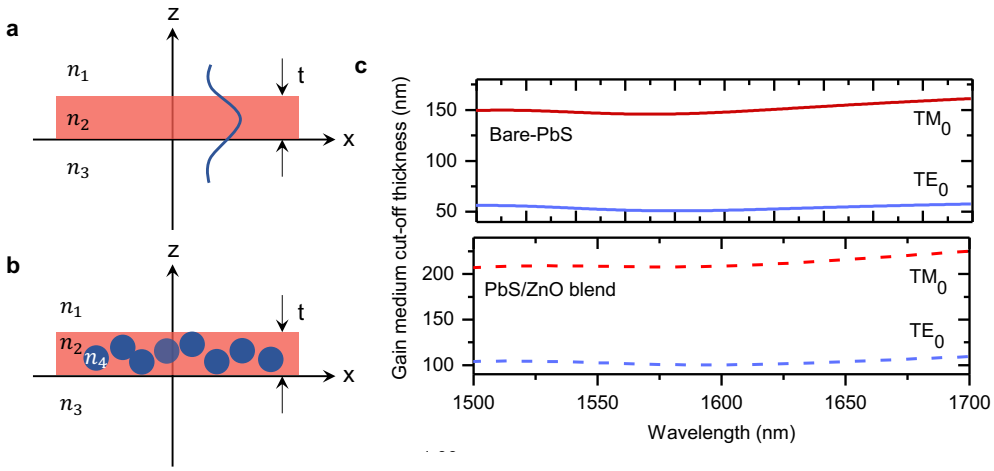

Figure 5.7: Full numerical electromagnetic model. (a,b) Schematic drawing of an asymmetric slab-waveguide made of bare-PbS (a) and a PbS/ZnO blend (b). (c) Calculated gain medium cut-off thickness for supporting fundamental TE and TM in bare-PbS (top panel) and PbS/ZnO blend (bottom panel) devices as a function of wavelength. Reprinted with permission from Wiley [30], Copyright 2022. Wiley-VCH Verlag GmbH & Co. KGaA. Weinheim.

and xz-plane for bare-PbS thin film, where there is no abrupt change in the E-field intensity. However, in the PbS/ZnO blended thin film, the E-field is enhanced at the position of ZnO nano-clusters owing to the strong scattering of light as can be seen in Figure 5.8c (dark blue line, $z = 8$ nm which is the middle of the gain medium). Although similar behavior is also observed at the interfaces, the intensity of scattering is significantly larger at the center of the gain medium ($z = 8$ nm). Also, as shown in Figure 5.8d, the E-field intensity is significantly enhanced at the surface of ZnO NCs where due to the cluster formation of ZnO NCs, the electromagnetic wave propagates between these nano-clusters. Another notable observation is the emergence of a propagation mode in PbS/ZnO blend sample, where the E-field intensity exhibits a maximum in the gain medium, while there is no variation of E-field intensity in the bare-PbS case as depicted in Figure 5.9.

For better understanding the role of ZnO nano-clusters in providing the ASE at thicknesses thinner than cut-off thickness of slab-waveguide architecture, we simulated two different case, the results shown in Figure 5.10. We depict our proposed PbS/ZnO blend heterostructure in Figure 5.10a. While in Figure 5.10b, we set the refractive index of ZnO NCs to 1 which is an artificial heterostructure called as PbS-etch. We calculated the mean distance by fitting the Electric field intensity ($|E|^2$) variation along the lateral side of samples at the middle (z =8 nm) of the bare-PbS and PbS/ZnO

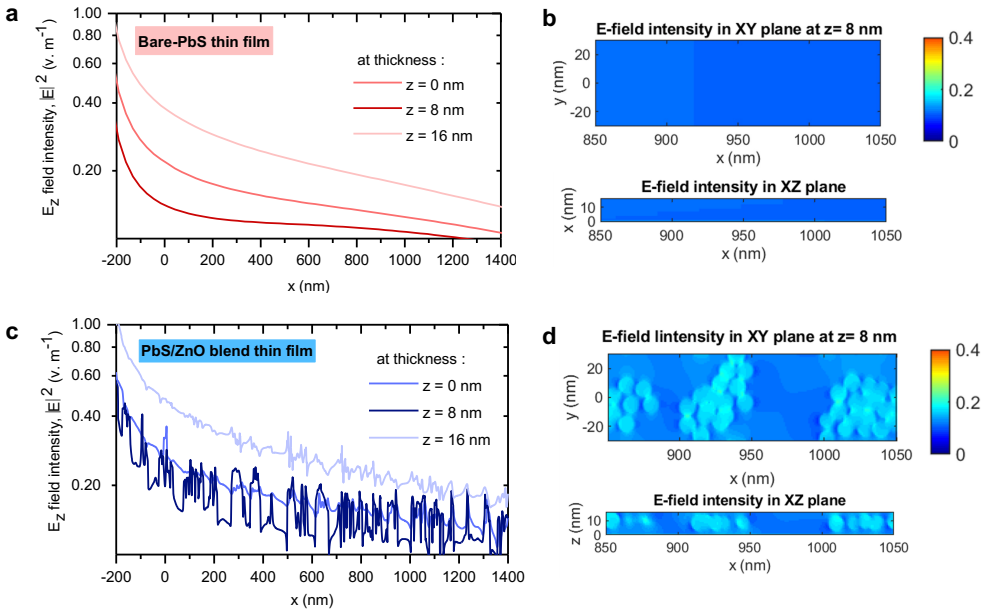

Figure 5.8: (a,c) Electric field intensity ($|E|^2$) variation along the lateral side of the samples at different heights for bare-PbS (a) and PbS/ZnO blend (c). (b,d) Electric field distribution along xy-plane and xz-plane for bare-PbS (b) and PbS/ZnO (d). Note, all E-fields are recorded at ASE wavelength of 1675 nm. Reprinted with permission from Wiley [30], Copyright 2022. Wiley-VCH Verlag GmbH & Co. KGaA. Weinheim.

blend samples (shown in the Figure 5.8a & c) to the exponential function of:

$$A_0 e^{-rx} + c_0 \tag{5.3}$$

where, r is the decay rate, the x is the propagation length, A_0 and c_0 are arbitrary constants. Here, mean distance is the length x where the field intensity drops to $1/e$, which is approximately $1/r$ as $c \ll 1$. We also added the PbS-etch into comparison. The intensity graphs and fitted functions are shown below. The calculated mean distances are compared as: $\frac{d_{PbS/ZnO}}{PbS} = 1.5$ and $\frac{d_{PbS/etch}}{PbS} = 1.7$. As expected, owing to the scattered filed from ZnO NCs, the normalized mean length is increased in both our proposed PbS/ZnO blend and PbS-etch devices. Also, the mean length is enhanced more in PbS-etch compared to PbS/ZnO case stemming from stronger scattered field.

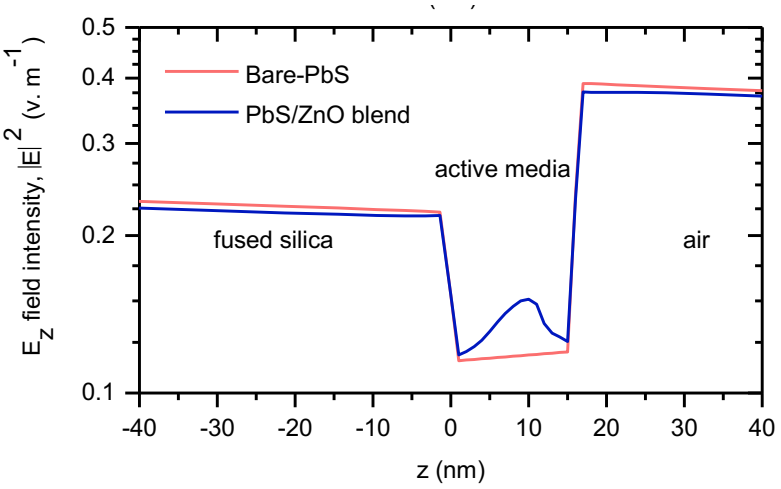

Figure 5.9: Electric field intensity ($|E|^2$) variation along vertical direction of the samples for bare-PbS and PbS/ZnO blend. Note, the thin film extends from 0 to 16 nm. Reprinted with permission from Wiley [30], Copyright 2022. Wiley-VCH Verlag GmbH & Co. KGaA. Weinheim.

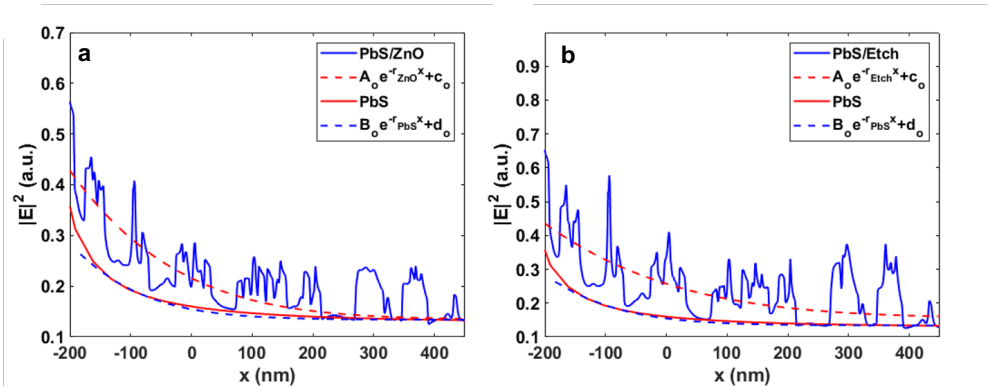

Figure 5.10: Electric field intensity ($|E|^2$) variation along the lateral side of samples at the middle (z =8 nm) height and corresponding exponential fits; (a) for bare-PbS and PbS/ZnO blend, and (b) for bare-PbS and PbS/Etch blend. Reprinted with permission from Wiley [30], Copyright 2022. Wiley-VCH Verlag GmbH & Co. KGaA. Weinheim.

5.2.3 Dual functional LED device

Finally, we fabricated a complete LED device stack comprising of engineered indium tin oxide (E-ITO) as a cathode electrode, a layer of ZnO NCs acting as electron transport layer (ETL), the PbS/ZnO blend as active medium (0.8 eV band gap PbS CQDs), a hole transport layer (HTL) made from large-band gap PbS CQDs (1.77 eV), and a single layer of graphene serving as the anode electrode. We engineered the optical constant of as-deposited ITO, to achieve a transmission of above 85% across our operating wavelength window (see Appendix A.6 for detailed information) [128] allowing us to observe stimulated emission on E-ITO substrates. Un-engineered ITO, in contrast, has transmission values down to as low as 60%, adding to much optical loss for an ASE signal to propagate along the sample. Note, the thickness of the ETL, gain medium and HTL are around 40, 80 and 20 nm, respectively. Figure 5.11a is a schematic illustration of the tested LED structure exhibiting electrically injected infrared spontaneous emission (SE), as well as showing infrared ASE under optical laser excitation. The bias-dependent LED device exhibits infrared SE at a wavelength of 1563 nm as shown in Figure 5.11b. Moreover, the infrared images of the LED device taken from the surface of the structure are depicted in Figure 5.11c. At 2 V the LED is in the off-state, while at 5 V it is in the on-state. By applying sufficient bias to the electrodes, bright infrared emission is clearly visible from the graphene-covered portion of the device. By pumping our LED device under stripe excitation of a femtosecond laser (fs-laser), we observed infrared stimulated emission peaks at 1607 nm as depicted in Figure 5.11d. The corresponding integrated intensity of ASE spectra versus excitation fluence is shown in Figure 5.11e for both with and without top electrode (i.e., graphene layer). The ASE threshold for the case of without graphene is $\approx$820 $\mu J.cm^{-2}$ which then increases slightly to 840 $\mu J.cm^{-2}$ when the graphene was placed on top. This can be attributed to the graphene transfer procedure (see Appendix A.7). Then, our proposed LED architecture allows us to achieve stimulated emission in full all-colloidal LED stack device as a first account.

5.3 Summary

we report near-infrared stimulated emission in a record thin colloidal gain medium. Our novel PbS/ZnO blends strongly interact with photons due to nano-cluster scatterers, resulting in propagation of generated stimulated emission along the surface of the devices below the fundamental cut-off thickness for an asymmetric slab waveguide. Moreover, for the first time we show ASE in full-stack LED structure made of CQDs as the gain medium under optical excitation. In our LED device, we employed a single

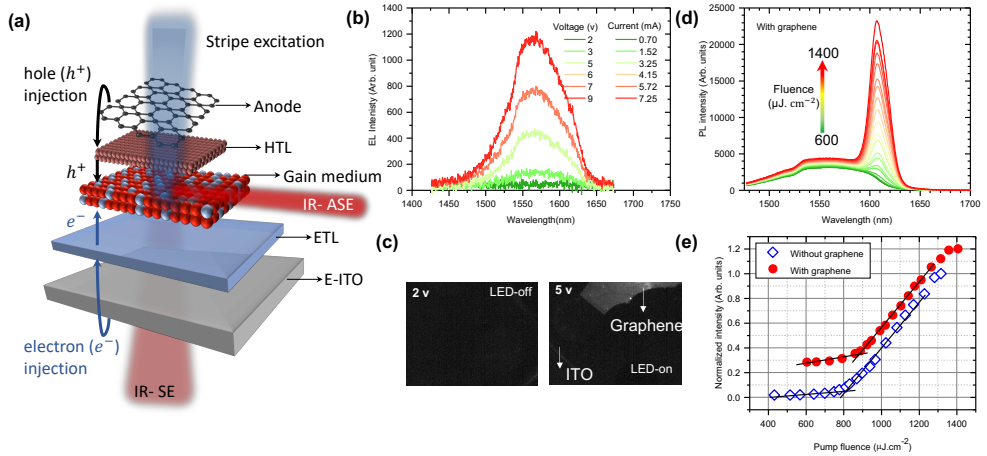

Figure 5.11: A full-LED device stack as both optically-pumped infrared-ASE and electrically-driven infrared-SE device. (a) Schematic illustration of a complete LED structure. (b) SE spectra of electrically excited LED as a function of bias voltages. (c) Infrared images taken from the surface of the LED structure under 2 V and 5 V where LED is -off and -on, correspondingly, with the graphene layer indicated. (d) ASE spectra as a function of excitation fluence under femtosecond laser pumping in full-LED device, where the anode layer is made of a single layer of graphene. (e) Normalized integrated intensity of ASE spectra against pump fluence for the devices with and without anode electrode. Reprinted with permission from Wiley [30], Copyright 2022. Wiley-VCH Verlag GmbH & Co. KGaA. Weinheim.

layer of graphene as an anode electrode instead of the conventional metals which results in quenching of ASE mode in the gain media. Our results will pave the way to realize a true electrically-driven laser made of CQDs as the gain medium.

6

Conclusions and Outlook

"The present is the only things that has no end."

-Erwin Schrödinger

6.1 Conclusion

In this Thesis, we have investigated the excitonic properties of colloidal semiconductor nanocrystals and their hybrids to accomplish high-performance solution-processed infrared optical gain and lasing devices. In doing so, we have proposed, developed, and demonstrated new generation of colloidal nanocrystals systems including binary nanocomposites of CQDs and NCs and heterostructured core/alloyed gradient-shell CQDs, to overcome the long-standing fundamental and practical challenges in infrared CQD-based lasers. In particular, using these novel structures allows us to address the poor optical gain performance of infrared-emitting conventional CQDs including high lasing thresholds, fast Auger recombination, short optical gain lifetime, and low modal gain coefficients. Furthermore, we addressed the practical limitations in the demonstration of stimulated emission in true LED devices.

We showed in chapter 3 that using a remote charge passivation mechanism induced by an appropriate matrix allowed us to suppress Auger process in PbS CQDs. This robust method enabled us to significantly reduce the density of trap states, which cause

trap-assisted Auger recombination in PbS CQDs. Integrating this novel active medium which formed as binary blend of PbS/ZnO into a DFB resonator lowered the lasing threshold with unprecedented operational stability for a CQD-laser.

In Chapter 4 we showed that combining core/gradient-alloyed shell heterostructured CQDs for hindering Auger process with permanently doping for suppressing ground-state absorption can reduce the lasing threshold below single exciton level per dot in 8-fold degenerate system. Employing PbS/PbSSe as the gain media enabled us to achieve record low gain threshold along with record long optical gain lifetime among all solution-processed infrared gain materials. Furthermore, we obtained record high modal gain coefficient which is comparable with the commercial epitaxially grown infrared-emitting semiconductors.

Finally, we demonstrated a LED structure operating as a dual functional device which emits strong infrared electroluminescence under electrical injection and shows stimulated emission under optical excitation. The active medium is made of binary blend of PbS as the emitting gain media and ZnO nanoclusters as the scatterers, which enabled us to demonstrate stimulated emission in record ultrathin gain medium. Specifically, the anode and cathode electrodes in our proposed LED architecture are made of a single of graphene and engineered-ITO. Using these contacts allowed us to achieve stimulated emission in full-stack LED device for the first time which had remained a challenge due to optical losses.

In overall, the findings in this Thesis develop the understanding photophysical properties of infrared-emitting CQDs and present the state-of-the-art performance in infrared CQD-laser devices. The results addressed fundamental challenges including demonstration of low threshold (sub-single-exciton) infrared lasing using and obtaining ultrahigh modal gain coefficient employing charged exciton gain mechanism in heterostructured quantum dots. Also, practical limitations toward CQD-laser diode was tackled using all colloidal dual functional device that operates as infrared laser and a standard LED. These findings prove the feasibility of making infrared CQD lasers with technologically relevant performance and pave the way towards the making of electrically driven laser diodes for silicon integrated photonics.

6.2 Outlook

In this Thesis, we employed pulsed femtosecond laser as the excitation source. However, for realization of the practical CQD-lasers, one needs to use CW lasers or electrical injection. The CW lasing threshold (P_{CW}) can be calculated from $P_{CW}=\frac{P_{pul.}}{\tau_g}$, here

$P_{pul.}$ is the lasing threshold (i.e., pump fluence) under pulsed excitation and τ_g is the stimulated emission lifetime [42]. In this thesis, our achieved lowest lasing threshold in this Thesis is 100 $\mu J.cm^{-2}$ within a gain lifetime of 300 ps obtained in charged-C/A-S CQDs, then P_{CW} ≈300 kW.cm^{-2} which still is not feasible to achieve gain under CW excitation. Therefore, the lasing threshold should be further reduced and simultaneously elongate the gain lifetime. As we shown in our results, smoothening the potential confinement at the core/shell interface results in the suppression of Auger recombination. For further suppression, one needs to increase the shell thickness which should lead to lowering the lasing threshold and elongation of the gain lifetime [62,64,129]. Using this type of heterostructure in visible-emitting CQDs (i.e., CdSe-based) results in ultralong gain lifetime $>$ 2 ns [37,42,62,118].

Moreover, lasing threshold can be further reduced by blending doped core/shell heterostructure with a large band gap CQDs, in which the first acts as gain medium and the second acts as carrier supplier. Similar methods have previously utilized for increasing the performance of optoelectronics devices such as LEDs [92,95]. In particular, the rate of excitons transfer from the carrier supplier CQDs to the gain medium is expected to be larger than stimulated emission. Given this, the required number of carriers for achieving lasing threshold is lower than bare emitting case. Additionally, employing such an active media should lead us to achieve carrier balance in the case of electrical injection, which is crucial for laser diode device.

Appendices

A

Experimental methods: Device fabrication

A.1 Synthesis of nanocrystals

Synthesis of PbS CQDs: PbS CQDs were synthesized by a multiple injection method, under inert atmosphere. Briefly, for 5.6 nm PbS CQDs, 0.446 g PbO, 3.8 mL oleic acid, and 50 mL 1-octadecene (ODE) were pumped for 1 h at 100 °C to form lead oleate. Once under argon, the solution was kept at 100 °C and a solution of 70 μL hexamethyldisilathiane (HMS) in 3 mL ODE was quickly injected. After 6 min of reaction, a second solution of 90 μL HMS in 9 mL ODE was dropwise injected. Afterwards, the solution was cooled down naturally to room temperature and PbS CQDs were precipitated with the addition of a mixture of acetone/ethanol, redispersing in anhydrous toluene. This process was repeated two more times for further purification. Finally, the concentration of PbS CQDs was adjusted to 30 mg mL^{-1} and the solution was stored in the glovebox to avoid oxidation. NCs size was tuned by the variation of the amount of HMS used in each solution. For 5.8 nm CQDs 65 μL HMS was used in the first injection, and 75 μL in the second. For 6.2 nm CQDs, the amount of HMS added in the first injection was 60 μL and in the second, 80 μL.

Synthesis of PbS@PbSSe core-shell CQDs: To grow a PbSSe shell on PbS core CQDs, 240 mg PbO, 10 mL ODE and 1.1 mL OA were heated at 100°C under vacuum, for 1h, to form the lead precursor. After, the solution was changed to argon atmosphere, the temperature was set to 140°C and 2 mL of PbS-ODE solution were injected. When the temperature was recovered, the selenium precursor solution was injected (96 mg Se powder dissolved in 1.3 mL tetrabutylphosphine). The growth of the shell can be followed by absorption spectroscopy. When the thickness of PbSSe shell was the appropriated, the reaction was quenched cooling it down with a water bath. The CQDs were washed three times with ethanol, redispersing in toluene. Finally, the concentration was adjusted to 30 mg/mL.

ZnO NCs Synthesis: ZnO NCs were synthesized based on the method shown previously [94]. First, zinc acetate dihydrate (2.95 g) was dissolved in methanol (125 mL) on a 250 mL flask, under continuous stirring, and the temperature was set at 60 °C. Simultaneously, another solution was prepared by dissolving 1.48 g of KOH in 65 mL of methanol. The prepared solution of KOH was slowly (in 4 min) added to the zinc acetate solution and the reaction was left unchanged for 2.5 h. After completion of the reaction, the heating was removed, and the solution was led to slowly cool down to room temperature under constant stirring. Prepared ZnO NCs solution was centrifuged at 3500 r.p.m. for 5 min. Then, the supernatant was discarded and the remaining NCs were dispersed in methanol, this centrifuge process was repeated three times. Finally, the ZnO NCs was dispersed in a solution of 5% butylamine in toluene for making the binary blend solutions, and in 2% butylamine in chloroform for formation of the base layer.

A.2 CQD thin film deposition

Active Layer Deposition: The schematic of the process is shown in Figure A.1. Active layer was formed on the desired substrate by spin coating technique. First, the substrate was covered with 50 μL of CQDs solution and spin coating started after 5 s, within a spin speed of 2500 r.p.m. for 15 s. Then, a mixed ligand of ZnI_2/ MPA (mixing of 25 $\times 10^{-3}$ M zinc iodide (ZnI_2) in methanol and 0.015% 3-mercaptopropionic acid (MPA) in methanol) was added on the formed surface (II stage). The spin coating was started after 7 s, at a spin speed of 2500 r.p.m. for 60 s, while a few drops of methanol were poured in order to clean the film from any unwanted organics (III stage). After washing out the excess ligand, spin coating continues for 20 s till CQDs solid film was formed (IV stage). These steps were repeated until reaching the desired thickness. The concentration of CQDs was set to 30 mg.mL^{-1} .

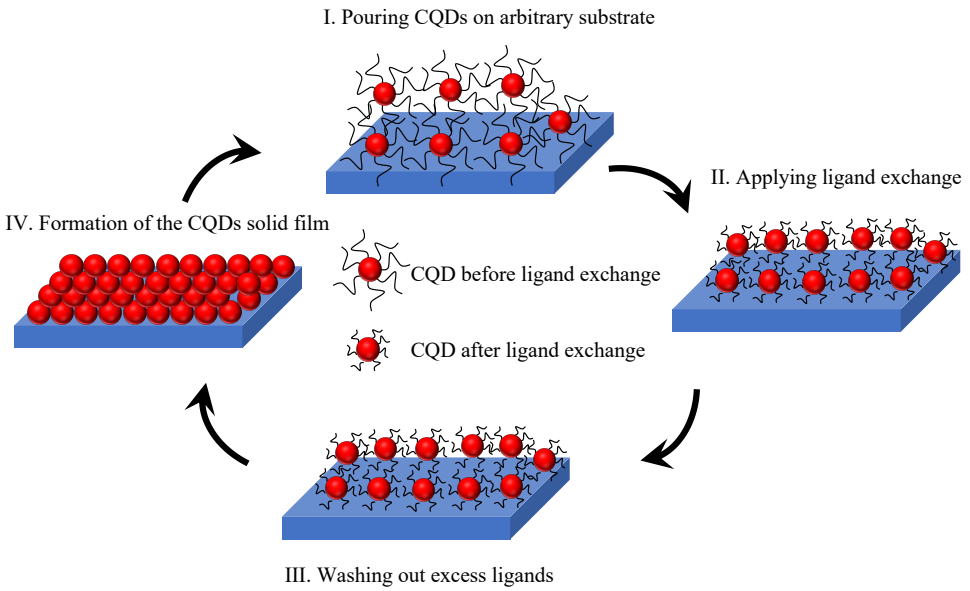

Figure A.1: Schematic of layer by layer active layer deposition of CQDs

In particular case of PbS/ZnO blend devices, before mixing, the ZnO NCs were prepared in separate vials with the same concentration (30 mg.mL^{-1}). For PbS/ZnO binary blend solutions, the PbS CQDs solution was mixed with ZnO solution at different volume ratios. Doping of CQDs obtained by a subsequent atomic layer deposition of alumina, which removes the atmospheric electron acceptors (water/oxygen) from the surface of the CQDs. Also, it encapsulates the film.

A.3 DFB lasers

Distributed feedback (DFB) cavity: In this thesis, we employed DFB structure as the optical resonator for our laser devices. DFB resonator provides the resonance frequency for lasing action based on waveguiding, in which the optical feedback is achieved by an adjacent diffractive structure. Figure A.2 shows the schematic of one- and two-dimensional DFB resonator. DFB lasers show exceptional mode selectivity for lasing and are compatible with solution processing of CQDs gain media.

Waveguides: To understand the principle of DFB lasers, we need to briefly discuss about the fundamental of waveguiding. Figure A.3 represents a basic waveguide, in which the light confined in the active medium by total internal reflection ($n_2 > n_1 \geq n_3$). Here, our analysis is based on ray optics theory. Then, for waveguiding, in addition to the angle of the propagation being larger than the critical angle, the successive wavefronts

should be in the same phase orthogonal to the propagation direction (indicated by black dots in Figure A.3). Therefore, the total phase change for a guided mode in the slab waveguide must be a multiple of 2π [130, 131]:

$$2k_0 \sin(\theta) - 2\varphi_{21} - 2\varphi_{31} = 2m\pi \qquad m = 0, 1, 2, ... \tag{A.1}$$

here, k_0 is the wave vector of the free space ($k_0 = \frac{2\pi}{\lambda}$), φ_{21} and φ_{31} are the phase shift because of the reflection at the interfaces and m is integer. φ_{21} can be calculated from the following expressions for TE and TM polarizations:

$$\text{TE mode:} \qquad \varphi_{21} = tan^{-1}\left(\sqrt{\frac{1 - \left(\frac{n_1}{n_2}\right)^2}{sin^2(\theta)} - 1}\right) \tag{A.2}$$

$$\text{TM mode:} \qquad \varphi_{21} = tan^{-1}\left(\left(\frac{n_1}{n_2}\right)^2 \sqrt{\frac{1 - \left(\frac{n_1}{n_2}\right)^2}{sin^2(\theta)} - 1}\right) \tag{A.3}$$

Equation A.1 is the modal equation for slab waveguide configuration. Each guided mode for a given waveguide structure and wavelength propagates at a specific angle (θ), known as effective refractive index that defined as: $n_{eff} = n_2 \cos\theta$

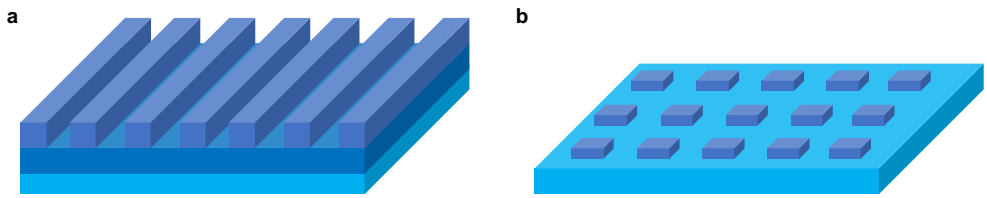

Figure A.2: DFB structures. (a) One-dimensional. (b) Two-dimensional

For asymmetric slab waveguide ($n_1 > n_3$), then for a guided mode in the active medium $n_1 \leq n_{eff} \leq n_2$. Then, the critical condition for this specific slab waveguide ($n_1 > n_3$) structure is $n_{eff} = n_1$ at $\theta = \theta_c$. Below this value, the modal equation can be satisfied. This condition defines a cut-off thickness for asymmetric slab waveguide structure.

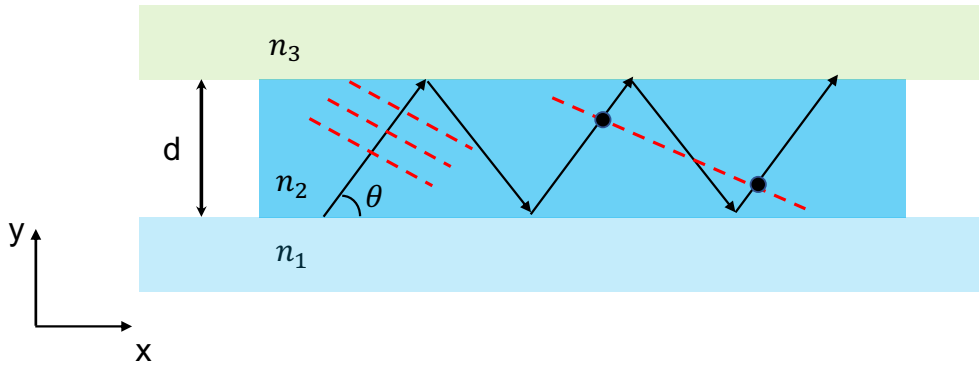

Figure A.3: Optical ray diagram in an asymmetric slab waveguide. The black arrows show the propagating rays with transverse wavefronts indicated by dashed red lines. θ is the angle of reflection from the interfaces respect to x-direction. d is thickness of the active medium of the waveguide

Thicker active layer can support a larger number of guided waveguide modes.

DFB lasers: A schematic of a typical DFB laser shown in Figure A.4, showing diffractive feedback along one axis of the waveguide. The laser structure consists of a CQD thin film deposited on top of patterned grating. Light propagates in the high refractive index medium (gain media), the waveguide mode is created by the scattered light from the periodic gratings (thin black arrows). Then, the scattered light from each grating combines coherently to generate Bragg-scattered waveguide mode in a new direction (thick black arrow). For a given grating period (Λ), the Bragg condition is satisfied for specific set of wavelengths, called as DFB feedback wavelength (λ_b) [132]:

$$2n_{eff}\Lambda = m\lambda_b \tag{A.4}$$

DFB Grating Fabrication: The gratings that we used in Chapter 3 were fabricated on pre-cleaned alumina (Ossila Ltd.) substrate in a cleanroom. The PMMA (AR-P 662.04 Allresist) was firstly spin-coated at 4000 r.p.m. for 60 s followed by baking at 150 °C for 2 min. Then, a layer of a conductive polymer (AR-PC 5090.02 Allresist) was spin-coated on top of PMMA layer within a spin speed of 2000 r.p.m., and then baked for 1 min at 90 °C. To pattern the sample, it was transferred to an electron-beam lithography system (Crestec CABL 9000C). Following the lithography, the conductive polymer layer was dissolved in water for 1 min and e-beam resist was developed for 2 min. For etching the alumina substrate, reactive-ion etching was used within 80 sccm

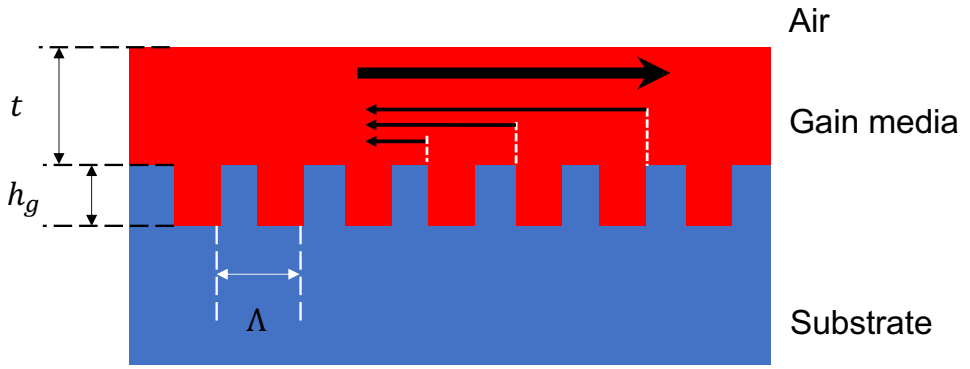

Figure A.4: Schematic representation of 2^{nd}-order one-dimensional DFB laser with a grating period of Λ and height of h_g. t defined as the thickness of gain media.

of Ar and 20 sccm of CHF3 under 290 V of an RF power for 5 min. Finally, the residual PMMA was then cleaned-off using an oxygen plasma asher and acetone/isopropanol solution cleaning.

A.4 Photovoltaic device fabrication

The PV devices were prepared on a pre-cleaned indium tin oxide (ITO) coated glass substrate. The electron-transporting layer (ZnO) was prepared by spin coating of ZnO NCs in chloroform (40 mg.mL^{-1}) on the substrate at a speed of 4000 r.p.m for 60 s. The thickness of this layer is about 40 nm. Then, the active layer of bare-PbS or PbS/ZnO binary blend was deposited on this layer. The active layer deposition follows the similar procedure as described above. In this case, the thickness of the active layer was 200–220 nm. Next, two layers of ethanedithiol-treated PbS (≈30–35 nm) were deposited on the active layer solid film, acting as the electron- blocking layer. Finally, the back-electrode was formed by deposition of ≈100 nm Au through a prepatterned mask in thermal evaporator (Nano 36 Kurt J. Lesker). The active area of each device is 3.14 mm^2.

A.5 LED device fabrication

The LED device was fabricated on a pre- cleaned E-ITO substrate. The electron transport layer was made of ZnO NCs by spin-casting ZnO NCs in chloroform at a spin speed of 4000 r.p.m. for 60 s. The active medium was spun on top of the ZnO layer as described in the active layer deposition section. The hole transport layer was formed using PbS QDs of smaller diameter which was treated by a solution of 0.02% ethanedithiol in acetonitrile. The graphene layer was transferred in a way mentioned

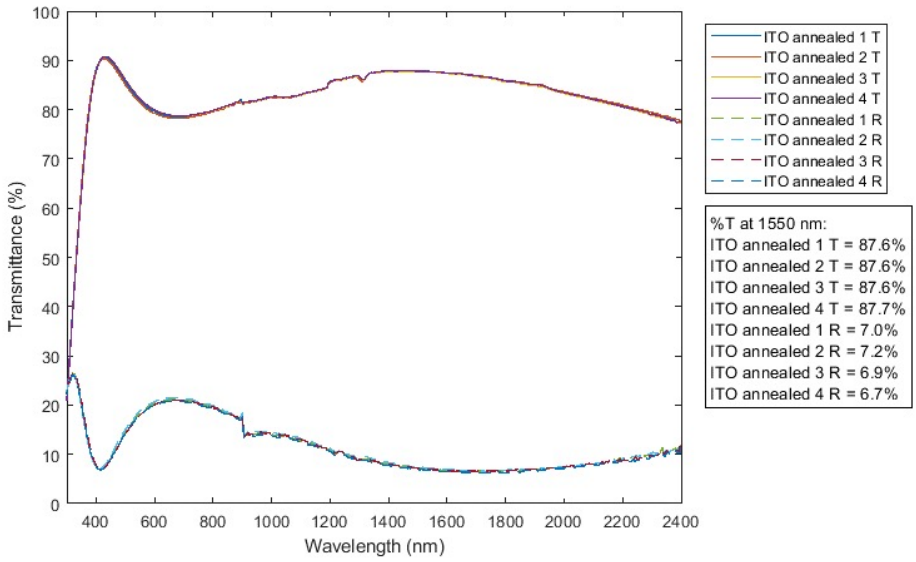

Figure A.5: Transmission of engineered-indium tin oxide (E-ITO) coated glass substrate.

above. To prevent from scratching the graphene layer, we deposited approximately 50 nm Au through a pre-patterned mask in thermal evaporator (Nano 36 Kurt J. Lesker).

A.6 Engineered ITO thin film preparation

Engineered-Indium Tin Oxide (E-ITO)-Coated Glass Substrate Preparation: The E-ITO is made by low-temperature annealing (LTA) of as-deposited ITO based on the method explained in our previous work [133]. ITO films of 100 nm were deposited by the University of Stuttgart on fused silica substrates via sputtering at room temperature. In the LTA process, the as-deposited ITO is annealed on a hotplate at 350 °C for 3 h, in the ambient atmosphere. The measured transmission and reflection of our E-ITO substrate is shown in Figure A.5.

A.7 Graphene layer transfer

CVD-grown monolayer graphene on copper with polymethyl methacrylate (PMMA) on top (purchased from Graphenea S.A) was cut to match the sample dimensions. The copper was etched in an ammonium persulfate solution in deionized water (3 g.mL^{-1}) for 3 h. The remaining PMMA/graphene sheet is further cleaned in deionized water

and transferred onto the sample. The sample with the graphene/PMMA layer is dried overnight in vacuum. PMMA is removed with acetone and isopropanol to obtain the graphene layer on top of our devices.

B

Experimental methods: Device characterizations

B.1 Steady-state absorption spectroscopy

In this thesis, we used steady-state absorption spectroscopy to understand the optical properties of our nanocrystals and solid films. Figure B.1 depicts a schematic of the setup for steady-state absorption measurements. To measure the absorption spectrum, a broad band white light source of an incandescent Tungsten is directed into a monochromator to generate the excitation wavelengths. The generated light excites the sample and PbSmart NIR detector measures the transmission intensity of the corresponding excitation wavelength. We used Cary-5000 (UV-VIS-NIR) as the absosrption spectrometer. The change in the optical intensity is attributed to the absorption and the reflection of the sample. Then, the measured transmission is $T(\lambda) = \frac{I_1(\lambda)}{I_0(\lambda)}$, here $I_0(\lambda)$ and $I_1(\lambda)$ are the incident and detected light intensity. To extract the absorption of our devices, the reflection measured by the spectrophotometer which was equipped with a diffuse reflectance accessory (DRA) module. $A(\lambda) = 1 - T(\lambda) - R(\lambda)$.

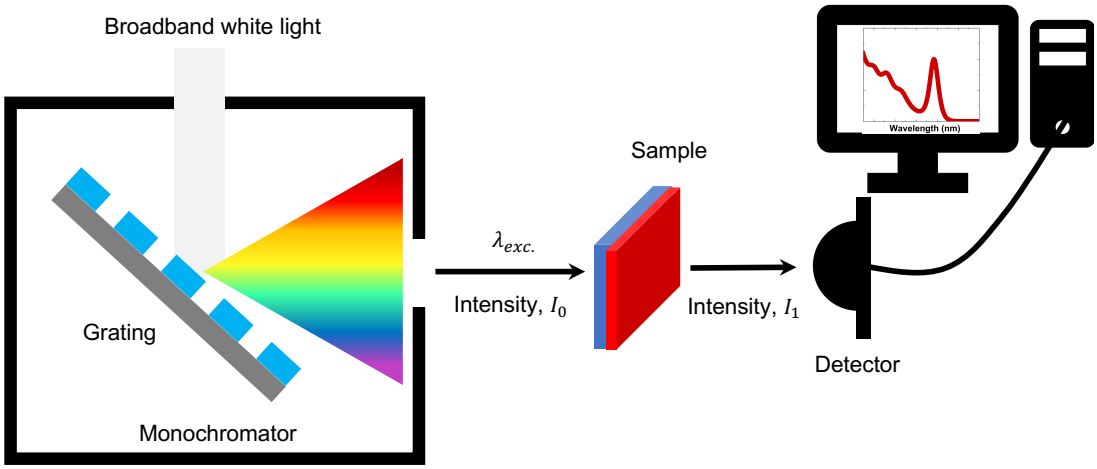

Figure B.1: Schematic diagram of the experimental setup for steady-state absorption spectroscopy. Insets shows absorption spectrum of PbS CQDs as an exemplary case.

B.2 Time-resolved photoluminescence (TRPL) spectroscopy

In this thesis, we employed TRPL spectroscopy to understand the dynamics of our devices at low population number of excitons ($\langle N \rangle \ll 1$). This technique allows us to find out the recombination mechanisms in our devices, such as the competition between radiative and nonradiative channels. To do so, the measurements were performed using a Horiba Jobin Yvon iHR550 Fluorolog system coupled with a Hamamatsu RS5509-73 liquid-nitrogen cooled photomultiplier tube and a calibrated Spectralon-coated Quanta-phi integrating sphere. A 637 nm continuous wave laser (Vortran Stradus) was used as the excitation source for steady-state PL measurements. The time-resolved measurements were performed using a pulsed light source (SpectraLED-S625) at 625 nm. For extracting intrinsic PL decay curves, the recorded decays were corrected by taking IRF of system into account.

B.3 Transient absorption spectroscopy

Using TA allows us to understand the ultrafast photophysical properties of our devices which cannot be monitored via TRPL including Auger recombination and optical gain lifetime. Particularly, TA measurements provide useful information about the stimulated emission. Basically, TA technique, also known as pump-probe spectroscopy, measures the pump-induced absorption change [134]. Figure B.2 shows the working principle of TA, where the optically modulated pump beam excites the sample and

every probe beam measures the absorption spectrum after a certain time delay (Figure B.2a). Therefore, the wavelength- and time-dependent differential absorption spectrum (ΔA) of pump-on and pump-off state for probe can be written as:

$$\Delta A(\lambda, t) = -\log\left(\frac{I_{on}(\lambda, t)}{I_{off}(\lambda, t)}\right) \tag{B.1}$$

Figure B.2b shows the sample ΔA at a time delay of τ_D with respect to the wavelength, while Figure B.2c plots the changes of absorption as a function time delay at a specific wavelength. Figure B.3 represents a schematic diagram of pump-probe TA, in which the output of Ti:Sapphire laser is split into two for generating the pump and probe beams separately. For generating the probe signal, the laser beam excites a nonlinear crystal, which produces the broadband white light in the visible and near IR (NIR) region. Note, different crystals are required to generate the light in different spectral windows. An optical parametric amplifier (OPA) is used for creating tunable pump beam ranging from the UV to mid-IR. The pump beam is generated through parametric nonlinear optical interactions including second- and third- harmonic generation, as well as sum- and difference- frequency generation. An optical chopper is introduced in the path to periodically block the successive pump beam pulses. As a consequence, the repetition rate of the pump beam becomes half of the probe. It is necessary to mention that above a certain wavelength ($\backsim$ 1600 nm), the probe beam must be generated through another OPA system. As can be seen, the pump beam enters to a delay line where the time delay (τ_D) between the pump and probe beam is created by changing the position of the mirrors. Finally, both beams are spatially overlapped onto the sample, where only the probe beam enters to the spectrometer. Then, the grating scatters the incoming light and a charge-coupled device (CCD) array detects the signal.

TA measurements: Our TA measurements were performed using a mode-lock Ti-sapphire oscillator based regenerative amplifier having a center wavelength of 800 nm and pulse width of 45 fs at a repetition rate of 1 kHz. The optical setup for the measurements was a typical pump-probe non-collinear configuration. The output of the amplifier was directed into a half-wave plate and a variable neutral density to adjust the pump fluence on the samples. The probe beam (wavelengths ranging from 1200 to 1700 nm) was generated by an optical parametric amplifier within almost 1 mJ at 800 nm. A precise motorized stage was used to control the time delay between the pump and probe beam. The probe beam was directed at the samples within the same

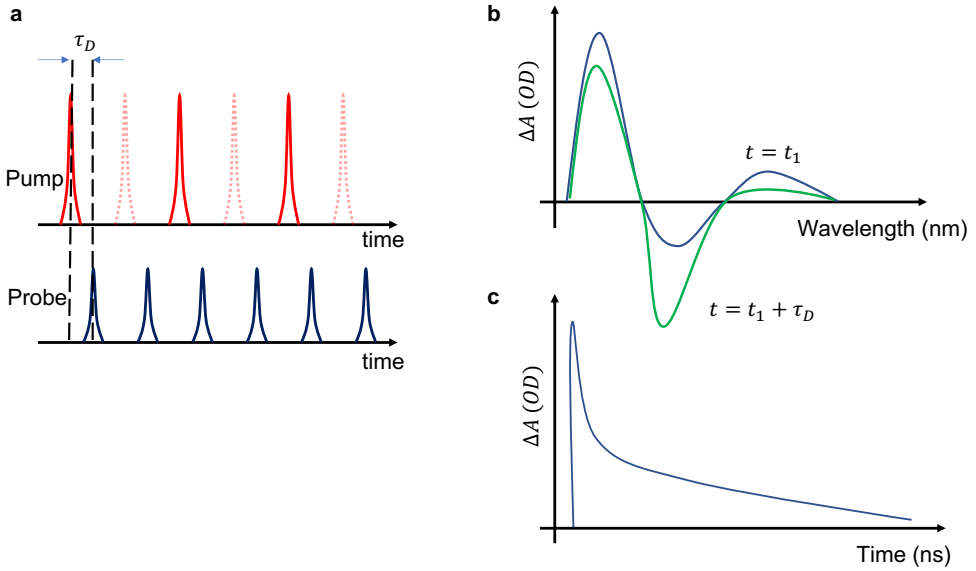

Figure B.2: Schematic representation of TA technique. (a) Pump and probe beam, where τ_D is defined as time delay between pump and probe beam. (b) Example of the change in absorption as a function of wavelength at a specific time delay. (c) Kinetic trace of ΔA at a given wavelength.

excitation area of the pump. The changes in reflection and transmission signals were recorded by a lock-in amplifier. All measurements were carried out at room temperature in solid film formation of CQDs on a glass substrate. The solid films were prepared by the procedure described in active layer deposition on a glass substrate (see Appendix A.2)

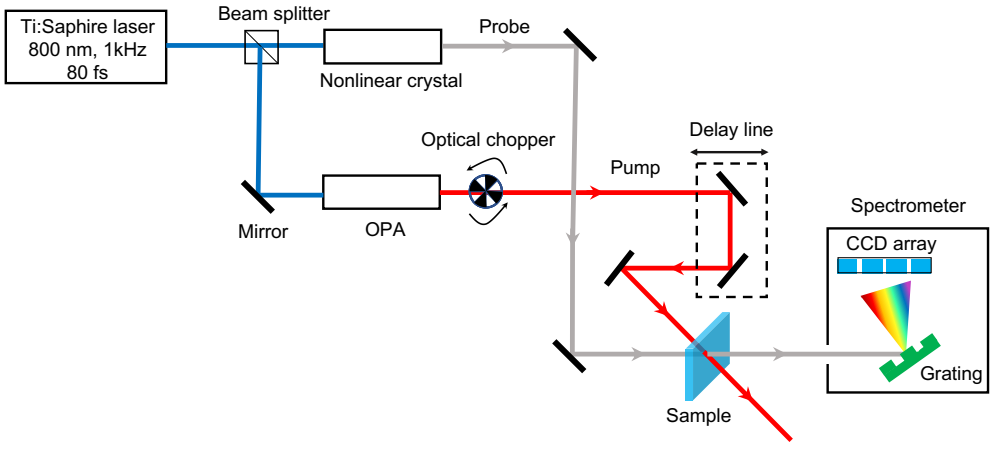

Figure B.3: Schematic diagram of pump-probe setup.

Calculating the averaged number of excitons per CQD. We used the following equation to calculate the average number of excitons per dot:

$$\langle N_{abs} \rangle = \frac{E_i(I_0 - I_t - I_r)}{ATF} V \tag{B.2}$$

Where, $\langle N_{abs} \rangle$ is the averaged-number of exciton per CQD in the solid film. E_i denotes as the generated number of excitons at the excitation wavelength (800 nm for TA measurements). I_0, I_t, I_r are the intensities of the incident, transmitted and reflected of the pump beam, which were monitored during the experiment. A is the excitation area, T is the thickness of the thin films (measured by SEM and profilometry) and F is the filling factor of the film (which is 0.74 for bare-PbS film, and 0.52 for PbS/ZnO blend having 30% ZnO loading). V denotes the volume of one CQD-emitter.

Extracting multiexcitonic kinetics: Figure B.4 shows an exemplary case of the measured TA for bare-PbS and PbS/ZnO blend (having 30% ZnO loading) samples as a function of the absorbed number of excitons per QD (at the excitation wavelength (800 nm)) at the first excitonic peak position. As described by Klimov et al. [77], to extract the multiexcitonic dynamics. First, all TA decays should be normalized to the long-term decay values (shown in Figure B.4). Then, subtraction of the multiexciton traces from the single-exciton trace yields the pure multiexciton dynamics. The extracted new decay was fitted within a mono-exponential function. For instance, to extract the bi-exciton Auger decay in both cases, the trace of $N \ll 1$ was subtracted from the traces at $\langle N \rangle \approx 0.4$. This procedure was also applied to extract the dynamics of CQDs states with 3- and 4- excitons. In addition to extracting ultrafast kinetics of the CQDs, using TA provides us useful information about the stimulated emission including optical gain spectrum and net gain threshold.

B.4 Optical gain and lasing characterizations

Optical gain measurements are necessary to characterize gain materials. In this thesis, we employed various techniques including amplified spontaneous emission (ASE) measurements, net modal gain calculation via variable stripe length (VSL) method, and waveguide loss coefficient.

ASE basic: ASE is the superluminscence of a luminescent material, in which spontaneous emission is optically amplified by the stimulated emission. Commonly, ASE is

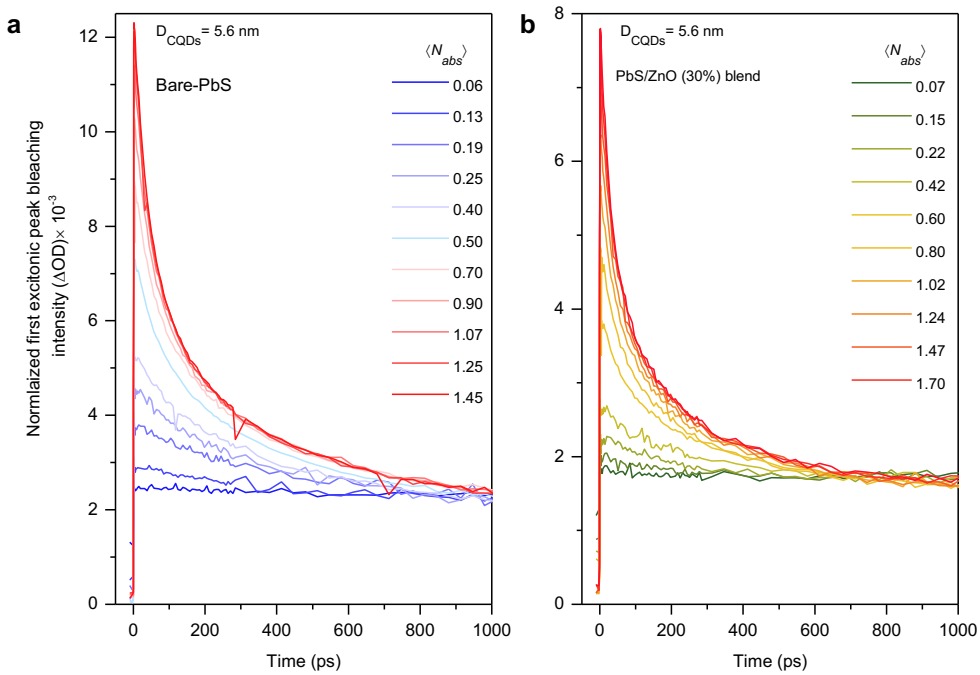

Figure B.4: Normalized bleaching intensity of first excitonic peak ($1S_e$–$1S_h$ transition) for PbS CQDs having a diameter of 5.6 nm. Bare-PbS QDs (a) and Pbs/ZnO blend having 30% ZnO loading (b).

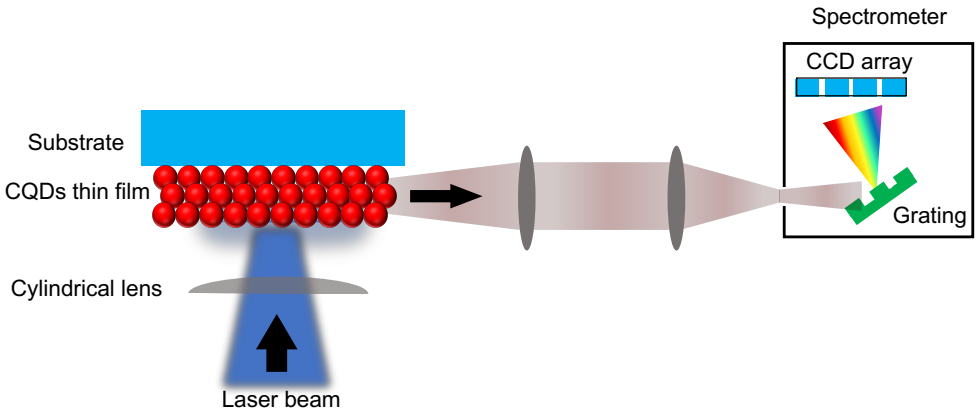

Figure B.5: Experimental configuration for ASE measurements. The laser beam is focused on the sample through a cylindrical lens. The ASE signal is collected perpendicular to the excitation direction through open space optic which is directed to a spectrometer.

observed in the solid films of any gain material. Particularly, the solid film of solution-processed materials such as CQDs or organic semiconductors are fabricated via spin-coating or drop-casting techniques. We previously explained the sample preparation process that we used in this thesis (Appendix A.2). Basically, ASE can be considered as a cavity-free lasing action, where the solid film acts as a waveguide for propagation the stimulated emission along the sample. We discussed the basics of the waveguides in section A.3, typically the devices for ASE measurements consist of an active layer on top of the substrate, where the light is collected perpendicular to the excitation direction. Note, the stripe excitation beam is commonly used for ASE characterizations. Figure B.5 shows a schematic of the ASE setup.

ASE measurements: In this thesis, the samples were optically excited by a femtosecond (300 fs) Yt:YAG ORAGAMI laser (NKT photonics) operating at a wavelength of 1030 nm and a repetition rate of 10 kHz. A variable neutral density is used for adjusting the pumping intensity. The laser focused through a cylindrical lens on the surface of the sample. The ASE spectra were collected perpendicular to the excitation axis by using a lens with a focal length of 50 mm having a diameter of 2 inches. Employing free-space optics, the collected ASE signal was coupled into a Kymera 328i spectrograph (Oxford instrument Andor) which was equipwithd by an 1D-InGaAs camera via a lens having a focal length of 200 mm through a 100 μm slit.

Lasing measurements: Lasing spectra were recorded perpendicular to the surface of the devices $\backsim$20 cm away from the CQD-DFB laser device. In doing so, a fiber-coupled port of the spectrometer was used having a slit width of 10-20 μm to achieve high resolution. The integration time for all measurements is set to 3 s. A long pass filter was located in front of the device for all measurements. The infrared picture and video of the CQD/DFB laser were taken by an NIT-WiDy-SenS-320V-ST InGaAs camera with an attached SWIR lens.

Variable stripe length: In this thesis, we measured the modal gain coefficient of our devices via the VSL technique. Figure B.7 shows the schematic representationthe of VSL experimental setup [135]. A We used similar setup to ASE measurements, in which the length of the stripe is adjusted by a slit. The width of the excitation beam was set to $\backsim$120 μm to ensure the 1D amplification assumption and to maximize the ASE intensity at the edge of sample. The slit was placed close enough to the sample for reducing the diffraction effects in the measurements. To fit VSL data, we used the following expression [135]:

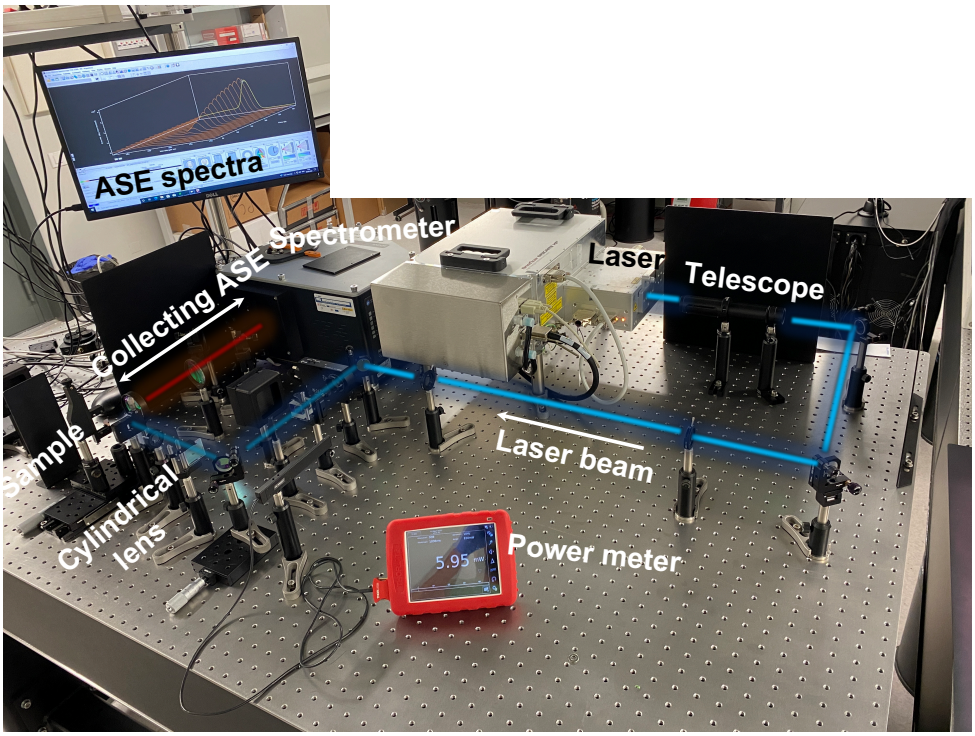

Figure B.6: Experimental setup for ASE measurements.

$$I_{VSL} = I_0(e^{g(g,\lambda)} - 1) \tag{B.3}$$

Waveguide loss coefficient: Similar to VSL measurements, we measured the optical loss coefficient. A narrow stripe excitation is used, in which the size of stripe is translated on top of the sample via a translation stage. The distance between the edge of the sample and unexcited part of the film is varied. Therefore, the waveguide loss coefficient can be calculated from: $I(\lambda, l) = I_0 e^{-\alpha(\lambda,l)}$.

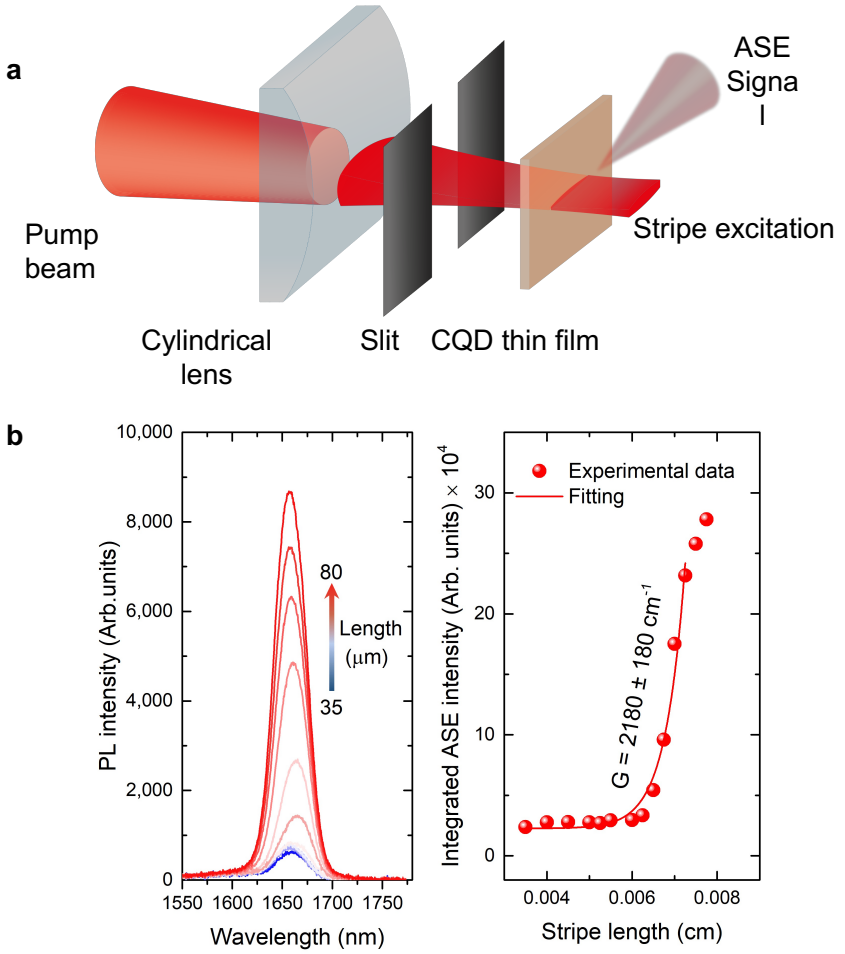

Figure B.7: (a) Schematic representation of VSL measurements. (b) Exemplary VSL data for PbS/PbSSe core/shell CQD thin film at 2000 μJ.cm^{-2}.

B.5 Thermal admittance spectroscopy

In this thesis, we employed TAS to analyze in-gap trap states similar to the method introduced in [95]. To do so, we have characterized the capacitance of the PV devices which represents the imaginary part of the admittance. The capacitance was recorded as a function of frequency at a specific temperature (Figure B.8). Then, the resonance frequency (f_0) at a particular temperature (T) can be defined as following:

$$f_0 = 2\xi_0 T^2 exp\left(\frac{-E_A}{k_b T}\right) \tag{B.4}$$

Where, ξ_0 is defined as trap escape frequency, E_A is the trap-states activation energy, and k_b is Boltzman's constant. Therefore, the distribution of the trap states (N_t) can be evaluated by the following equation:

$$N_t(E_f) = \frac{-v_{bi}^2}{AW_D[qv_{bi} - (E_{f\infty} - E_f)]} \frac{dc}{df} \frac{f}{k_b T} \tag{B.5}$$

Herein, the built-in potential (V_{bi}) and the depletion width (W_D) of the devices were extracted from Mott-Schottky measurement. A is the device area, $E_{f\infty}$ noted as bulk fermi level of the active material. By re-arranging Equation B.4, E_f can be defined as:

$$k_b T ln(\frac{2\xi_0 T^2}{f}) \tag{B.6}$$

Figure B.8 and B.9 show the C and $(-fdc/df)$ as a function of frequency (f) varying temperature, respectively. To calculate the activation energy of the trap-states (E_A), the resonance frequency (f_0) was taken the peak value of $(-fdc/df)$ (Figure **??**). Furthermore, the calculated N_t using Equation B.6 depicted as a function of E_t (the position of trap-states with respect to the band-edge) in Figure 3.2.

B.6 Electromagnetic simulation

Lumerical FDTD Simulation: Commercial software, Ansys Lumerical Finite Difference Time Domain (FDTD), is used for full electromagnetic simulations. A thin (16 nm) PbS layer is placed on top of a semi- infinite SiO2 substrate ($z \leq 0$). Clusters of spherical ZnO particles are randomly distributed inside the PbS layer. The fundamental mode is calculated and injected toward x direction by the built-in mode source. The fields

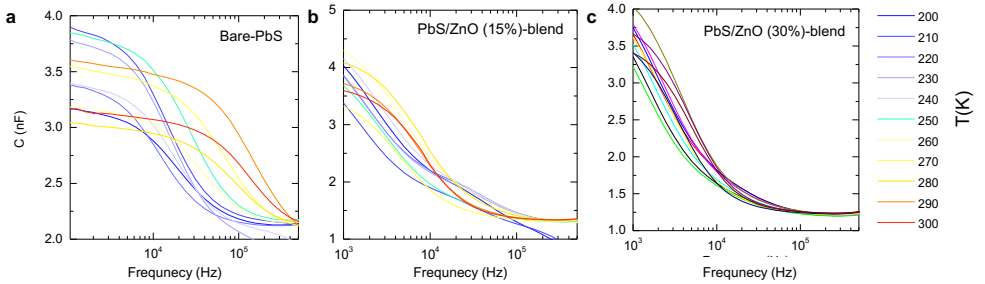

Figure B.8: Frequency-dependent capacitance plot as a function of temperature for (a) Bare-PbS, (b) PbS/ZnO (15%)-blend and (c) PbS/ZnO (30%)-blend.

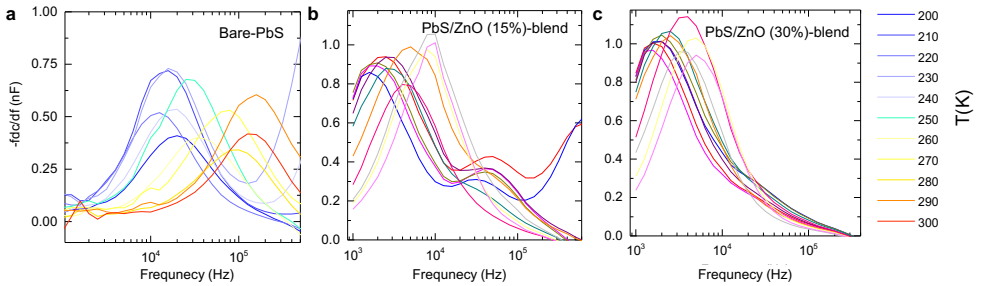

Figure B.9: Frequency-dependent capacitance plot as a function of temperature for (a) Bare-PbS, (b) PbS/ZnO (15%)-blend and (c) PbS/ZnO (30%)-blend.

are recorded by frequency-domain field and power monitors. Perfectly matched layers (PML) boundary conditions are used at $\pm x$ and $\pm z$ boundaries, and periodic boundary conditions are used at $\pm y$ boundaries.

B.7 X-ray photoelectron spectroscopy

The samples for XPS were prepared on glass substrate following the same spin coating procedure used for the fabrication of the devices. XPS measurements were performed at the Institut Català de Nanociencia i Nanotecnologia (ICN2) using a Phoibos 150 analyser (SPECS) under ultra-high vacuum conditions (base pressure of 4×10^{-10} mbar) equipped with a monochromatic $AlK\alpha$ X-ray source (1486.74 eV). The pass energy value used was 20 eV for the high-resolution spectrum. The spectra of S2s and Se3d were fitted with a curve that has the line-shape obtained from the product of a Gaussian and a Lorentzian (70% Gaussian, 30% Lorentzian), while Pb4f was fitted using a Lorentzian asymmetric line-shape.

Bibliography

[1] A. Mekis, "Lighting up the chip," *Nature Photonics*, vol. 2, no. 7, pp. 389–390, 2008. (see p. 1)

[2] S. Pimputkar, J. S. Speck, S. P. Denbaars, and S. Nakamura, "Prospects for LED lighting," *Nature Photonics*, vol. 3, no. 4, pp. 180–182, 2009. (see p. 1)

[3] G. Favraud, J. S. T. Gongora, and A. Fratalocchi, "Evolutionary Photonics for Renewable Energy, Nanomedicine, and Advanced Material Engineering," *Laser and Photonics Reviews*, vol. 12, no. 11, pp. 1–24, 2018. (see p. 1)

[4] B. Javidi, J. Sola-Pikabea, and M. Martinez-Corral, "Breakthroughs in photonics 2014: Recent advances in 3-D integral imaging sensing and display," *IEEE Photonics Journal*, vol. 7, no. 3, pp. 1–7, 2015. (see p. 1)

[5] D. Conteduca, "Photonic Biosensors: Detection, Analysis and Medical Diagnostics," *Biosensors*, vol. 12, no. 4, pp. 10–12, 2022. (see p. 1)

[6] H. K. Lo, M. Curty, and K. Tamaki, "Secure quantum key distribution," *Nature Photonics*, vol. 8, no. 8, pp. 595–604, 2014. (see p. 1)

[7] I. S. Amiri, S. R. B. Azzuhri, M. A. Jalil, H. M. Hairi, J. Ali, M. Bunruangses, and P. Yupapin, "Introduction to photonics: Principles and the most recent applications of microstructures," *Micromachines*, vol. 9, no. 9, 2018. (see p. 1)

[8] W. A. Zortman, D. C. Trotter, and M. R. Watts, "Silicon photonics manufacturing," *Optics Express*, vol. 18, no. 23, p. 23598, 2010. (see pp. 1 and 2)

[9] T. Sharma, J. Wang, B. K. Kaushik, Z. Cheng, R. Kumar, Z. Wei, and X. Li, "Review of recent progress on silicon nitride-based photonic integrated circuits," *IEEE Access*, vol. 8, pp. 195436–195446, 2020. (see p. 2)

[10] M. A. Albota, B. F. Aull, D. G. Fouche, R. M. Heinrichs, D. G. Kocher, R. M. Marino, J. G. Mooney, N. R. Newbury, M. E. O. Brien, B. E. Player, B. C.

Willard, and J. J. Zayhowski, "Three-Dimensional Imaging Laser Radars with Geiger-Mode Avalanche Photodiode Arrays," no. October, 2014. (see p. 2)

[11] Y. Ceylan, S. Hizmetli, and Y. Silig, "The effects of infrared laser and medical treatments on pain and serotonin degradation products in patients with myofascial pain syndrome . A controlled trial," pp. 260–263, 2004. (see p. 2)

[12] S. J. Pittman, B. Costa, and L. M. Wedding, "LiDAR Applications," pp. 145–174, 2013. (see p. 2)

[13] A. Layer and C. Epitaxy, "Epitaxial growth of iii-v compound semiconductor thin films and their device applications," vol. 23, pp. 73–126, 1992. (see p. 2)

[14] B. J. Ainslie, "A Review of the Fabrication and Properties of Erbium-Doped Fibers for Optical Amplifiers," vol. 9, no. 2, pp. 220–227, 1991. (see p. 2)

[15] C. B. Murray, D. J. Norris, and M. G. Bawendi, "Synthesis and Characterization of Nearly Monodisperse CdE (E = S, Se, Te) Semiconductor Nanocrystallites," *Journal of the American Chemical Society*, vol. 115, no. 19, pp. 8706–8715, 1993. (see pp. 5 and 6)

[16] A. P. Alivisatos, "Perspectives on the physical chemistry of semiconductor nanocrystals," *Journal of Physical Chemistry*, vol. 100, no. 31, pp. 13226–13239, 1996. (see pp. 5 and 6)

[17] A. Alivisatos, "Semiconductor clusters, nanocrystals and quantum dots," *Science*, vol. 271, no. December, pp. 933–937, 1996. (see p. 6)

[18] J. M. Pietryga, Y. S. Park, J. Lim, A. F. Fidler, W. K. Bae, S. Brovelli, and V. I. Klimov, "Spectroscopic and device aspects of nanocrystal quantum dots," *Chemical Reviews*, vol. 116, no. 18, pp. 10513–10622, 2016. (see pp. 6, 8, 9, and 32)

[19] David Jiles, *Introduction to the Electronic Properties of Materials*. Springer, 1 ed., 1994. (see p. 6)

[20] H. Jones, *Introduction to Solid State Physics by C. Kittel* . John Wiley and Sons Inc, 8 ed., 2005. (see p. 6)

[21] V. I. Klimov, *Nanocrystal Quantum Dots*. CRC Press, 2010. (see pp. 7, 17, and 32)

[22] I. Moreels, K. Lambert, D. Smeets, D. De Muynck, T. Nollet, J. C. Martins, F. Vanhaecke, A. Vantomme, C. Delerue, G. Allan, and Z. Hens, "Size-dependent

optical properties of colloidal PbS quantum dots," *ACS Nano*, vol. 3, no. 10, pp. 3023–3030, 2009. (see p. 9)

[23] G. Konstantatos and E. H. Sargent, *Colloidal Quantum Dot Optoelectronics and Photovoltaics*. Cambridge University Press, 2013. (see pp. 9 and 23)

[24] G. Allan and C. Delerue, "Confinement effects in PbSe quantum wells and nanocrystals," *Physical Review B - Condensed Matter and Materials Physics*, vol. 70, no. 24, pp. 1–9, 2004. (see p. 9)

[25] I. Kang and F. W. Wise, "Electronic structure and optical properties of PbS and PbSe quantum dots," *Journal of the Optical Society of America B*, vol. 14, no. 7, p. 1632, 1997. (see pp. 9 and 56)

[26] R. D. Schaller, M. A. Petruska, and V. I. Klimov, "Tunable Near-Infrared Optical Gain and Amplified Spontaneous Emission Using PbSe Nanocrystals," *Journal of Physical Chemistry B*, vol. 107, no. 50, pp. 13765–13768, 2003. (see pp. 9, 15, and 32)

[27] G. Nootz, L. A. Padilha, P. D. Olszak, S. Webster, D. J. Hagan, E. W. Van Stryland, L. Levina, V. Sukhovatkin, L. Brzozowski, and E. H. Sargent, "Role of symmetry breaking on the optical transitions in lead-salt quantum dots," *Nano Letters*, vol. 10, no. 9, pp. 3577–3582, 2010. (see p. 10)

[28] N. Taghipour, G. L. Whitworth, A. Othonos, M. Dalmases, S. Pradhan, Y. Wang, G. Kumar, and G. Konstantatos, "Low-Threshold, Highly Stable Colloidal Quantum Dot Short-Wave Infrared Laser enabled by Suppression of Trap-Assisted Auger Recombination," *Advanced Materials*, vol. 34, no. 3, pp. 1–8, 2022. (see pp. 11, 15, 18, 48, 63, and 70)

[29] S. Christodoulou, I. Ramiro, A. Othonos, A. Figueroba, M. Dalmases, O. Özdemir, S. Pradhan, G. Itskos, and G. Konstantatos, "Single-Exciton Gain and Stimulated Emission across the Infrared Telecom Band from Robust Heavily Doped PbS Colloidal Quantum Dots," *Nano Letters*, vol. 20, no. 8, pp. 5909–5915, 2020. (see pp. 11, 15, 17, 24, 32, 33, 48, 59, 63, and 70)

[30] N. Taghipour, I. Tanriover, M. Dalmases, G. L. Whitworth, C. Graham, A. Saha, O. Özdemir, B. Kundu, V. Pruneri, K. Aydin, and G. Konstantatos, "Ultra-Thin Infrared Optical Gain Medium and Optically-Pumped Stimulated Emission in PbS Colloidal Quantum Dot LEDs," *Advanced Functional Materials*, vol. 2200832, pp. 1–7, 2022. (see pp. 11 and 15)

[31] Y. S. Park, J. Roh, B. T. Diroll, R. D. Schaller, and V. I. Klimov, "Colloidal quantum dot lasers," *Nature Reviews Materials*, vol. 6, no. 5, pp. 382–401, 2021. (see pp. 15, 18, 21, and 32)

[32] H. Jung, N. Ahn, and V. I. Klimov, "Prospects and challenges of colloidal quantum dot laser diodes," *Nature Photonics*, vol. 15, no. 9, pp. 643–655, 2021. (see pp. 15, 32, and 70)

[33] S. Delikanli, F. Isik, F. Shabani, H. D. Baruj, N. Taghipour, and H. V. Demir, "Ultralow Threshold Optical Gain Enabled by Quantum Rings of Inverted Type-I CdS/CdSe Core/Crown Nanoplatelets in the Blue," *Advanced Optical Materials*, vol. 9, no. 8, pp. 1–6, 2021. (see p. 15)

[34] B. Guzelturk, Y. Kelestemur, K. Gungor, A. Yeltik, M. Z. Akgul, Y. Wang, R. Chen, C. Dang, H. Sun, and H. V. Demir, "Stable and low-threshold optical gain in CdSe/CdS quantum dots: An all-colloidal frequency up-converted laser," *Advanced Materials*, vol. 27, no. 17, pp. 2741–2746, 2015. (see pp. 15, 20, 29, 48, and 51)

[35] F. Fan, O. Voznyy, R. P. Sabatini, K. T. Bicanic, M. M. Adachi, J. R. McBride, K. R. Reid, Y. S. Park, X. Li, A. Jain, R. Quintero-Bermudez, M. Saravanapavanantham, M. Liu, M. Korkusinski, P. Hawrylak, V. I. Klimov, S. J. Rosenthal, S. Hoogland, and E. H. Sargent, "Continuous-wave lasing in colloidal quantum dot solids enabled by facet-selective epitaxy," *Nature*, vol. 544, no. 7648, pp. 75–79, 2017. (see pp. 15, 29, and 48)

[36] N. Taghipour, S. Delikanli, S. Shendre, M. Sak, M. Li, F. Isik, I. Tanriover, B. Guzelturk, T. C. Sum, and H. V. Demir, "Sub-single exciton optical gain threshold in colloidal semiconductor quantum wells with gradient alloy shelling," *Nature Communications*, vol. 11, no. 1, pp. 1–8, 2020. (see pp. 15, 18, 21, 22, 32, 39, 48, 49, 62, and 63)

[37] O. V. Kozlov, Y.-s. Park, J. Roh, I. Fedin, T. Nakotte, and V. I. Klimov, "Sub–single-exciton lasing using charged quantum dots coupled to a distributed feedback cavity to a Distributed Feedback Cavity," *Science*, vol. 675, no. August, pp. 672–675, 2019. (see pp. 15, 22, 29, 32, 48, and 85)

[38] Z. Yang, M. Pelton, I. Fedin, D. V. Talapin, and E. Waks, "A room temperature continuous-wave nanolaser using colloidal quantum wells," *Nature Communications*, vol. 8, no. 1, 2017. (see pp. 15 and 21)

[39] S. Yakunin, L. Protesescu, F. Krieg, M. I. Bodnarchuk, G. Nedelcu, M. Humer, G. De Luca, M. Fiebig, W. Heiss, and M. V. Kovalenko, "Low-threshold amplified

spontaneous emission and lasing from colloidal nanocrystals of caesium lead halide perovskites," *Nature Communications*, vol. 6, pp. 1–8, 2015. (see pp. 15 and 21)

[40] V. I. Klimov, A. A. Mikhailovsky, S. XU, A. Malko, J. A. Hollingsworth, and C. Leatherdale, "Optical Gain and Stimulated in Nanocrystal Emission Quantum Dots," vol. 290, no. 5490, pp. 314–317, 2000. (see pp. 15, 17, and 18)

[41] M. Saba, S. Minniberger, F. Quochi, J. Roither, M. Marceddu, A. Gocalinska, M. V. Kovalenko, D. V. Talapin, W. Heiss, A. Mura, and G. Bongiovanni, "Exciton-exciton interaction and optical cain in colloidal CdSe/CdS Dot/Rod nanocrystals," *Advanced Materials*, vol. 21, no. 48, pp. 4942–4946, 2009. (see pp. 15, 18, 21, 22, and 48)

[42] K. Wu, Y. S. Park, J. Lim, and V. I. Klimov, "Towards zero-threshold optical gain using charged semiconductor quantum dots," *Nature Nanotechnology*, vol. 12, no. 12, pp. 1140–1147, 2017. (see pp. 15, 16, 17, 22, 23, 32, 39, 48, 49, 62, and 85)

[43] C. Dang, J. Lee, C. Breen, J. S. Steckel, S. Coe-Sullivan, and A. Nurmikko, "Red, green and blue lasing enabled by single-exciton gain in colloidal quantum dot films," *Nature Nanotechnology*, vol. 7, no. 5, pp. 335–339, 2012. (see pp. 15, 22, 29, 39, 48, 62, and 63)

[44] G. L. Whitworth, M. Dalmases, N. Taghipour, and G. Konstantatos, "Solution-processed PbS quantum dot infrared laser with room-temperature tunable emission in the optical telecommunications window," *Nature Photonics*, vol. 15, no. 10, pp. 738–742, 2021. (see pp. 15, 29, 32, 33, 42, 48, 63, and 70)

[45] C. Liao, L. Tang, L. Wang, Y. Li, J. Xu, and Y. Jia, "Low-threshold near-infrared lasing at room temperature using low-toxicity Ag2Se quantum dots," *Nanoscale*, vol. 12, no. 42, pp. 21879–21884, 2020. (see pp. 15, 39, 48, and 70)

[46] M. Asada, Y. Miyamoto, and Y. Suematsu, "Gain and the Threshold of Three-Dimensional Quantum-Box Lasers," *IEEE Journal of Quantum Electronics*, vol. 22, no. 9, pp. 1915–1921, 1986. (see pp. 15 and 64)

[47] Y. Arakawa and H. Sakaki, "Multidimensional quantum well laser and temperature dependence of its threshold current," *Applied Physics Letters*, vol. 40, no. 11, pp. 939–941, 1982. (see p. 15)

[48] N. Taghipour, M. Dalmases, G. L. Whitworth, M. Dosil, A. Othonos, S. Christodoulou, S. M. Liga, and G. Konstantatos, "Colloidal Quantum Dot Infrared Lasers Featuring Sub-single-exciton Threshold and Very High Gain," *Advanced Materials*, vol. 2207678, p. 2207678, 2022. (see p. 17)

[49] I. Robel, R. Gresback, U. Kortshagen, R. D. Schaller, and V. I. Klimov, "Universal size-dependent trend in auger recombination in direct-gap and indirect-gap semiconductor nanocrystals," *Physical Review Letters*, vol. 102, no. 17, pp. 1–4, 2009. (see pp. 17 and 18)

[50] J. T. Stewart, L. A. Padilha, M. M. Qazilbash, J. M. Pietryga, A. G. Midgett, J. M. Luther, M. C. Beard, A. J. Nozik, and V. I. Klimov, "Comparison of carrier multiplication yields in PbS and PbSe nanocrystals: The role of competing energy-loss processes," *Nano Letters*, vol. 12, no. 2, pp. 622–628, 2012. (see pp. 17 and 18)

[51] L. W. Wang, M. Califano, A. Zunger, and A. Franceschetti, "Pseudopotential Theory of Auger Processes in CdSe Quantum Dots," *Physical Review Letters*, vol. 91, no. 5, pp. 1–4, 2003. (see p. 17)

[52] V. A. Kharchenko and M. Rosen, "Auger relaxation processes in semiconductor nanocrystals and quantum wells," *Journal of Luminescence*, vol. 70, no. 1-6 SPEC. ISS., pp. 158–169, 1996. (see p. 17)

[53] A. L. Efros and M. Rosen, "Random Telegraph Signal in the Photoluminescence Intensity of a Single Quantum Dot," *Physical Review Letters*, vol. 78, no. 6, pp. 1110–1113, 1996. (see p. 17)

[54] V. I. Klimov, J. A. McGuire, R. D. Schaller, and V. I. Rupasov, "Scaling of multiexciton lifetimes in semiconductor nanocrystals," *Physical Review B - Condensed Matter and Materials Physics*, vol. 77, no. 19, pp. 1–12, 2008. (see p. 18)

[55] C. She, I. Fedin, D. S. Dolzhnikov, P. D. Dahlberg, G. S. Engel, R. D. Schaller, and D. V. Talapin, "Red, Yellow, Green, and Blue Amplified Spontaneous Emission and Lasing Using Colloidal CdSe Nanoplatelets," *ACS Nano*, vol. 9, no. 10, pp. 9475–9485, 2015. (see pp. 18 and 48)

[56] Y. S. Park, W. K. Bae, T. Baker, J. Lim, and V. I. Klimov, "Effect of Auger Recombination on Lasing in Heterostructured Quantum Dots with Engineered Core/Shell Interfaces," *Nano Letters*, vol. 15, no. 11, pp. 7319–7328, 2015. (see pp. 18, 19, 20, 38, and 57)

[57] M. A. Hines and P. Guyot-Sionnest, "Synthesis and characterization of strongly luminescing ZnS-capped CdSe nanocrystals," *Journal of Physical Chemistry*, vol. 100, no. 2, pp. 468–471, 1996. (see p. 20)

[58] B. O. Dabbousi, J. Rodriguez-Viejo, F. V. Mikulec, J. R. Heine, H. Mattoussi, R. Ober, K. F. Jensen, and M. G. Bawendi, "(CdSe)ZnS core-shell quantum dots:

Synthesis and characterization of a size series of highly luminescent nanocrystallites," *Journal of Physical Chemistry B*, vol. 101, no. 46, pp. 9463–9475, 1997. (see p. 20)

[59] V. I. Klimov, S. A. Ivanov, J. Nanda, M. Achermann, I. Bezel, J. A. McGuire, and A. Piryatinski, "Single-exciton optical gain in semiconductor nanocrystals," *Nature*, vol. 447, no. 7143, pp. 441–446, 2007. (see pp. 20 and 22)

[60] Y. Chen, J. Vela, H. Htoon, J. L. Casson, D. J. Werder, D. A. Bussian, V. I. Klimov, and J. A. Hollingsworth, ""Giant" multishell CdSe nanocrystal quantum dots with suppressed blinking," *Journal of the American Chemical Society*, vol. 130, no. 15, pp. 5026–5027, 2008. (see p. 20)

[61] L. Wang, K. Nonaka, T. Okuhata, T. Katayama, and N. Tamai, "Quasi-Type II Carrier Distribution in CdSe/CdS Core/Shell Quantum Dots with Type i Band Alignment," *Journal of Physical Chemistry C*, vol. 122, no. 22, pp. 12038–12046, 2018. (see p. 20)

[62] F. García-Santamaría, Y. Chen, J. Vela, R. D. Schaller, J. A. Hollingsworth, and V. I. Klimov, "Suppressed auger recombination in "Giant" nanocrystals boosts optical gain performance," *Nano Letters*, vol. 9, no. 10, pp. 3482–3488, 2009. (see pp. 20, 21, 48, and 85)

[63] J. Cassidy, B. T. Diroll, N. Mondal, D. B. Berkinsky, K. Zhao, D. Harankahage, D. Porotnikov, R. Gately, D. Khon, A. Proppe, M. G. Bawendi, R. D. Schaller, A. V. Malko, and M. Zamkov, "Quantum Shells Boost the Optical Gain of Lasing Media," *ACS Nano*, vol. 16, no. 2, pp. 3017–3026, 2022. (see pp. 20 and 48)

[64] L. Zhang, C. Liao, B. Lv, X. Wang, M. Xiao, R. Xu, Y. Yuan, C. Lu, Y. Cui, and J. Zhang, "Single-Mode Lasing from "giant" CdSe/CdS Core-Shell Quantum Dots in Distributed Feedback Structures," *ACS Applied Materials and Interfaces*, vol. 9, no. 15, pp. 13293–13303, 2017. (see pp. 20, 48, and 85)

[65] Y. S. Park, W. K. Bae, L. A. Padilha, J. M. Pietryga, and V. I. Klimov, "Effect of the core/shell interface on auger recombination evaluated by single-quantum-dot spectroscopy," *Nano Letters*, vol. 14, no. 2, pp. 396–402, 2014. (see pp. 20, 21, and 48)

[66] R. Osovsky, D. Cheskis, V. Kloper, A. Sashchiuk, M. Kroner, and E. Lifshitz, "Continuous-wave pumping of multiexciton bands in the photoluminescence spectrum of a single CdTe-CdSe core-shell colloidal quantum dot," *Physical Review Letters*, vol. 102, no. 19, pp. 1–4, 2009. (see pp. 20 and 57)

[67] M. Nasilowski, P. Spinicelli, G. Patriarche, and B. Dubertret, "Gradient CdSe/CdS Quantum Dots with Room Temperature Biexciton Unity Quantum Yield," *Nano Letters*, vol. 15, no. 6, pp. 3953–3958, 2015. (see pp. 20 and 49)

[68] G. E. Cragg and A. L. Efros, "Suppression of auger processes in confined structures," *Nano Letters*, vol. 10, no. 1, pp. 313–317, 2010. (see pp. 21 and 57)

[69] C. She, I. Fedin, D. S. Dolzhnikov, A. Demortière, R. D. Schaller, M. Pelton, and D. V. Talapin, "Low-threshold stimulated emission using colloidal quantum wells," *Nano Letters*, vol. 14, no. 5, pp. 2772–2777, 2014. (see pp. 21 and 48)

[70] D. Dede, N. Taghipour, U. Quliyeva, M. Sak, Y. Kelestemur, K. Gungor, and H. V. Demir, "Highly Stable Multi-Crown Heterostructures of Type-II Nanoplatelets for Ultra-Low Threshold Optical Gain," *Chemistry of Materials*, vol. 31, p. acs.chemmater.9b00136, 2019. (see p. 21)

[71] C. Qin, A. S. Sandanayaka, C. Zhao, T. Matsushima, D. Zhang, T. Fujihara, and C. Adachi, "Stable room-temperature continuous-wave lasing in quasi-2D perovskite films," *Nature*, vol. 585, no. 7823, pp. 53–57, 2020. (see pp. 21 and 48)

[72] H. Zhu, Y. Fu, F. Meng, X. Wu, Z. Gong, Q. Ding, M. V. Gustafsson, M. T. Trinh, S. Jin, and X. Y. Zhu, "Lead halide perovskite nanowire lasers with low lasing thresholds and high quality factors," *Nature Materials*, vol. 14, no. 6, pp. 636–642, 2015. (see p. 21)

[73] S. A. Ivanov, J. Nanda, A. Piryatinski, M. Achermann, L. P. Balet, I. V. Bezel, P. O. Anikeeva, S. Tretiak, and V. I. Klimov, "Light amplification using inverted core/shell nanocrystals: Towards lasing in the single-exciton regime," *Journal of Physical Chemistry B*, vol. 108, no. 30, pp. 10625–10630, 2004. (see p. 22)

[74] J. Nanda, S. A. Ivanov, M. Achermann, I. Bezel, A. Piryatinski, and V. I. Klimov, "Light amplification in the single-exciton regime using exciton-exciton repulsion in type-II nanocrystal quantum dots," *Journal of Physical Chemistry C*, vol. 111, no. 42, pp. 15382–15390, 2007. (see p. 22)

[75] R. D. Schaller and V. I. Klimov, "High efficiency carrier multiplication in PbSe nanocrystals: Implications for solar energy conversion," *Physical Review Letters*, vol. 92, no. 18, pp. 1–4, 2004. (see p. 23)

[76] G. H. Carey, A. L. Abdelhady, Z. Ning, S. M. Thon, O. M. Bakr, and E. H. Sargent, "Colloidal Quantum Dot Solar Cells," *Chemical Reviews*, vol. 115, no. 23, pp. 12732–12763, 2015. (see p. 23)

[77] V. I. Klimov, A. A. Mikhailovsky, D. W. McBranch, C. A. Leatherdale, and M. G. Bawendi, "Quantization of multiparticle Auger rates in semiconductor quantum dots," *Science*, vol. 287, no. 5455, pp. 1011–1014, 2000. (see pp. 24, 32, 36, and 99)

[78] Y. Jia, R. A. Kerner, A. J. Grede, B. P. Rand, and N. C. Giebink, "Continuous-wave lasing in an organic-inorganic lead halide perovskite semiconductor," *Nature Photonics*, vol. 11, no. 12, pp. 784–788, 2017. (see p. 29)

[79] J. Roh, Y. S. Park, J. Lim, and V. I. Klimov, "Optically pumped colloidal-quantum-dot lasing in LED-like devices with an integrated optical cavity," *Nature Communications*, vol. 11, no. 1, pp. 1–10, 2020. (see pp. 29 and 70)

[80] Y. Wang, V. D. Ta, K. S. Leck, B. H. I. Tan, Z. Wang, T. He, C. D. Ohl, H. V. Demir, and H. Sun, "Robust Whispering-Gallery-Mode Microbubble Lasers from Colloidal Quantum Dots," *Nano Letters*, vol. 17, no. 4, pp. 2640–2646, 2017. (see p. 29)

[81] B. Le Feber, F. Prins, E. De Leo, F. T. Rabouw, and D. J. Norris, "Colloidal-Quantum-Dot Ring Lasers with Active Color Control," *Nano Letters*, vol. 18, no. 2, pp. 1028–1034, 2018. (see p. 29)

[82] M. M. Adachi, F. Fan, D. P. Sellan, S. Hoogland, O. Voznyy, A. J. Houtepen, K. D. Parrish, P. Kanjanaboos, J. A. Malen, and E. H. Sargent, "Microsecond-sustained lasing from colloidal quantum dot solids," *Nature Communications*, vol. 6, pp. 6–13, 2015. (see p. 29)

[83] J. M. Richter, M. Abdi-Jalebi, A. Sadhanala, M. Tabachnyk, J. P. Rivett, L. M. Pazos-Outón, K. C. Gödel, M. Price, F. Deschler, and R. H. Friend, "Enhancing photoluminescence yields in lead halide perovskites by photon recycling and light out-coupling," *Nature Communications*, vol. 7, 2016. (see pp. 32, 33, and 38)

[84] F. Staub, U. Rau, and T. Kirchartz, "Statistics of the Auger Recombination of Electrons and Holes via Defect Levels in the Band Gap - Application to Lead-Halide Perovskites," *ACS Omega*, vol. 3, no. 7, pp. 8009–8016, 2018. (see pp. 32 and 33)

[85] P. Landsberg, *Recombination in semiconductors*. Cambridge University Press, 1992. (see pp. 32 and 33)

[86] G. J. Supran, K. W. Song, G. W. Hwang, R. E. Correa, J. Scherer, E. A. Dauler, Y. Shirasaki, M. G. Bawendi, and V. Bulovic, "High-performance shortwave-

infrared light-emitting devices using core-shell (PbS-CdS) colloidal quantum dots," *Advanced Materials*, vol. 27, no. 8, pp. 1437–1442, 2015. (see p. 32)

[87] X. Yang, F. Ren, Y. Wang, T. Ding, H. Sun, D. Ma, and X. W. Sun, "Iodide capped PbS/CdS core-shell quantum dots for efficient long-wavelength near-infrared light-emitting diodes," *Scientific Reports*, vol. 7, no. 1, pp. 1–6, 2017. (see pp. 32 and 48)

[88] A. Stavrinadis, S. Pradhan, P. Papagiorgis, G. Itskos, and G. Konstantatos, "Suppressing Deep Traps in PbS Colloidal Quantum Dots via Facile Iodide Substitutional Doping for Solar Cells with Efficiency ¿10Energy Letters, vol. 2, no. 4, pp. 739–744, 2017. (see p. 32)

[89] S. Pradhan, A. Stavrinadis, S. Gupta, Y. Bi, F. Di Stasio, and G. Konstantatos, "Trap-State Suppression and Improved Charge Transport in PbS Quantum Dot Solar Cells with Synergistic Mixed-Ligand Treatments," *Small*, vol. 13, no. 21, pp. 1–9, 2017. (see p. 32)

[90] Y. Cao, A. Stavrinadis, T. Lasanta, D. So, and G. Konstantatos, "The role of surface passivation for efficient and photostable PbS quantum dot solar cells," *Nature Energy*, vol. 1, no. 4, pp. 1–6, 2016. (see p. 32)

[91] K. N. Bourdakos, D. M. Dissanayake, T. Lutz, S. R. Silva, and R. J. Curry, "Highly efficient near-infrared hybrid organic-inorganic nanocrystal electroluminescence device," *Applied Physics Letters*, vol. 92, no. 15, pp. 1–4, 2008. (see p. 32)

[92] X. Gong, Z. Yang, G. Walters, R. Comin, Z. Ning, E. Beauregard, V. Adinolfi, O. Voznyy, and E. H. Sargent, "Highly efficient quantum dot near-infrared light-emitting diodes," *Nature Photonics*, vol. 10, no. 4, pp. 253–257, 2016. (see pp. 32 and 85)

[93] S. Pradhan, A. Stavrinadis, S. Gupta, S. Christodoulou, and G. Konstantatos, "Breaking the Open-Circuit Voltage Deficit Floor in PbS Quantum Dot Solar Cells through Synergistic Ligand and Architecture Engineering," *ACS Energy Letters*, vol. 2, no. 6, pp. 1444–1449, 2017. (see p. 32)

[94] A. K. Rath, F. Pelayo Garcia De Arquer, A. Stavrinadis, T. Lasanta, M. Bernechea, S. L. Diedenhofen, and G. Konstantatos, "Remote trap passivation in colloidal quantum dot bulk nano-heterojunctions and its effect in solution-processed solar cells," *Advanced Materials*, vol. 26, no. 27, pp. 4741–4747, 2014. (see pp. 32, 33, and 88)

[95] S. Pradhan, F. Di Stasio, Y. Bi, S. Gupta, S. Christodoulou, A. Stavrinadis, and G. Konstantatos, "High-efficiency colloidal quantum dot infrared light-emitting diodes via engineering at the supra-nanocrystalline level," *Nature Nanotechnology*, vol. 14, no. 1, pp. 72–79, 2019. (see pp. 32, 33, 72, 85, and 104)

[96] A. Richter, S. W. Glunz, F. Werner, J. Schmidt, and A. Cuevas, "Improved quantitative description of Auger recombination in crystalline silicon," *Physical Review B - Condensed Matter and Materials Physics*, vol. 86, no. 16, pp. 1–14, 2012. (see p. 33)

[97] J. C. Blake, J. Nieto-Pescador, Z. Li, L. Gundlach, and L. Gundlach, "Femtosecond Luminescence Imaging for Single Nanoparticle Characterization," *Journal of Physical Chemistry A*, vol. 124, no. 23, pp. 4583–4593, 2020. (see p. 33)

[98] D. Bozyigit, S. Volk, O. Yarema, and V. Wood, "Quantification of deep traps in nanocrystal solids, their electronic properties, and their influence on device behavior," *Nano Letters*, vol. 13, no. 11, pp. 5284–5288, 2013. (see p. 34)

[99] D. Bozyigit, W. M. Lin, N. Yazdani, O. Yarema, and V. Wood, "A quantitative model for charge carrier transport, trapping and recombination in nanocrystal-based solar cells," *Nature Communications*, vol. 6, 2015. (see p. 34)

[100] A. R. Kirmani, G. Walters, T. Kim, E. H. Sargent, and A. Amassian, "Optimizing Solid-State Ligand Exchange for Colloidal Quantum Dot Optoelectronics: How Much Is Enough?," *ACS Applied Energy Materials*, vol. 3, no. 6, pp. 5385–5392, 2020. (see p. 39)

[101] D. V. Talapin, J. S. Lee, M. V. Kovalenko, and E. V. Shevchenko, "Prospects of colloidal nanocrystals for electronic and optoelectronic applications," *Chemical Reviews*, vol. 110, no. 1, pp. 389–458, 2010. (see p. 39)

[102] F. Deschler, M. Price, S. Pathak, L. E. Klintberg, D. D. Jarausch, R. Higler, S. Hüttner, T. Leijtens, S. D. Stranks, H. J. Snaith, M. Atatüre, R. T. Phillips, and R. H. Friend, "High photoluminescence efficiency and optically pumped lasing in solution-processed mixed halide perovskite semiconductors," *Journal of Physical Chemistry Letters*, vol. 5, no. 8, pp. 1421–1426, 2014. (see p. 48)

[103] A. Nurmikko, "What future for quantum dot-based light emitters?," *Nature Nanotechnology*, vol. 10, no. 12, pp. 1001–1004, 2015. (see p. 48)

[104] B. Guzelturk, Y. Kelestemur, M. Olutas, S. Delikanli, and H. V. Demir, "Amplified spontaneous emission and lasing in colloidal nanoplatelets," *ACS Nano*, vol. 8, no. 7, pp. 6599–6605, 2014. (see p. 48)

[105] F. Di Stasio, J. Q. Grim, V. Lesnyak, P. Rastogi, L. Manna, I. Moreels, and R. Krahne, "Single-Mode Lasing from Colloidal Water-Soluble CdSe/CdS Quantum Dot-in-Rods," *Small*, vol. 11, no. 11, pp. 1328–1334, 2015. (see p. 48)

[106] C. Gollner, J. Ziegler, L. Protesescu, D. N. Dirin, R. T. Lechner, G. Fritz-Popovski, M. Sytnyk, S. Yakunin, S. Rotter, A. A. Yousefi Amin, C. Vidal, C. Hrelescu, T. A. Klar, M. V. Kovalenko, and W. Heiss, "Random Lasing with Systematic Threshold Behavior in Films of CdSe/CdS Core/Thick-Shell Colloidal Quantum Dots," *ACS Nano*, vol. 9, no. 10, pp. 9792–9801, 2015. (see p. 48)

[107] G. Zaiats, D. Yanover, R. Vaxenburg, J. Tilchin, A. Sashchiuk, and E. Lifshitz, *PbSe-based colloidal core/shell heterostructures for optoelectronic applications*, vol. 7. 2014. (see pp. 49 and 56)

[108] S. Bisschop, P. Geiregat, T. Aubert, and Z. Hens, "The Impact of Core/Shell Sizes on the Optical Gain Characteristics of CdSe/CdS Quantum Dots," *ACS Nano*, vol. 12, no. 9, pp. 9011–9021, 2018. (see pp. 49, 63, and 65)

[109] L. K. Sagar, W. Walravens, Q. Zhao, A. Vantomme, P. Geiregat, and Z. Hens, "PbS/CdS core/shell quantum dots by additive, layer-by-layer shell growth," *Chemistry of Materials*, vol. 28, no. 19, pp. 6953–6959, 2016. (see p. 49)

[110] D. Yanover, R. Vaxenburg, J. Tilchin, A. Rubin-Brusilovski, G. Zaiats, R. K. Čapek, A. Sashchiuk, and E. Lifshitz, "Significance of small-sized PbSe/PbS core/shell colloidal quantum dots for optoelectronic applications," *Journal of Physical Chemistry C*, vol. 118, no. 30, pp. 17001–17009, 2014. (see p. 49)

[111] D. S. Koktysh, J. R. McBride, S. K. Dixit, L. C. Feldman, and S. J. Rosenthal, "PbS/PbSe structures with core-shell type morphology synthesized from PbS nanocrystals," *Nanotechnology*, vol. 18, no. 49, 2007. (see p. 49)

[112] D. D. Sarma, A. Nag, P. K. Santra, A. Kumar, S. Sapra, and P. Mahadevan, "Origin of the enhanced photoluminescence from semiconductor CdSeS nanocrystals," *Journal of Physical Chemistry Letters*, vol. 1, no. 14, pp. 2149–2153, 2010. (see p. 51)

[113] P. K. Santra, R. Viswanatha, S. M. Daniels, N. L. Pickett, J. M. Smith, P. O'Brien, and D. D. Sarma, "Investigation of the internal heterostructure of highly luminescent quantum dotquantum well nanocrystals," *Journal of the American Chemical Society*, vol. 131, no. 2, pp. 470–477, 2009. (see p. 51)

[114] J. Nanda, B. A. Kuruvilla, and D. D. Sarma, "Photoelectron spectroscopic study of cds nanocrystallites," *Physical Review B - Condensed Matter and Materials Physics*, vol. 59, no. 11, pp. 7473–7479, 1999. (see p. 51)

[115] H. Shinotsuka, S. Tanuma, C. J. Powell, and D. R. Penn, "Calculations of electron inelastic mean free paths. XII. Data for 42 inorganic compounds over the 50 eV to 200 keV range with the full Penn algorithm," *Surface and Interface Analysis*, vol. 51, no. 4, pp. 427–457, 2019. (see p. 53)

[116] Y. Nandan and M. S. Mehata, "Wavefunction Engineering of Type-I/Type-II Excitons of CdSe/CdS Core-Shell Quantum Dots," *Scientific Reports*, vol. 9, no. 1, pp. 1–11, 2019. (see p. 55)

[117] M. Şahin, S. Nizamoglu, O. Yerli, and H. Volkan Demir, "Reordering orbitals of semiconductor multi-shell quantum dot-quantum well heteronanocrystals," *Journal of Applied Physics*, vol. 111, no. 2, 2012. (see p. 55)

[118] W. K. Bae, L. A. Padilha, Y. S. Park, H. McDaniel, I. Robel, J. M. Pietryga, and V. I. Klimov, "Controlled alloying of the core-shell interface in CdSe/CdS quantum dots for suppression of auger recombination," *ACS Nano*, vol. 7, no. 4, pp. 3411–3419, 2013. (see pp. 57 and 85)

[119] D. I. Chepic, A. L. Efros, A. I. Ekimov, M. G. Ivanov, V. A. Kharchenko, I. A. Kudriavtsev, and T. V. Yazeva, "Auger ionization of semiconductor quantum drops in a glass matrix," *Journal of Luminescence*, vol. 47, no. 3, pp. 113–127, 1990. (see p. 57)

[120] I. Ramiro, B. Kundu, M. Dalmases, O. Özdemir, M. Pedrosa, G. Konstantatos, and G. Konstantatos, "Size- And Temperature-Dependent Intraband Optical Properties of Heavily n-Doped PbS Colloidal Quantum Dot Solid-State Films," *ACS Nano*, vol. 14, no. 6, pp. 7161–7169, 2020. (see p. 59)

[121] C. Dang and A. Nurmikko, "Beyond quantum dot LEDs: Optical gain and laser action in red, green, and blue colors," *MRS Bulletin*, vol. 38, no. 9, pp. 737–742, 2013. (see pp. 62 and 63)

[122] J. Ding, M. Hagerott, T. Ishihara, H. Jeon, and A. V. Nurmikko, "(Zn,Cd)Se/ZnSe quantum-well lasers: Excitonic gain in an inhomogeneously broadened quasi-two-dimensional system," *Physical Review B*, vol. 47, no. 16, pp. 10528–10542, 1993. (see p. 62)

[123] W. Lu, B. Zhong, and D. Ma, "Amplified spontaneous emission and gain from optically pumped films of dye-doped polymers," *Applied Optics*, vol. 43, no. 26, p. 5074, 2004. (see p. 63)

[124] B. Guzelturk, M. Pelton, M. Olutas, and H. V. Demir, "Giant Modal Gain Coefficients in Colloidal II-VI Nanoplatelets," *Nano Letters*, vol. 19, no. 1, pp. 277–282, 2019. (see p. 63)

[125] P. Geiregat, A. J. Houtepen, L. K. Sagar, I. Infante, F. Zapata, V. Grigel, G. Allan, C. Delerue, D. Van Thourhout, and Z. Hens, "Continuous-wave infrared optical gain and amplified spontaneous emission at ultralow threshold by colloidal HgTe quantum dots," *Nature Materials*, vol. 17, no. 1, pp. 35–41, 2018. (see p. 63)

[126] K. L. Shaklee and R. F. Leheny, "Direct determination of optical gain in semiconductor crystals," *Applied Physics Letters*, vol. 18, no. 11, pp. 475–477, 1971. (see p. 63)

[127] C. Liao, L. Tang, Y. Li, S. Sun, L. Wang, J. Xu, Y. Jia, and Z. Gu, "Toward temperature-insensitive near-infrared optical gain using low-toxicity Ag2Se quantum dots," *Nanoscale*, vol. 14, no. 28, pp. 10169–10175, 2022. (see p. 70)

[128] A. Yariv and P. Yeh, *Photonics: optical electronics in modern communications*. Oxford University Press: New York, NY, 2007. (see pp. 76 and 80)

[129] F. García-Santamaría, S. Brovelli, R. Viswanatha, J. a. Hollingsworth, H. Htoon, S. a. Crooker, and V. I. Klimov, "Breakdown of Volume Scaling in Auger Recombination in CdSe/CdS Heteronanocrystals: The Role of the CoreShell Interface," *Nano Let*, vol. 11, pp. 687–693, 2011. (see p. 85)

[130] X. Song and R. Leonhardt, "Ray-optics analysis of single mode condition for optical waveguides with rectangular cross-section," *Progress in Electromagnetics Research*, vol. 135, no. October 2012, pp. 81–89, 2013. (see p. 90)

[131] R. G. Hunsperger, *Integrated Optics Theory and Technology*. Springer, 6 ed., 2009. (see p. 90)

[132] I. D. Samuel and G. A. Turnbull, "Organic semiconductor lasers," *Chemical Reviews*, vol. 107, no. 4, pp. 1272–1295, 2007. (see p. 91)

[133] R. A. Maniyara, C. Graham, B. Paulillo, Y. Bi, Y. Chen, G. Herranz, D. E. Baker, P. Mazumder, G. Konstantatos, and V. Pruneri, "Highly transparent and conductive ITO substrates for near infrared applications," *APL Materials*, vol. 9, no. 2, 2021. (see p. 93)

[134] R. Berera, R. van Grondelle, and J. T. Kennis, "Ultrafast transient absorption spectroscopy: Principles and application to photosynthetic systems," *Photosynthesis Research*, vol. 101, no. 2-3, pp. 105–118, 2009. (see p. 96)

[135] K. L. Shaklee, R. E. Nahory, and R. F. Leheny, "Optical gain in semiconductors," *Journal of Luminescence*, vol. 7, no. C, pp. 284–309, 1973. (see p. 101)

List of Publications

List of Publications

This thesis is based on the following publications:

"Low-Threshold, Highly Stable Colloidal Quantum Dot Short-Wave Infrared Laser enabled by Suppression of Trap-Assisted Auger Recombination"
N. Taghipour, G. L. Whitworth, A. Othonos, M. Dalmases, S. Pradhan, Y. Wang, G. Kumar and G. Konstantatos
Advanced Materials, vol. 34, no. 3, pp. 2107532 (1-8), 2022

"Ultra-Thin Infrared Optical Gain Medium and Optically-Pumped Stimulated Emission in PbS Colloidal Quantum Dot LEDs"
N. Taghipour, I. Tanriover, M. Dalmases, G. L. Whitworth, C. Graham, A. Saha, O. Özdemir, B. Kundu, V. Pruner, K. Aydin, and G. Konstantatos
Advanced Functional Materials, vol. 32, no. 27, pp. 2107532 (1-7), 2022

"Colloidal Quantum Dot Infrared Lasers Featuring Sub-single-exciton Threshold and Very High Gain"
N. Taghipour, M. Dalmases, G. Whitworth, M. Dosil, A. Othonos, S. Christodoulou, S. M. Liga, and G. Konstantatos
Advanced Materials, Accepted article, pp. 2207678 (1-7), 2022

"Solution-processed PbS quantum dot infrared laser with room-temperature tunable emission in the optical telecommunications window"
G. L. Whitworth, M. Dalmases, N. Taghipour, and G. Konstantatos
Nature Photonics, vol. 15, no. 10, pp. 738-742, 2021

Other publications:

"Colloidal Quantum Dot Light Emitting Diodes at Telecom Wavelength with 18% Quantum Efficiency and Over 1 MHz Bandwidth"
S. Pradhan, M. Dalmases, N. Taghipour, B. Kundu, and G. Konstantatos
Advanced Science, vol. 9, no. 20, pp. 2200637, 2022.

"Ag-Refined Kesterite in Superstrate Solar Cell Configuration with 9.7% Power Conversion Efficiency"
Z. Wang, Y. Wang, N. Taghipour, L. Peng and and G. Konstantatos
Advanced Functional Materials, vol. 32, no. 43, pp. 2205948 (1-8), 2022